Library.

JNCASR
Acc No 3308
LIBRARY

JNCASR
620.189 2 P03
3308

# COLOSSAL MAGNETORESISTANCE, CHARGE ORDERING, PHASE SEPARATION AND RELATED PROPERTIES OF RARE EARTH MANGANATES

**A Thesis**

**Submitted for the Degree of**

**Doctor of Philosophy**

**By**

**L. Sudheendra**

**TO**
**JAWAHARLAL NEHRU CENTRE FOR ADVANCED SCIENTIFIC RESEARCH**
**(A Deemed University)**
**BANGALORE, INDIA**

**July 2003**

620.112 97
P03

# DECLARATION

I hereby declare that the matter embodied in this thesis entitled "**COLOSSAL MAGNETORESISTANCE, CHARGE ORDERING, PHASE SEPARATION AND RELATED PROPERTIES OF RARE EARTH MANGANATES**" is the result of investigations carried out by me at the Chemistry and Physics of Materials Unit, Jawaharlal Nehru Centre for Advanced Scientific Research, Bangalore, India, under the supervision of Professor C. N. R. Rao, *FRS* and Dr. A. R. Raju.

In keeping with the general practice of reporting scientific observations, due acknowledgement has been made whenever the work described has been based on the findings of the other investigators. Any omission that might have occurred by oversight or error of judgement is regretted.

L. Sudheendra

# STATEMENT

Certified that the work described in this thesis was carried out under our supervision at Jawaharlal Nehru Centre for Advanced Scientific Research, Jakkur, Bangalore, India.

**Prof. C.N.R. Rao**

**Dr. A.R. Raju**

# ACKNOWLEDGEMENTS

Words cannot express my sincere gratitude to Prof. C. N. R. Rao, *F.R.S.*, for it is only because of his immense support and encouragement that I have been able to pursue my education here. He has motivated and instilled in me the aptitude to do research. I am very grateful to him for suggesting the research problems, and for finding time to analyze and interpret my data. I also thank him for introducing me to various other research fields apart from manganates. I thank him for financial assistance. His endless enthusiasm and concern has been a constant source of strength for me throughout my stay here.

I am very grateful to Dr. A. R. Raju for his interest in this work. He has taught me how to get the best out of the instruments that I worked with. He has helped me to put all the experiments and data together.

My sincere thanks are due to my collaborators, Mr. Sachin Parashar, Prof. K.V. Ramanujachary, Dr. Chin, Dr. N. Chandrabhas, Mr. Motin Sheik, Dr. Govindaraj, Mr. Vivek Chand.

I thank all my teachers, Prof. Shobhana Narasimhan, Prof. G. U. Kulkarni, Prof. K. S. Narayan, Prof. S. Natarajan, Dr. N. Chandrabhas, Dr. Umesh Waghmare, Dr. Balasubramanian from JNC, Prof. T. N. Guru Row, Prof. K. J. Rao, Prof. A. K. Shukla and Prof. J. Gopalakrishnan from IISc.

My sincere thanks are due to the past and present members of the Nanomaterials and the Magnet and Crystal growth lab, for their help at one point or the other: Dr. Murugavel, Dr. Hemanth Aiyer, Dr. Ponnambalam, Dr. K. Vijaya Sarathy, Dr. Vanitha, Kripa Sindhu Sardar and Asish Kumar Kundu. Thanks also to Dr. Eswar Moorthy and Dr. Ayyappan for help and co-operation during my initial days of research at the centre.

I thank Prof. Hemalatha Balaram for her help, suggestions and comments in the bio-mineralization experiments.

I am very thankful to Mr. Srinath for his invaluable, technical assistance with the furnaces and other electronic instruments. I thank Mr. Renganathan, Mr. Anil, Mr. Basavaraj, Mr. Vasu, Ms. Usha, Mr. Srinivas, Mr. Hanume Gowda, Ms. Shashi and Mr. Xavier, Ms. Sudha and Ms. Veena for their continuous help.

I thank the Library staff: Ms. Jayamangala, Ms. Nandakumari, Mr. Rajeeva and Mr. Nagesh for their help. Many thanks to the JNC administrative staff.

I am very thankful to the computer lab staff: Mr. Rajesh, Ms. Sheetal and the CMC engineers.

Thanks to members of the various units in JNC, Ashish Kapoor, John, Sameen, Siva Kumar, Gargi, Neena, Reji, Ramshankar, Ranjith, Sujay, Manoj, Biru, Thiru, Uday, Girish, S. Lakshmi, Pushpa, R. Lakshmi, P. Dash, Ved, Sharmila, Shailesh, Selvi, Dhanashree, Manashi, Jaya, Meenakshi, Faraz, Arpita and Kavitha.

I sincerely thank Gautam, Deepak, Pattu, C.P. Vinod, N. Vinod, Sachin and Anupama, for being such wonderful friends.

Special thanks to my M.Sc batch mates and friends, Chandru, Sharada, Tushar, Sundar, Abhi for their unflinching support and friendship.

I am very thankful to JNCASR for the invaluable financial support and for excellent canteen and students residence.

I express my gratitude to my parents for without their support, I would not have ventured into research. Their endless patience, constant encouragement and love have been a constant source of strength for me.

# Contents

**Declaration** i

**Statement** ii

**Acknowledgements** iii

**Preface** v

Summary 1

1. A brief overview of rare earth manganates, $Ln_{1-x}A_xMnO_3$ (Ln = rare earth, A = alkaline earth) 7

**1.1 Structure** 8

**1.2 Crystal Field effects** 12

**1.3 Electronic structure** 14

**1.4 Electronic and magnetic properties of rare earth manganates** 16

1.4.1 Magnetic properties 16
1.4.2 Electrical transport properties in rare earth manganates 28
**1.5 Layered manganates** 33

**1.6 Phase transition and phase control** 34

1.6.1 Temperature induced phase transition 34
1.6.2 Magnetic field-induced phase transition 36
1.6.3 Bandwidth and bandfilling(pressure effects) 38
1.6.4 Cation size disorder 40
1.6.5 Electric field effects 42
1.6.6 Radiation-induced phase transition 43
**1.7 Phase separation** 45

1.7.1 Some examples 48
**1.8 References** 53

2. Scope of the present investigations 61

**2.1 Cation-deficient lanthanum manganates, $Ln_{1-x}MnO_3$ and $LaMn_{1-x}O_3$ ($x$ = 0-0.1)** 61

**2.2 Electric current induced effects on rare earth manganates** 62

**2.3 Grain size effects on the ferromagnetism, charge ordering and phase separation in $Nd_{0.5}Ca_{0.5}MnO_3$ and $Nd_{0.5}Sr_{0.5}MnO_3$** 64

**2.4 Electron-doped rare earth manganates, $Ln_xCa_{1-x}MnO_3$ (Ln = La, Nd, Gd and Y; x = 0.02-0.25)** 65

**2.5 Electron-doped rare earth manganates of Ruddelsden-Popper $CaO(Pr_{0.08}Ca_{0.92}MnO_3)_n$ ($n$ = 1,2,3 and $\infty$) series** 67

**2.6 Electronic phase separation in $(La_{1-x}Ln_x)_{0.7}Ca_{0.3}MnO_3$** 69

**2.7 References** 72

3. Experimental 76

**3.1 Synthesis** 76

3.1.1 Polycrystalline materials 76
*a. Solid state synthesis*
*Synthesis of $Ln_xCa_{1-x}MnO_3$ (Ln=La,Nd,Gd and Y)* 77
*Preparation of $(La_{1-x}Ln_x)_{0.7}Ca_{0.3}MnO_3$* 77
*b. Sol-gel synthesis* 77
*Sol-gel synthesis of $Nd_{0.5}A_{0.5}MnO_3$ (A=Ca and Sr)* 78
*Ruddlesden-Popper phases, $CaO(Pr_{0.08}Ca_{0.92}MnO_3)_n$ (n=1,2,3 and ∞)* 80

3.1.2 Crystal growth by floating zone melting technique 81
Cation-deficient lanthanum manganates, $Ln_{1-x}MnO_3$ and $LaMn_{1-x}O_3$ (x=0-0.1) 83
$Nd_{0.5}Ca_{0.5}MnO_3$ and $Pr_{0.6}Ca_{0.4}MnO_3$ crystals 84
$La_{0.77}Ca_{0.23}MnO_3$ 84

**3.2 Methods of characterization** 85

3.2.1 X-ray diffraction 85
3.2.2 Scanning electron microscopy 86
3.2.3 Magnetization 86
3.2.4 Electrical transport measurements 86
*a. DC conductivity* 86
*b. AC conductivity and dielectric spectroscopy* 87
c. *Magnetoresistance* 88
**3.3 References** 90

4. Results and Discussion 91

**4.1 Cation-deficient lanthanum manganates, $Ln_{1-x}MnO_3$ and $LaMn_{1-x}O_3$ (x = 0-0.1)** 91

4.1.1 Characterization 91
4.1.2 $LaMnO_3$ 94
4.1.3 $La_{0.96}MnO_3$ 94
4.1.4 $La_{0.9}MnO_3$ 95
4.1.5 $LaMn_{0.9}O_3$ 96
4.1.6 Conclusions 97

**4.2 Electric current-induced effects in charge-ordered $Nd_{0.5}Ca_{0.5}MnO_3$ and $Pr_{0.6}Ca_{0.4}MnO_3$** 98

4.2.1 Resistivity data 98
4.2.2 Charge ordering transition 99
4.2.3 Electroresistive ratio 101
4.2.4 Thermal hysteresis 101
4.2.5 I-V characteristics 103
4.2.6 Conclusions 105

**4.3 Electric current-induced first-order effects on the insulator-metal transition and the colossal electroresistance in rare earth manganates** 106

4.3.1 $La_{0.77}Ca_{0.23}MnO_3$ 106
*a. Resistivity data* 106
*b. Thermal hysteresis* 106

c. *Electroresistive ratio* 108
4.3.2 $La_{0.9}MnO_3$ 108
4.3.3 Conclusions 111

**4.4 Grain size effects on charge ordering, phase segregation and related properties of rare earth manganates, $Nd_{0.5}A_{0.5}MnO_3$ (A = Ca or Sr)** 112

4.4.1 $Nd_{0.5}Ca_{0.5}MnO_3$ 112
4.4.2 $Nd_{0.5}Sr_{0.5}MnO_3$ 117
4.4.3 Conclusions 121

**4.5 A systematic study of four series of electron-doped rare earth manganates, $Ln_xCa_{1-x}MnO_3$ (Ln = La, Nd, Gd and Y) over the x = 0.02-0.25 composition range** 122

4.5.1 Characterization 122
4.5.2 Magnetization data 125
4.5.3 Resistivity data 128
4.5.4 Magnetic hysteresis 130
4.5.5 Percolation 133
4.5.6 Conclusions 134

**4.6 Investigation of electrical and magnetic properties of electron-doped Ruddlesden-Popper phases, $CaO(Pr_{0.08}Ca_{0.92}MnO_3)_n$ (n=1, 2, 3 and ∞)** 135

4.6.1 Characterization 135
4.6.2 Resistivity and magnetization data 137
4.6.3 Conclusions 141

**4.7 Electronic phase separation in the rare earth manganates, $(La_{1-x}Ln_x)_{0.7}Ca_{0.3}MnO_3$ (Ln = Nd, Gd and Y)** 142

4.7.1 Characterization 142
4.7.2 Magnetization data 145
4.7.3 Resistivity 150
4.7.4 Size disorder effects 152
4.7.5 Percolation 154
4.7.6 Dielectric spectroscopy 155
4.7.7 Conclusions 158
**4.8 References** 160

5. Other work carried out by the candidate 164

**5.1 Bonding of monazite to $Al_2O_3$ and $TiO_2$ ceramics** 164

5.1.1 Introduction 164
5.1.2 Experimental 165
5.1.3 Results and discussion 165
a. *Microstructure of $Al_2O_3$ and $TiO_2$ composites with monazite* 165
b. *Grain size* 169
c. *Vickers hardness and fracture toughness* 169
5.1.4 Conclusions 170
5.1.5 References 172

**5.2 Peptide-induced formation of silica from tetraethylorthosilicate at near-neutral pH** 173

5.2.1 Introduction 173
5.2.2 Experimental 174

5.2.3 Results and discussion 176
a. *Effect of amino acids* 176
b. *Effect of concentration* 178
c. *Effect of pH* 179
d. *Effect of oligomers* 180
e. *Polypeptides* 182
5.2.4 Conclusions 183
5.2.5 References 184

**5.3 Silica fibres obtained with long-chain carboxylic acid templates** 185

5.3.1 Introduction 185
5.3.2 Experimental 186
5.3.3 Results and discussion 186
a. *X-ray analysis* 186
b. *SEM micrographs and IR analysis* 188
c. *TGA analysis* 188
d. *Effect of heating* 191
5.3.4 Conclusions 191
5.3.5 References 192

# PREFACE

This thesis, deals with the investigations of rare earth manganates consists of the following seven sections:

***Section 1:*** Cation-deficient lanthanum manganates, $Ln_{1-x}MnO_3$ and $LaMn_{1-x}O_3$.

***Section 2:*** Electric-current effects on rare earth charge-ordered $Pr_{0.6}Ca_{0.4}MnO_3$ and $Nd_{0.5}Ca_{0.5}MnO_3$ manganates.

***Section 3:*** Electric current induced first-order effects in colossal magnetoresistive $La_{0.77}Ca_{0.23}MnO_3$ manganates.

***Section 4:*** Grain size effects on the ferromagnetism, charge ordering and phase separation in $Nd_{0.5}Sr_{0.5}MnO_3$ and $Nd_{0.5}Ca_{0.5}MnO_3$.

***Section 5:*** Electron-doped rare earth manganates, $Ln_xCa_{1-x}MnO_3$ (Ln = La, Nd, Gd and Y; $x$ = 0.0 and 0.25).

***Section 6:*** Electron-doped Ruddelsden-Popper rare earth manganates with a composition $CaO(Pr_{0.08}Ca_{0.92}MnO_3)_n$ ($n$= 1,2,3 and $\infty$).

***Section 7:*** Electronic phase separation in $(La_{1-x}Ln_x)_{0.7}Ca_{0.3}MnO_3$ (Ln = Nd, Gd and Y).

Section 1 deals with the effect of cation deficiency at the A-site on the properties of $LaMnO_3$. There is a drastic change in the electron transport properties as the cation deficiency is varied. Some of the cation deficient manganates show substantial magnetoresistance.

In section 2, effects of electrical currents on single crystals of charge-ordered manganates $Pr_{0.6}Ca_{0.4}MnO_3$ and $Nd_{0.5}Ca_{0.5}MnO_3$ are discussed. A substantial change in

the electrical resistivity and an insulator to metal transition are observed. Such an insulator to metal transition is not observed even under large magnetic fields in these robustly charge-ordered manganates.

In section 3, results of the effect of electrical currents on single crystals of $La_{0.77}Ca_{0.23}MnO_3$ and $La_{0.9}MnO_3$, that exhibit colossal magnetoresistance are discussed. The insulator to metal transition temperature decreases with increasing current. The transition also shows thermal hysteresis indicating the phenomenon to be first order.

Grain size effects on $Nd_{0.5}Sr_{0.5}MnO_3$ and $Nd_{0.5}Ca_{0.5}MnO_3$ are discussed in section 4. The ferromagnetic and charge-ordered transition temperatures vary with the grain size. The phase separation is enhanced as the grain size of the material is decreased.

Section 5 discusses the results of $Ln_xCa_{1-x}MnO_3$ electron-doped manganates. The electronic transport properties vary with both concentration of dopant and the average radius of the A-site cation due to disorder effects. In section 6, electron doped Ruddlesden-Popper phases of $CaO(Pr_{0.08}Ca_{0.92}MnO_3)_n$ ($n$= 1,2,3 and $\infty$) are discussed.

Electronic phase separation in $(La_{1-x}Ln_x)_{0.7}Ca_{0.3}MnO_3$ is discussed in section 7. It is noteworthy that the electronic transport properties are controlled by the average size of the A-site cation and as the disorder due to the mismatch between the radius of the A-site cations.

***

# COLOSSAL MAGNETORESISTANCE, CHARGE ORDERING, PHASE SEPARATION AND RELATED PROPERTIES OF RARE EARTH MANGANATES

## SUMMARY*

Rare earth manganates of the formula, $Ln_{1-x}A_xMnO_3$ (Ln = rare earth A = alkaline earth), have been investigated widely in the last few years. They exhibit many fascinating properties such as colossal magnetoresistance (CMR), charge ordering and phase separation. These properties of the manganates are controlled by factors such as the bandfilling (concentration of $Mn^{4+}$ ions), bandwidth of the material as determined by the average size of the A-site cations $<r_A>$, site disorder and dimensionality. External factors such as temperature, external pressure, magnetic, radiation and electric fields also play an important role. A suitable choice of the external and internal parameters enables phase control in the manganates, which is essential for tuning the electron transport and related properties.

Cation deficiency at the A and B sites in $LaMnO_3$ is expected to have marked effects on the magnetic and electrical transport properties. In order to investigate this aspect, single crystals of La and Mn deficient compositions were prepared and investigated. It is found that $La_{0.9}MnO_3$ orders ferromagnetically at ~255 K and the ferromagnetic transition is accompanied by an insulator-metal (IM) transition. The magnetoresistance (MR) at the ferromagnetic transition (IM transition) temperature increases with the increasing magnetic field. A maximum MR of 55% was observed near the IM transition at 5 T. $La_{0.96}MnO_3$, shows a typical insulating behavior although the magnetization data shows a ferromagnetic-like

transition at 150 K. $LaMn_{0.9}O_3$ also shows a ferromagnetic insulator behavior similar to $La_{0.96}MnO_3$. The ferromagnetic insulators do not show MR throughout the temperature region studied.

Magnetic fields have been effectively used to probe charge-ordered manganates, where a 5-6 order change in the resistivity is caused by the application of magnetic fields. It was considered significant to compare the effect of the electrical and magnetic fields on charge-ordered manganates. Single crystals of manganates were chosen for studying the electric field effect in order to minimize grain boundary effects. Compositions such as $Nd_{0.5}Ca_{0.5}MnO_3$ which are robust charge-ordered manganates do not undergo melting of the charge-ordered state even under a high magnetic field of 20-30 T. On the other hand, the charge-ordered state in $Pr_{0.6}Ca_{0.4}MnO_3$, melts under the influence of a magnetic field of 6T, with the IM transition temperature increasing with increasing field. Electrical current effects on both these charge-ordered manganates shows comparable effects. With increasing current, there is a decrease in the resistivity of the manganates. There is an IM transition at low temperatures close to 60 K and the transition temperature is current-independent but shows hysteresis. The first-order nature of the phenomenon is attributed to current-induced phase separation. We also observe a drastic decrease in the charge-ordered transition temperature, $T_{co}$, with increasing current, which is attributed to the release of the lattice stress due to local electron delocalization driven by the current through the crystal. We have also calculated electroresistive ratio for both the charge-ordered manganates and find the ratio to increase with decreasing temperature and increasing current.

$La_{0.77}Ca_{0.23}MnO_3$ shows ferromagnetic ordering around 235 K, with an IM transition close to the ferromagnetic ordering temperature. It also exhibits CMR. The effect of electric current on a single crystal of this manganate is found to be drastically different compared to charge-ordered manganates. With increasing current, the resistivity decreases at room temperature, but on cooling, the $T_{IM}$ shifts to lower temperatures with increasing current. This phenomenon shows thermal hysteresis, with the IM transition temperature in the warming cycle being higher than that in the cooling cycle. The hysteresis increasing with increasing current. The electroresistive ratio (ER), defined similar to the magnetoresistive ratio, increases with increasing current, with a maximum value of 35 % at around 240 K. Below 220 K, a large positive ER is observed. The same phenomenon was also observed in $La_{0.9}MnO_3$ crystals.

$Nd_{0.5}Sr_{0.5}MnO_3$ shows a ferromagnetic transition at 250 K ($T_c$) followed by a charge-ordered antiferromagnetic transition at 150 K ($T_{co}$), as the sample is cooled from room temperature. The effect of grain size has been studied on these ordering transitions. The results obtained was compared with the robust charge-ordered material, $Nd_{0.5}Ca_{0.5}MnO_3$, which has the same $Mn^{3+}$ and $Mn^{4+}$ ratio, but does not exhibit ferromagnetic ordering. Samples of the two manganates with small grain sizes were first prepared by the sol-gel technique. Electron transport properties of the manganates were then studied as a function of sintering temperature which increased the grain size of the sample with increasing sintering temperature. For low sintering temperatures ($\leq$ 1173 K) and small grain sizes, ferromagnetism appears to dominate at low temperatures in $Nd_{0.5}Sr_{0.5}MnO_3$. Surprisingly, the fraction of the ferromagnetic phase below the $T_{co}$ decreases with increasing grain size or sintering

temperature. In $Nd_{0.5}Ca_{0.5}MnO_3$, the charge ordering and the antiferromagnetic transition appear to be quenched when sintering temperature was 1173 K or below, instead the manganate shows evidence of ferromagnetic interactions.

Electron-doped manganates of the form $Ln_{1-x}Ca_xMnO_3$ ($x > 0.5$) have attracted much attention in recent years because of the electron-hole asymmetry in the electron transport properties observed in the rare earth manganates. Compositions of $Ln_{1-x}Ca_xMnO_3$ close to $CaMnO_3$ appear to show a rather unusual behavior. As the rare earth concentration is increased, a ferromagnetic-like transition close to 100 K manifests itself, the ordering temperature appears being invariant to the concentration or the radius of the rare earth ion. The ferromagnetic behavior is observed up to a critical concentration of the rare earth, $x_c$, beyond which the electron doped manganates show antiferromagnetic charge ordering behavior. The antiferromagnetic charge ordering temperature increases with the concentration of the rare earth (or $Mn^{3+}$ ion). Similar results are found for all the rare earths studied. The critical concentration $x_c$, (below which there is ferromagnet-like behaviour) increases with the decrease in the radius of the rare earth. This is attributed to disorder arising from the mismatch between the radii of A-site cations as given by the variance, $\sigma^2$. The antiferromagnetic transition temperature (for a fixed $Mn^{4+}$ concentration) decreases with increasing $\sigma^2$. In the ferromagnetic like region, $\sigma^2$ induces phase separation which involves both ferromagnetic and antiferromagnetic domains, the size of the ferromagnetic domain increasing up to the critical concentration. The conduction in the phase separated regime appears to be percolative for temperatures less than 100 K.

Electron-doped compositions in the Ruddelsden-Popper (RP) series of manganates of the general formula, $CaO(Pr_{0.08}Ca_{0.92}MnO_3)_n$ ($n$ = 1,2,3 and ∞), have been investigated to see the effect of dimensionality on the electron transport properties of these manganates. The $Pr^{3+}$ ion has a radius similar to $Ca^{2+}$ minimizing the disorder effect due to lattice mismatch. The compositions with 8% $Pr^{3+}$ represents the critical concentration below which ferromagnetic like behavior is observed. A maximum in the magnetization and conductivity occurs for 8% Pr in the electron-doped manganate composition. As the number of perovskite layers increases, there is a drastic decrease in the resistivity. A decrease of three orders in magnitude is observed when n increases from one to infinity. Further, resistivities of the electron-doped RP phases are three orders of magnitude smaller in comparison with those of RP phases of the undoped calcium manganates. The magnetization on the other hand shows an anomalous behavior for $n$ = 1 sample. The Weiss constant varies from negative for $n$ = 1, to positive when $n$ is infinity. This cross-over of Weiss constant from a negative to a positive value could be taken as the signature of phase separation in this series of manganates.

The compositions $(La_{1-x}Ln_x)_{0.7}Ca_{0.3}MnO_3$ (Ln=Nd,Gd and Y) show a cross-over from a ferromagnetic metallic ground state when $x$ is zero, to a charge-ordered antiferromagnetic state when $x$ is unity. Hence, in principle, a mixed phase should be observed for some values of $x$ between zero and one. As the concentration of Ln is increased, there is a drastic change in the electron transport properties of these manganate compositions. For a critical concentration of Ln ($x$), the magnetization data shows that the compound seizes to be a ferromagnetic metal with no saturation magnetization or IM transition. This critical concentration $x$, $x_c$, decreases with

decrease in the radius of the rare earth ion. Hence, the critical concentration, $x_c$, for Nd, Gd and Y are 0.6,0.3 and 0.26 respectively. These critical concentrations also correspond to a unique value of average size of the A-site cation ($<r_A>$) of 1.18 Å ($<r_A^C>$). The compositions close to the critical values show evidence of phase separation. The compositions with $x$ greater than the critical value, $x_c$ ($<r_A> < <r_A^C>$) show canted antiferromagnetic insulating behavior. The dielectric constants of the samples with $x > x_c$ compositions show very high values in the range of $10^5$-$10^6$. The frequency dependence of the dielectric constant is similar to that of relaxor ferroelectrics and of the high dielectric constant copper titanate perovskites.

* Based on these studies, papers have been published in *Int. J. Inorg. Mater* (2000), *Solid. State. Commun.* (2001), *Solid. State. Commun.* (2003), *J. Phys. Condens. Matter* (2003), *J. Phys.Condens. Matter* (2003), *J. Appl. Phys* accepted (2003). One paper has been communicated to *J. Appl. Phys.*

# 1. A BRIEF OVERVIEW OF RARE EARTH MANGANATES, $Ln_{1-x}A_xMnO_3$ (Ln = RARE EARTH, A = ALKALINE EARTH)

Perovskite oxides with mixed valency have been studied for over 50 years. The chemical flexibility that the system offers is responsible for the wide range of structural, electronic and magnetic properties. The current interest in these materials, especially manganates, is due to the colossal magnetoresistance and related properties [1]. Understanding and exploiting the large magnetoresistance effects in single crystals, polycrystalline materials and thin films appears to be one of the motivations for continued research in this area. The rich electronic phase diagram of the rare earth manganates also reflects the competition amongst interactions which determine the electronic ground state. The interdependence of experiments, theory and technology evolution remains crucial for the future.

Broad features of the rare earth manganates and related perovskites were described by Jonker and vanSanten many years ago [2]. They discussed the preparation, crystal structure and magnetic properties of $La_{1-x}A_xMnO_3$ (A = Ca) and gave an account of the electrical resistivity [3]. The series was extended to A = Sr and Ba but the range of $x$ was limited to $x < 0.7$ and $x < 0.5$ respectively. Magnetoresistance and other transport properties were first discussed by Voger, who showed the magnetoresistance of $La_{0.8}Sr_{0.2}MnO_3$ to be negative with a peak near the ferromagnetic Curie temperature [4].

The current interest in the manganates started in 1993 following the preparation of high-quality thin films by von Helmoltt [5] and Charara [6], which exhibited very large magnetoresistance. Optimized compositions showed high

magnetoresistance near $T_c$. The term colossal magnetoresistance (CMR) is used to differentiate the manganates from the metallic systems showing giant magnetoresistance (GMR). This raised hopes of developing spin electronic devices based on hetrostructures.

## 1.1 Structure

The perovskite structure can be regarded as consisting of interpenetrating cubic close packed arrays of $O^{2-}$ anions and A cations, with the small B cations occupying the octahedral interstitial sites (Fig.1.1). A wide range of cations which can occupy the A-site in the perovskite structure. The ideal radii of the A and B-site cations, $r_A$ and $r_B$ respectively, occupying the sites in a cubic perovskite (C) can be deduced as follows. The value of $r_A$ is the same as $r_O$ which is 0.14 nm, while $r_B$ is $(2^{1/2}-1)r_O$ = 0.05nm. Goldschmidt [7] defined a tolerance factor

$$t' = \frac{r_A + r_O}{2^{1/2}(r_B + r_O)}$$

The value of $t'$ is unity for ideal cubic perovskite. The perovskite structure limit is $0.89 < t' < 1.02$. The value differs with the co-ordination number chosen.

All the manganates of the formula $Ln_{1-x}A_xMnO_3$ are derived from the cubic perovskite structure, but few of them have ideal cubic structure because the atoms are displaced from the ideal positions when $t' \neq 1$, which results from the various sizes of the substituted A and B-site cations. The flexibility shown by perovskite structure is remarkable as it accommodates misfits in ionic radii and electronically induced deformations by various kinds of distortions and tranformation to larger cells with lower symmetry. When $t'$ is close to unity, a rhombohedral distortion

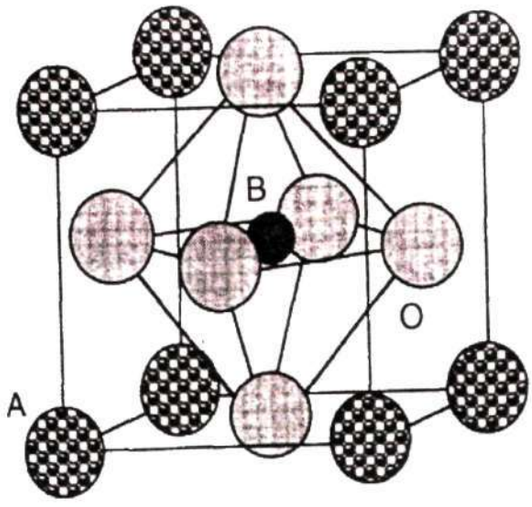


***Fig.1.1*** *Cubic structure of perovskite $ABO_3$ oxide*

involving co-operative rotation of $MnO_6$ octahedra in the structure about [111] axis is observed. When the value of $t'$ is large, there is a buckling of the network octahedra corresponding to co-operative rotation about [110] axis which leads to O-type orthorhombic $GdFeO_3$ structure as shown in Fig. 1.2. The $GdFeO_3$ structure has the unit cell dimensions of $a = 5.346$ Å, $b = 5.616$ Å and $c = 7.668$ Å and the B-O-B angle is reduced from 180° to 161°. It must be noted that in a typical O-type, $a < \frac{c}{\sqrt{2}} < b$. Rare-earth manganates of the type $Ln_{1-x}A_xMnO_3$ (Ln = rare earth and A = alkaline earth) adopt a different type of orthorhombic structure (O'-type) in which $\frac{c}{\sqrt{2}} < a < b$. The reason for the large distortion (deviation) from the ideal cubic perovskite is the Jahn-Teller effect of the $Mn^{3+}$ ions which causes the octahedra to extend in one direction in *a-b* plane [8]. These O and O' orthorhombic structure have four formula units per unit cell (z = 4) as compared to one in the case of ideal perovskite (z = 1).

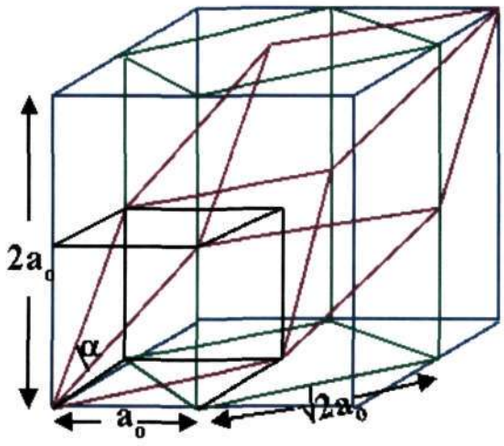


***Fig. 1.2*** *Relation between the different unit cells used to describe manganates.*

The manganates can crystallize not only in the orthorhombic and cubic structures, but also in the tetragonal, hexagonal and monoclinic structures as well. These unit cells are closely related and the rhombohedral or monoclinic angles are close to the ideal value $\alpha = 60°$ or $\alpha = 90°$ and $\beta = 90°$. Fig. 2 sketches the relation between the various unit cells. The doubled cubic cell with $a \approx a_o$ contains eight formula units (z = 8). The rhombohedral cell (R) with $a \approx 2a_o$ and $\alpha \approx 90.4°$ is a deformed version, slightly flattened along 111 direction. A smaller rhombohedral cell with $a \approx \sqrt{2}\, a_o$ and $\alpha \approx 61°$ is similarly deformed but has z = 2. As usual for rhombohedral structures, it is more convenient to index them in a hexagonal cell. The unit cell dimensions of orthorhombic cells are given by $a \approx \sqrt{2}\, a_o$, $b \approx \sqrt{2}\, a_o$, and $c = 2a_o$. Finally, the monoclinic cells are slightly deformed versions of the small cubic cell (z = 1) or the orthorhombic cells (z = 4).

In the case where $a \approx b$, the monoclinic cell is equivalent to a larger orthorhombic cell. The introduction of various cations at A-site, in addition to

causing a change in the crystal structure can change the electronic configuration of the B-site ion, which alters the inter atomic distances and bond angles.

When different ions of the same 3*d* element with different number of electrons occupy crystallograpically equivalent B-sites, say $B_1$ and $B_2$, the result is a partially filled *d* band with a tendency towards metallic conduction. The configurations $3d^n(B_1)$-$3d^{n+1}(B_2)$ and $3d^{n+1}(B_1)$-$3d^n(B_2)$ are degenerate if there is no charge ordering. Mixed valency of the transition metal ion leading to a metallic-like conduction was first shown by Verwey and de Boer in magnetite ($Fe_3O_4$) [9].

The mixed valence oxides $Ln_{1-x}A_xMnO_3$ can be regarded as solid solutions between the end members such as $LnMnO_3$ (eg: $LaMnO_3$) and $AMnO_3$ (eg: $CaMnO_3$) with the formal states $La^{3+}Mn^{3+}O_3^{2-}$ and $A^{2+}Mn^{4+}O_3^{2-}$, leading to mixed-valance compounds such as $(Ln_{1-x}^{3+}\ A_x^{2+})\ (Mn^{3+}M^{4+})O_3$. The electronic configurations of $Mn^{3+}$ and $Mn^{4+}$ are $3d^4$ and $3d^3$ respectively. Both the end member compounds are antiferromagnetic but the solid solutions show interesting electron transport properties.

The solubility of monovalent $A^+$ cations in rare earth manganates is very limited ($x < 0.2$) [10]. But, divalent $A^{2+}$ cations can be substituted for rare earth ions in these manganates, resulting in a complete range of solid solutions. A sequence of O' → O → R → C is found generally on increasing the $Mn^{4+}$ content by A-site substitution in these manganates.

Compositions of $(LaMn)_{1-x}O_3$ where $x$ is in the range 0-0.1, exhibit non stoichiometry at A as well as the B site. The nonstoichiometric compounds have either rhombohedral or orthorhombic structures. An orthorhomic structure is reported for $x \sim 0.02$, and a rhombohedral structure for $x \geq 0.04$. The O-R transition

decreases with increasing $x$ at low temperatures. The Mn-O-Mn bond angles vary from 155° to 164° depending upon the stoichiometry. As the stoichiometry governs the relative contents of $Mn^{3+}$ and $Mn^{4+}$, the magnetic as well as electrical properties are strongly stoichiometry dependent [11].

In the $Ln_xA_{1-x}MnO_3$, substitution at the A-site not only alters the Mn-O distances, but also the Mn-O-Mn bond angle, which is related to the A-site cation radius and tolerance factor $t'$. A variation from 156° to 168° is reported for $Ln_{0.7}A_{0.3}MnO_3$ with different cations [12,13] and from 155-164° for non stoichiometric $LaMnO_3$ [14]. Substitutions of different rare earths in A-site as in $(Ln_{1-x}Ln'_x)_{0.67}Ca_{0.33}MnO_3$, allows one to vary the Mn-O-Mn bond angle without any change in the Mn-O distances [13,16,17].

### 1.2 Crystal field effects

Crystal field effects greatly influence the magnetic and electrical properties of perovskite manganates. In the ideal lattice both A and B sites have the same cubic point symmetry *m3m*. However, due to distortions the point symmetry gets lowered. In $Ln_{1-x}A_xMnO_3$ the delocalization of manganese electrons can be neglected, in particular, for the end members with $x = 0$ and $x = 1$. The energy of $Mn^{3+}$ and $Mn^{4+}$ ions can be represented by a crystal-field energy level arising from the spectroscopic term, which for $Mn^{3+}$ in the octahedral co-ordination is $^5E_g$ (ground state), originating from *5D*. In purely cubic symmetry, the ground state is a

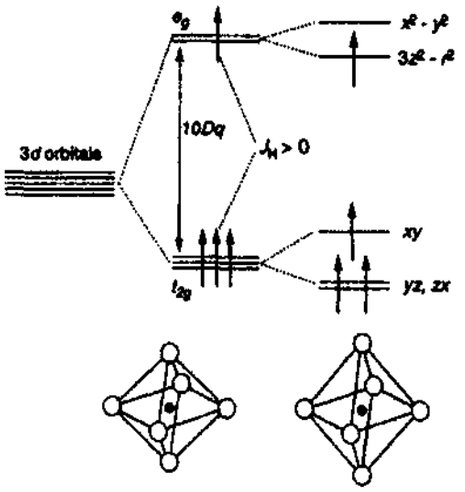


*Fig. 1.3 Crystal field splitting in manganates containing $Mn^{3+}$ ions and their corresponding octahedral distortions.*

magnetic singlet. For $Mn^{4+}$ it is $^4A_2$, of $4F$. The excitation of an electron from $t_{2g}$ to $e_g$ orbital leads to the $^5T_{2g}$ excited state of $Mn^{3+}$ in $LnMnO_3$ (Fig.1.3). The energy of transition was estimated from optical spectra and was found to be 2.1 eV for light rare earths and 2.3 eV for heavier rare earths. For $LaMnO_3$, two absorption bands have been detected at 1.8 eV and 2.3 eV. The spitting has been attributed to Jahn-Teller effect. The $d^4$ ($^5E_g$) ion in octahedral co-ordination $t_{2g}^3 e_g^1$ is a strong Jahn-Teller ion because it lowers its energy in proportion to the splitting of the $e_g$ levels by uniaxial distortion [17]. The $\Delta_{cf}$ =10Dq value can be estimated by comparing the spectra of $Mn^{3+}$ in various distorted environments. The value has been estimated to be 1.5 eV and $2\delta_{JT} \approx 1$ eV. Optical phonon measurements yield a value of 0.6 eV for $\delta_{JT}$ [18].

## 1.3 Electronic structure

Perovskite oxides with closed shell B-site ions are transparent insulators. (eg., $CaTiO_3$, $SrTiO_3$, $LaAlO_3$, $LaScO_3$ and $LaGaO_3$). In $LaAlO_3$, there is a gap of 5.6 eV between the top of the valence band (derived from the $2p$ of the oxygen orbitals) and the bottom of the empty conduction band (derived from the unoccupied $5d$-$6s$ orbitals of $La^{3+}$ or $3s$ orbitals of $Al^{3+}$). Empty $d^0$ levels usually lie near the top of this $2p$-n$s$ gap, where as the $3d^{10}$ levels lie below the top of $2p$ band. The $d$ levels fall at progressively lower symmetry on passing along the $3d$ series because of the increasing nuclear charge.

Transition-metal oxides are materials whose electronic properties are determined by the interplay of several interactions of comparable magnitude, all of the order of 1 eV.

a) Mott-Hubbard interactions $U_{dd}$ which is the cost of creating a $d^{n+1}$ and $d^{n-1}$ charge excitation in a array of $d^n$ ions.

b) Charge transfer interactions $U_{pd}$, which is the cost of transferring an oxygen p electron to the neighbouring d ion to create a $p^5d^{n+1}$ charge excitation from $p^6d^n$.

c) The transfer integral, t, which determines the $d$-electron bandwidth, W

d) Hund's rule on-site exchange interaction, $U_{ex}$, which is the energy required to flip a d-electron spin.

e) The crystal field interactions $\Delta_{cf}$ and $\delta_{JT}$.

Transition-metal oxides may be Mott-Hubbard or charge transfer insulators. When the electron correlations are such that $U_{dd} > W$ or $U_{pd} > W$ respectively [19]. Most oxides of the early $3d$ transition metals are Mott-Hubbard insulators. In addition, for the end members of the $3d$ series, the charge transfer gap may become

zero leading to metallicity. In the middle of the series where the $U_{dd} \approx U_{pd}$ the nature of the gap is not clear.

Interelectronic correlations which give rise to Hund's rules for the free ion are perturbed by the crystalline electrostatic field due to the oxygen ion as in the case for manganates, where the B-site (Mn) is co-ordinated by six oxygen neighbours resulting in an octahedra. The five *d* orbitals each of which can accommodate one electron of each spin is therefore split due to the octahedral crystal field into $t_{2g}$ ($d_{xy}$, $d_{yz}$ and $d_{xz}$), and the $e_g$ orbitals ($d_{x^2-y^2}$ and $d_{z^2}$), which have their lobes oriented between the oxygen neighbours. The latter other hand are directed towards the oxygen neighbour. The $t_{2g}$ have a lower energy because of the electrostatic repulsion of electrons on neighbouring sites, and the resulting crystal field splitting $\Delta_{cf}$ between the $t_{2g}$ and $e_g$ orbitals is of the order of 1.5 eV. Intraatomic correlations which give rise to the Hund's first rule (maximum S) is represented on a one-electron energy diagram by introducing an energy splitting $U_{ex}$ of up spin and down spin orbitals, which is greater than $\Delta_{cf}$. A good example for evidence that $U_{ex}$ and $\Delta_{cf}$ are similar in magnitude is provided by $LaCoO_3$ which does not follow the Hund's first rule (Nickel substituted Mn also show similar trends). The manganese ion on the other hand is a high spin element; the divalent ion $Mn^{2+}$ has a stable $3d^5$ configuration, a half filled shell $t_{2g}^3 e_g^2$ with S=5/2 and a spherically symmetric electron density. Trivalent manganese is $3d^4$, $t_{2g}^3 e_g^1$ with S=2, whereas $Mn^{4+}$ is $3d^3$, $t_{2g}^3 e_g^0$ with S=3/2. The spin only moments of these ions are 5 $\mu_\beta$, 4 $\mu_\beta$ and 3 $\mu_\beta$ respectively.

A distortion of octahedra lowers the symmetry of cubic crystal field in such a way that the center of gravity of the $t_{2g}$ levels and the center of gravity of $e_g$ levels are unchanged. Therefore, nothing is to be gained by $Mn^{2+}$ or $Mn^{4+}$ from such distortion, but, $Mn^{3+}$ can lower its energy in proportion to the distortion, and the corresponding penalty is elastic energy will scale as the distortion squared. Hence, there is a marked tendency of the $d^4$ ions to distort their octahedral environment in order to lower their energy. This is popularly known as Jahn-Teller effect. The tetragonal elongation of the octahedron found in O'-type structure will stabilize the $d_{z^2}$ orbital relative to the $d_{x^2-y^2}$ orbital.

The $t_{2g}$ orbitals overlap relatively less with the orbitals of nearby oxygen or rare earth, so these electrons tend to form a localized $t_{2g}^3$ ion core. However, the $e_g$ orbitals overlap directly with the p orbitals of the oxygen neighbours, so they tend to form a σ* antibonding band. The end member compound $LaMnO_3$ has a distorted perovskite structure where the Fermi level falls in a gap between the Jahn-Teller split $e_g$ bands. However, intermediate compositions such as $La_{1-x}Ca_xMnO_3$ with a pseudo cubic structure has a partially filled σ* bands. The electrons in these partially filled band are responsible for conduction through ferromagnetic spin mediation. A direct overlap of $t_{2g}$ core electrons of the adjacent manganese ions leads to antiparallel exchange coupling, since only the spin down orbitals would be empty.

## 1.4 Electronic and magnetic properties of rare earth manganates

### 1.4.1 Magnetic properties

***a) Spin ordering: Ferromagnetism and Antiferromagnetism:*** Electron transport properties of the rare earth manganates are governed by the structure and the

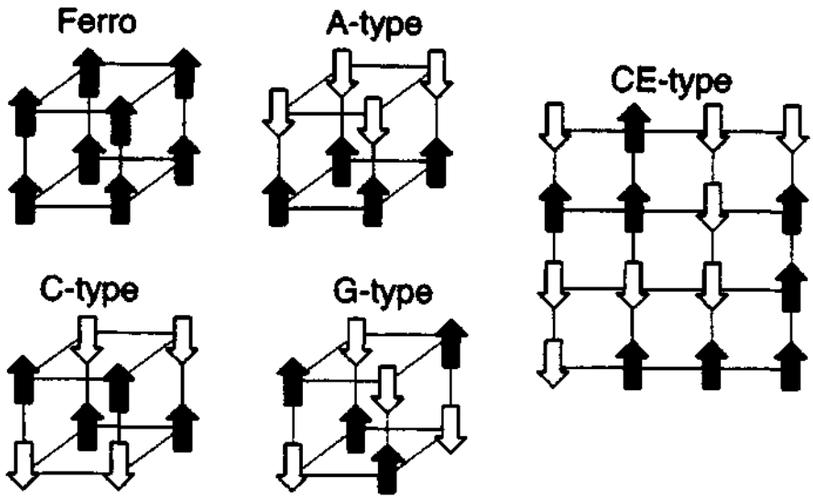


*Fig.1.4 Schematic showing the various possible orientation of spins at the B-site of a perovskite manganate.*

amount of charge carriers present. Two characteristic distortions of the perovskite structure influence the magnetic order of the manganates. (a) small size of the A-site cation ($t' < 1$) leading to co-operative tilting of the $MnO_6$ octahedra and (b) the Jahn-Teller distortion of the octahedra which contains a $Mn^{3+}$ ion at their center and their co-operative ordering. The critical temperatures at which these two distortions set in are different. The former produces a buckling of the octahedra about 1250 K, which may be present over the entire range of concentrations.

The distribution of $Mn^{3+}$ and $Mn^{4+}$ ions in the lattice too plays an important role as co-operative Jahn-Teller ordering of the $Mn^{3+}$ ion at low temperatures. The mixed-valance manganates having ($Mn^{3+}$ and $Mn^{4+}$) can exhibit magnetic order, charge order and orbital order. Some of the simplest magnetic modes for B-site in perovskite structure are illustrated in fig 1.4. Mode F is ferromagnetic but all others (A, C and G) are antiferromagnetic. Mode A has four parallel and two antiparallel spins on its nearest neighbours. In mode G, each B-site cation is oriented anti

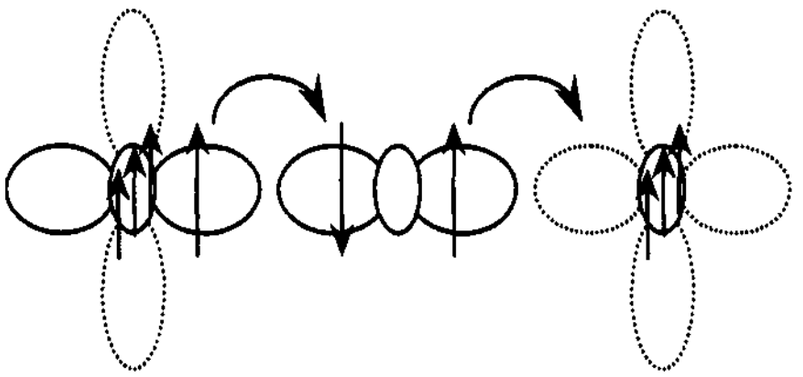

***Fig. 1.5*** *Schematic showing the double exchange mechanism between $Mn^{3+}$ and $Mn^{4+}$ ions.*

parallel to its six neighbours. Modes C and E each have four antiparallel and two parallel neighbours. A composite CE mode is composed of checkered board of alternating C and E blocks.

***b) Double exchange model:*** The crystallographic, magnetic structures and the associated rich phase diagram of the $La_{1-x}Ca_xMnO_3$, as well as the dependence of the magnetic properties on $x$ were established as early as 1955 by Wollan and Koehler [20]. There are three main regions for small concentration of $Mn^{4+}$, the compounds are essentially antiferromagnetic. For $x \sim 0.3$ the manganates exhibit ferromagnetism and they revert to antiferromagnetic ground state in compositions with $x > 0.5$. Jonker [21] first analyzed these results and concluded that the exchange is weakly positive (ferromagnetic) between two $Mn^{3+}$ ions, negative between two $Mn^{4+}$ ions and is positive between $Mn^{3+}$ and $Mn^{4+}$ ions. Indicating that compositions close to the end members should show ferromagnetic correlations.

Ferromagnetism in these compositions is strongly correlated to resistivity and the compositions showing ferromagnetism were metallic whereas the

compositions were insulators for antiferromagnetic ordering. A concept of indirect magnetic exchange between 3*d* atoms was introduced by Zener [22] to explain the correlation between ferromagnetism and metallicity. It was assumed that strong intra-atomic Hunds rule exchange would restrict the carriers to change their spin orientation when hopping from one ion to the other. Therefore hopping of carries was favored when the two ions had parallel spin orientations. A system with parallel spins with conduction electrons favored ferromagnetism, which could explain strong correlation between conductivity and ferromagnetism. A magnetic exchange interaction between $Mn^{3+}$ and $Mn^{4+}$ mediated by oxygen ion results in a transfer of one electron from $Mn^{3+}$ to oxygen and from oxygen to $Mn^{4+}$.

Such a transfer of electrons involving charge transfer through mediation of spin on the oxygen ion was termed Double Exchange (Fig.1.5). It must be noted here that the double exchange would be favored when $Mn^{3+}$-O-$Mn^{4+}$ bond is linear. When the $Mn^{3+}$-O-$Mn^{4+}$ angle is less than 180°, the orbitals on $Mn^{3+}$ and $Mn^{4+}$ interact directly leading to antiferromagnetism. This direct interaction of *d* orbitals on the adjacent ions is termed as Superexchange. As the magnetic exchange is antiferromagnetic, electron transfer becomes difficult leading to insulating behavior.

***c) General exchange model:*** A more generalized picture of the double exchange mechanism was provided by Anderson and Hasegawa [23] involving two magnetic ions with random spin directions. They calculated $t = t_o \cos(\frac{\theta}{2})$ where $t_o$ is the normal transfer integral that depends on the spatial wavefunctions, the term

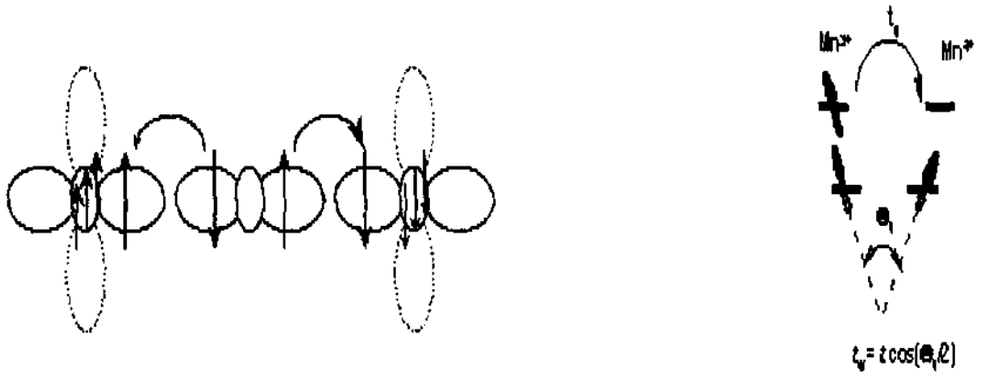


*Fig. 1.6 a) Schematic showing a super exchange mechanism between $Mn^{3+}$ and $Mn^{4+}$ ion. b) schematic showing the transfer integral dependence on the orientation of the spins*

$\cos(\frac{\theta}{2})$ is due to the spin wavefuntion and θ is the angle between the two spin directions. This is quite unlike superexchange where the coupling is proportion to cosθ (Fig.1.6).

***d) Charge and orbital ordering:*** Charge ordering is also known as Wigner crystallization, and is driven by interatomic coulomb interactions. The mobile *d* electron can be localized on certain manganese ions to form a regular lattice for particular occupancies of the *d* band, provided inter electronic coulomb interaction is comparable with the conduction-electron bandwidth, W [24].

Charge-ordering results in a small displacement of the oxygen atoms to accommodate the ordered cation lattice. Charge ordering is most likely when the

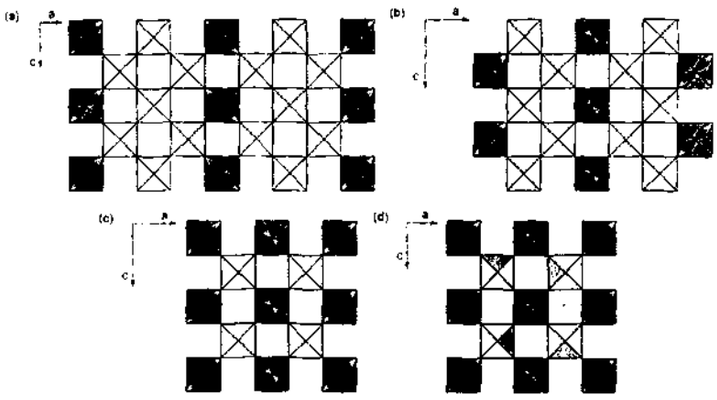

***Fig.1.7*** *schematic representation of different types of charge ordering obtained with various dopent concentrations.*

temperature is low and x is rational fraction, especially 1/4, 1/3 or 1/2 (Fig. 1.7). The charge ordering therefore localizes the fourth d electron in $Mn^{3+}$.

Kanamori [17] pointed out that the carriers in mixed valent manganates may be strongly coupled to local distortions, and orbital ordering can occur at certain carrier concentrations when *d* electrons occupy an asymmetric orbital as shown in fig 1.7. The driving force for such orbital ordering is partly electrostatic repulsion of charge clouds, and is stabilized by Jahn-Teller distortions on adjacent octahedra. Charge ordering and orbital ordering is maximized at $x = 1/2$ compositions as shown in Fig.1.7d.

***e) Magnetic properties of $La_{1-x}Ca_xMnO_3$:*** For low $Mn^{4+}$ concentrations ($x > 0$) in $La_{1-x}Ca_xMnO_3$, neutron diffraction patterns have shown that for increasing $x$, the ferromagnetic component increases up to $x = 0.3$; where the sample becomes ferromagnetic [20,25]. At $Mn^{4+}$ concentrations above 0.35, a mixture of ferromagnetism and antiferromagnetism was found. The new antiferromagnetism

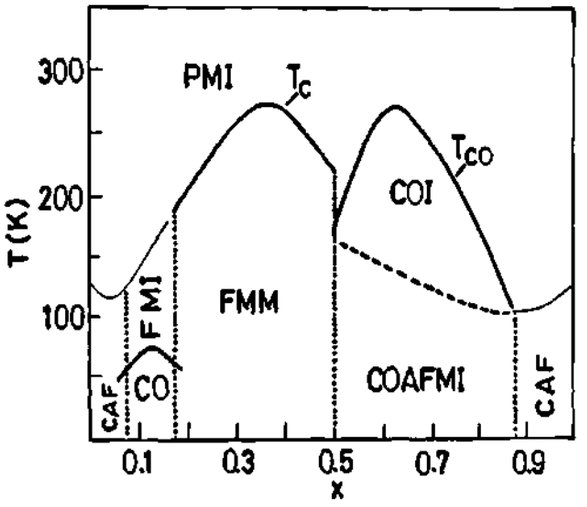


*Fig. 1.8 The magnetic phase diagram of $La_{1-x}Ca_xMnO_3$ (ref. 42).*

phase consisting of a regular CE type stacking. This results in charge ordering near a $Mn^{4+}$ and $Mn^{3+}$ ratio of unity ($x = 0.5$, Fig. 1.8).

On heating, the $x = 0.5$ compound antiferromagnetic order turns into ferromagnetic order around 170 K before becoming paramagnetic at $T_c = 225$ K. As $x$ increases, structure progressively transforms itself into the C-type structure corresponding to another charge-ordering state for $Mn^{4+}$ to $Mn^{3+}$ ratio of 3 ($x = 0.75$). The magnetic configuration consists of ferromagnetic chains ordered antiferromagnetically. Here again the ferromagnetic bond is shorter than antiferromagnetic bond. As the concentration of $Mn^{4+}$ increases further, they replace $Mn^{3+}$ ions at random creating more antiferromagnetic bonds in the structure. The end members of this series, $CaMnO_3$ is fully antiferromagnetic with nearest neighbour G-type antiferromagnetic structure.

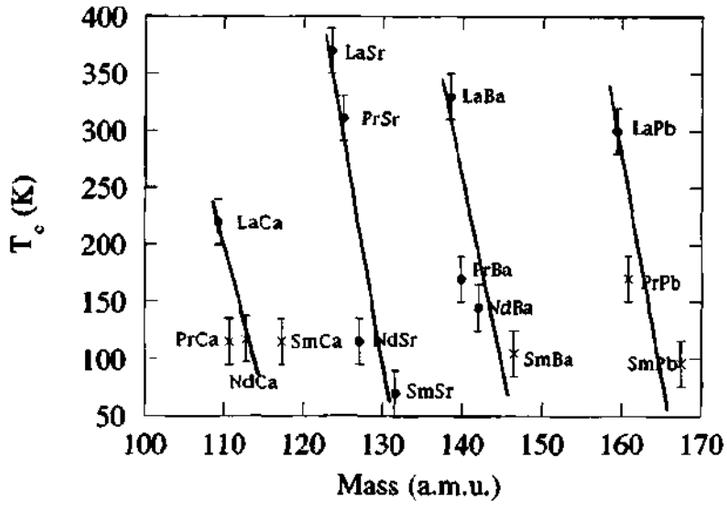


*Fig. 1.9 $T_c$ versus the mass of the A-site cations • = compounds showing $T_c$, X = compounds exhibiting an increase in resistivity at low temperatures (ref. 30).*

All the magnetic structures present in $La_{1-x}Ca_xMnO_3$ series of compositions are exhibited by other systems of the more general formula $Ln_{1-x}A_xMnO_3$ with the critical range of concentrations for ferromagnetism, antiferromagnetism, charge and orbital ordering being different.

***f) Ferromagnetic manganates:*** Ferromagnetism arising from the exchange interactions depends upon interatomic distances and bond angles. Havinga [26] first showed how the strength of the exchange interaction between two $Mn^{3+}$ ions in the octahedral environment varied with the Mn-O-Mn bond angle θ. For a stiff Mn-O bond lengths, the bond angles were found to decrease in the order Cubic > rhombhohedral > orthorhombic and the net magnetic interaction became negative for θ < 150° [26,27]. Both in binary and ternary solid solutions of the type $(LnLn')_{1-x}(AA')_xMnO_3$, the $T_c$ decreased with decrease in Mn-O-Mn bond angle [11,16,28,29]. The saturation magnetization is difficult with decreasing Mn-O-Mn

angle, which was explained based on the competing interactions between double exchange and superexchange leading to a canted Mn moments. As can be seen from the Fig. 1.9, with a given alkali cation there is a tendency of $T_c$ to increase with increasing atomic radius of the rare earth [30] which is related to the $e_g$ band width [15]. However, there is no clear trend of $T_c$ with average atomic weight, size or electronegativities of the alkaline ion.

The cation-deficient lanthanum manganates $(LaMn)_{1-x}O_3$ are antiferromagnetic and insulating for $x < 0.03$, but show ferromagnetism with spin-only moment of 3.8 $\mu_\beta$ for compositions exceeding 0.03. A cation deficient sample with $x > 0.04$ remains insulating down to the lowest temperature exhibiting a canted spin structure. When $x \geq 0.05$ compound exhibits a metal-insulator transition at the ferromagnetic ordering temperature, $T_c$. $x$-T phase diagram has been proposed by Töpfer and Goodenough [31]. Although these non stoichiometric oxides exhibit ferromagnetic ordering when the cation deficiency is present in only one sublattice, Ramanujachary et al have shown the presence of ferromagnetic ordering in $(LaMn)_{1-x}O_3$ crystals having both A and B-site deficiency grown from fused salt electrolysis [32].

The Curie temperature is reduced by the substitution of non-magnetic trivalent ions at the B-site (eg. Al, Ga, Fe etc.) [33,34]. On the other hand, substitution of $Cr^{3+}$ and $Ru^{4+}$ in place of $Mn^{3+}/Mn^{4+}$ induces ferromagnetism by destroying charge ordering [35,36]. This behavior has been linked to the magnetic degrees of freedom associated with non-collinear ferromagnetic ordering. The $T_c$ of such compositions occurs around 100 K, and the magnetization and the resistivity transitions are found to be hysteric [11,30,34,37]. These compositions also show

characteristic spin-glass behavior and can be modeled in terms of magnetically inhomogeneous spin clusters [38]. Similarly there is a tendency for $T_c$ to increase with increasing tolerance factor or average size of the A-site cation [39].

The temperature dependent sublattice magnetization of $LaMnO_3$ crystals have been followed by neutron diffraction and the critical exponent, β in the expression $m \propto [1-(\frac{T}{T_c})]^{\beta}$ was evaluated to be in the range of 0.25-0.28 [40, 41]. Compounds which are ferromagnetic, but with a spontaneous magnetization considerably less than the spin only moment, exhibit characteristic differences in field-cooled and zero-field-cooled magnetic measurements. The coercivity for these compounds increases rapidly at low temperature [38].

***g) Charge, Spin and Orbital ordering in $Ln_{1-x}A_xMnO_3$:*** The CE-type AFM charge-ordered state in $Ln_{1-x}A_xMnO_3$ is associated with the ordering of $3d_{x^2-r^2}$ or $3d_{y^2-r^2}$ type orbitals at the $Mn^{3+}$ site. Fig. 1.10 (d) shows the spin, charge and orbital ordering in the CE-type AFM state. The CE type charge ordering seen in some of the manganates exhibit AFM ordering at the charge ordering temperature. Generally, the charge ordering temperature is higher than Nèels temperature ($T_{co} \geq T_N$). This implies, spin ordering occurs concurrently or after charge ordering. Complete orbital ordering is achieved when there is both charge and spin ordering. Orbital and spin ordering occur without charge ordering in some of the manganates showing A-type antiferromagnetism is shown in Fig. 1.10 (c) [eg., $Nd_{0.45}Sr_{0.55}MnO_3$]. A-type AFM in $Ln_{1-x}A_xMnO_3$ is generally not charge-ordered as

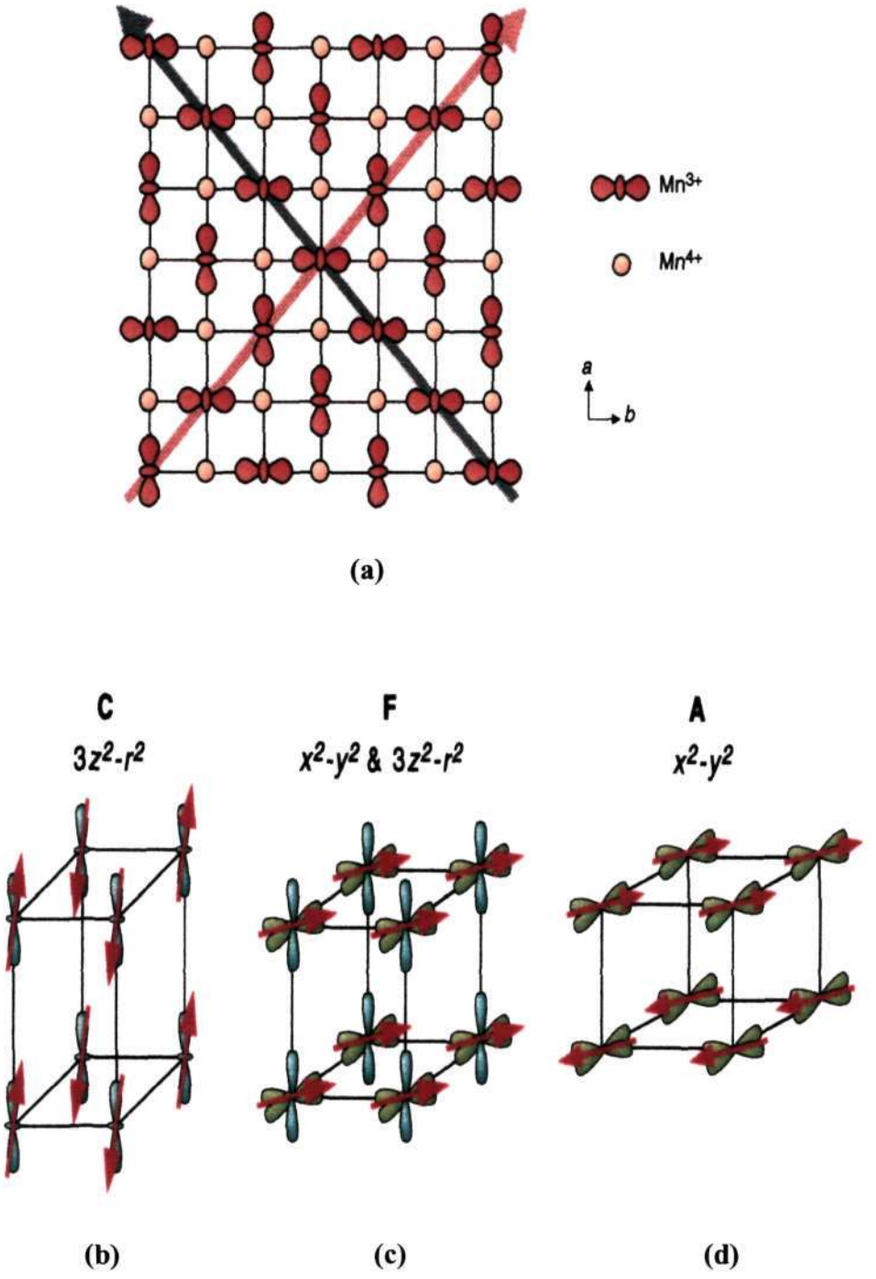


***Fig. 1.10*** *Schematic showing the orbitals and the spin orientations of Mn ions in a perovskite lattices a) C-type anitferromagnetism involving $d_{z2}$ orbitals; b) F-type ferromagnetism; c) A-type anitferromagnetic involving $d_{x2-y2}$ orbitals; d) CE-type with a checkered board arrangement of $d_{z2}$ orbitals (ref.42).*

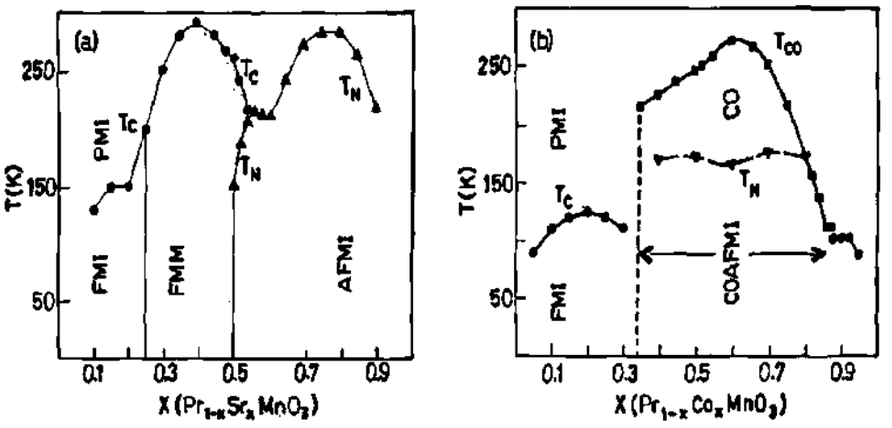


a b

***Fig. 1.11*** *a) Phase diagram of $Pr_{1-x}Sr_xMnO_3$ b) Phase diagram of $Pr_{1-x}Ca_xMnO_3$ (ref. 42).*

electron transfer can occur between the Mn cations in the *a-b* plane. Orbital ordering in A-type AFM is depicted in Fig. 1.10 (d). Here the $x^2$-$y^2$ type orbital is present at the $Mn^{3+}$ site. The orbital order melts into a quantum-disordered state, and the compound shows the ferromagnetic-metallic (F) state for $0.2 < x \leq 0.5$ for $La_{1-x}Ca_xMnO_3$ manganate (Fig.1.10 (b)).

The phase diagram of $La_{1-x}Ca_xMnO_3$ (Fig.1.8) shows charge ordering in the composition range $x \approx 0.5$-$0.8$ range whereas for $Pr_{1-x}Sr_x$ $MnO_3$ no charge ordering has been observed (Fig. 1.11a). On the other hand, $Pr_{1-x}Ca_xMnO_3$ (Fig. 1.11b) exhibits charge ordering over the $x = 0.3$-$0.8$ range. Such variations in properties are due to the effect of average radius of the A-site cations. The smaller radius favoring charge ordering. From Fig.11b it can be noted that charge-ordering temperature, $T_{co}$ increases with $x$. The paramagnetic state is characterized by FM spin fluctuations. At $T_{co}$ these fluctuations decrease and disappear at $T_N$ [42].

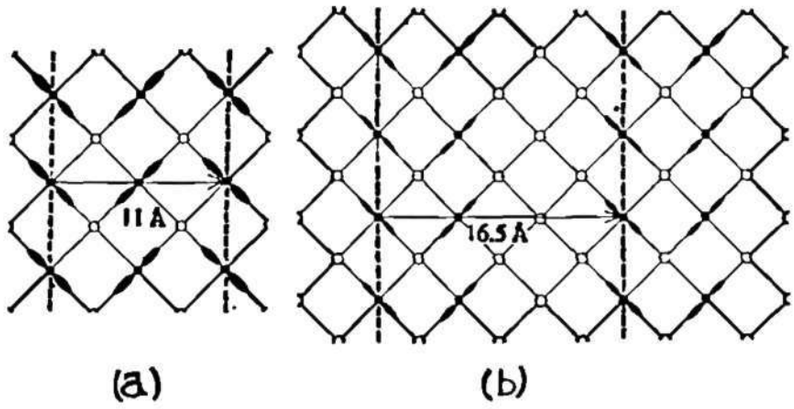


*Fig. 1.12 Charge and orbital ordering in $La_{1-x}Ca_xMnO_3$ showing charge modulations a) x=0.5 b) x=0.67. Open circles represent $Mn^{4+}$ and lobes depict $e_g$ orbitals of $Mn^{3+}$ ions (ref. 42).*

***h) Stripes in charge-ordered state:*** Charge and orbital ordering in manganates is reported to give rise to stripes [43,44]. In $La_{1-x}Ca_xMnO_3$ when $x = 0.5$ the number of $Mn^{3+}$ and $Mn^{4+}$ ions are same and this leads to diagonal stripes with a spacing of 11 Å. On the other hand, when $x = 0.67$ the number of $Mn^{4+}$ ions is twice that of $Mn^{3+}$ ions leading to the ordering of diagonal rows of $Mn^{3+}$ and $Mn^{4+}$ ions besides the orientational ordering of the orbitals. This in turn may lead to striped pattern with periodicity of 16.5Å (figs.1.12 a and b).

### 1.4.2 Electrical transport in rare earth manganates

Electrical transport in the manganates involves the transfer of electrons from $Mn^{3+}$ to $Mn^{4+}$ by double exchange. The manganates with $x < 0.5$ have a conduction band more than half-filled whereas those with $x > 0.5$ have a conduction band less than half-filled. When $x > 0.5$ the probability of ferromagnetic overlap leading to double exchange decreases and that of antiferromagnetism coupling increases. An

ordering of charge carriers leading to Coulomb interaction overcomes the kinetic energy localizing the electron, thus favoring insulating behavior.

Electrical transport properties of $Ln_{1-x}A_xMnO_3$ mirror the magnetic properties exhibiting low resistivities in the ferromagnetic region and insulating behavior in charge-ordered and antiferromagnetic regions. The magnetic transitions with very high resistivities for $x = 0$ minimum for $x = 0.3$ and maximum for other antiferromagnetic structures with $x > 0.5$. The number of charge carriers can be assumed to be equal to the $Mn^{4+}$ ion introduced into the lattice for small doping ($x \sim 0$). Instead, it is found experimentally that the conduction changes rather rapidly around a threshold corresponding to a dopant concentration of $x \approx 0.15$, suggesting that localization of charge carriers play an important role in electron transport properties at low doping levels. Charge ordering, even on a local scale, promotes localization of charge carriers. In $La_{1-x}Sr_xMnO_3$ series, for example, charge ordering occurs around $x = 0.125$ [45]. The electrical resistivity of a crystal with $x = 0.15$ is anisotropic with the in-plane resistivity being lower by a factor of 2 to 5 in comparison with resistivity along c-axis [46].

***a) Ferromagnetic state:*** The ferromagnetic state in $La_{1-x}Ca_xMnO_3$ is observed around $x = 0.3$. The composition is metallic and the evidence for metallic behavior comes from power law dependence of the resistivities at low temperatures where a $T^2$ [47-50] or $T^{2.5}$ dependence is reported [51]. This could be attributed to the correlation effect or spin wave scattering. The coefficient of the $T^2$ term derived from measurements on single crystals is consistent with strongly correlated electron metals. Only few compounds such as $La_{0.7}Sr_{0.3}MnO_3$ show residual resistivity

620.112 97
P03
JNCASR
Acc No. 3308
LIBRARY

expected for metals $\rho_0 = 1.5X10^{-6}\Omega m$ suggesting that the mean free path exceed the interatomic spacing [52]. In other compounds, the residual resistivity can be up to ten orders of magnitude greater, making them extremely peculiar metals. The $T^2$ variation is suppressed below 10-20 K [49] and in some cases slight upturn in $\rho$ is reported [53,54].

***b) Paramagnetic state:*** Electron transport properties of manganates in the region above the ferromagnetic transition temperature are anomalous. In most of the cases the resistivity in the high temperature paramagnetic regime follows an Arrhenius type activated behavior [55,56].

$$\rho = \rho_o \exp\left(\frac{E_o}{kT}\right)$$

where, $E_0$ is typically 0.1 eV. There is evidence for $\rho \propto T\exp(\frac{E_o}{kT})$ over an extended temperature range [48,50,57]. The common view is that the carriers form dielectric polarons [48,50]. The hopping motion of these polarons leads to a resistivity of the form

$$\rho = \left(\frac{kT}{ne^2 D}\right)\exp\left(\frac{E_o}{kT}\right)$$

where $n$ is the carrier density and $D$ is the polaron diffusion constant. The contribution to $E_o$ may originate from coulombic factors. Snyder et al [59] have performed an extended high temperature measurements on single crystals and thin films of calcium and strontium doped lanthanum manganates.

The presence of magnetic disorder above $T_c$ together with the intrinsic variations in the Coulomb potential due to the presence of $Ln^{3+}$ and $A^{2+}$ ion in the

lattice leads to the formation of the mobility edge [60]. At high temperatures, carriers from the Fermi energy ($E_F$) are excited to the mobility edge ($E_\mu$), giving an activated conductivity. At low temperatures it may be possible to discern a nearest-neighbour hopping process with a lower activation energy, which transforms into VRH with a $T^{-1/4}$ temperature dependence when the phonon energy is insufficient. This leads to long-range hops wherein the electron finds the site with small energy of activation. This is not incompatible with the small dielectric polaron model since VRH of the small polaron also leads to $T^{-1/4}$ dependence. For highly correlated electrons, a small gap appears at $E_F$ and the hopping law is then shows a $T^{-1/2}$ temperature dependence below the correlation gap [61]. For a range of ferromagnetic manganates, the resistivity data above $T_c$ could be fitted to a power law between 1/2 and 1/4. This same fractional power law can be extended to charge ordered and AFM regions [62].

***c) Magnetoresistance:*** Many solids exhibit a change in their resistance upon application of a magnetic field. A suitable change in the resistance upon application of a magnetic field is not surprising in manganates as magnetization (spins) and the resistivity (charge carries) are related.

The change in resistance to the initial resistance is referred to as magneto resistance (MR)

$$MR = \frac{\rho(H) - \rho(O)}{\rho(O)}$$

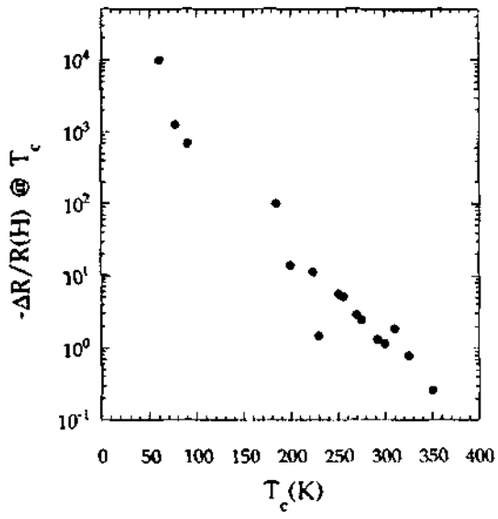


*Fig. 1.13 Variation of magnetoresistance as a function of $T_c$ (ref. 65).*

$\rho(H)$ is the resistivity in presence of an applied field and $\rho(0)$ is the resistivity in absence of any field.

Large magnetoresistance is linked to the presence of a critical concentration of $Mn^{4+}$ of around 30%, which can be introduced in $Ln_{1-x}A_xMnO_3$ by cation substitution at the A-site. This effect is inhibited by charge-ordering. The maximum effect is generally noticed around $T_c$. The decrease in the resistivity value with applied fields appear to be different above and below $T_c$. Above $T_c$, the magnetoresistance is not very large in small fields, and the curves are bell shaped showing a $\Delta\rho \propto H^2$ or $M^2$ [63]. Also, near $T_c$, the resistivity drops rather quickly and saturates at high fields, but at low fields, the effect is again small. Around $T_c$, $\Delta\rho$ varies roughly as $H^2$ but, others report a linear variation of $\Delta\rho$ with H [64]. It must also be mentioned that the MR and the $T_c$ are coupled by a universal relationship (Fig.1.13). The fact that large MR is observed for small $T_c$ values is not surprising for the following two reasons: first, since the transition to a metallic state

is from a semiconducting-like state and hence lower the $T_c$, the larger is the ρ just above $T_c$. Higher $T_c$, the greater the contribution from scattering due to phonons, magnons, and other electrons, which will set a lower bound on ρ in the metallic state and hence an upper bound on the MR [65]. The largest magnetoresistance observed seem to accompany first-order transitions. Low temperature measurements have shown the existence of a first-order transition between a high thermally activated resistivity and metallic-like state in a number of composition [66]. Large resistance ratios are related to cation size effects [36].

## 1.5 Layered Manganates

Layered structures of the formula $(AO)(Ln_{1-x}A_xMnO_3)_n$ are members of the Ruddelssden Popper series, consisting of perovskite units sandwiched between rocksalt AO layers. The end members of this series with $n = 1$ and $\infty$ correspond to the single layer $K_2NiF_4$ and the cubic perovskite structures, respectively.

Compounds corresponding to the formula $La_{1-x}Sr_{1+x}MnO_4$ have been extensively studied [67]. For all values of $x$, the $La_{1-x}Sr_{1+x}MnO_4$ series exhibit insulating behavior. The compositions close to 0.5 exhibits charge ordering around 250 K [68]. At lower temperature (~20 K), a spin-glass state is observed for $0.2 < x < 0.6$. For $x < 0.1$, compounds are anitferromagnetic below 100 K.

The $n = 2$ compounds show MR in $La_{2-2x}Sr_{1+2x}MnO_7$ [69] and $La_{2-2x}Ca_{1+2x}Mn_2O_7$ [70]. In Ca doped systems ($x$ ~0.25), a ferromagnetic $T_c$ of 215 K was identified but the MR peak was observed at a much lower temperature (100 K). The large discrepancy was attributed to the quasi-2D nature of the Mn-O layers.

In Sr substituted manganates, for $x$ = 0.4, two transitions were observed. The first transition was reported around 300 K which was ascribed to short-range 2D ordering and the second transition around 125 K to a long range ferromagnetic ordering. The resistivity in both $c$-axis and $a$-$b$ plane change from semiconducting to metallic around this temperature. The MR for this compound is much larger than for the 3D ($n = \infty$) system which supports the general trend of increasing MR with decreasing $T_c$. When the concentration of $A^{2+}$ ions is 30 % ($x$ = 0.3), $n$ = 2 systems show large anisotropy in its transport properties. Both magnitude and the form of the temperature dependence of ρ(T) are different along the two crystallographic directions.

The effect of different lanthanide ion substitution has also been studied for the double layer system $LnSr_2Mn_2O_7$ [71]. The substitution of smaller cations (Ln size < La) results in hysteresis reminiscent of a spin-glass behavior around 150 K. Also, a structural study for $0.55 \leq x \leq 0.75$ with Ln = La, Pr, Nd, Sm, Gd, Tb, Dy, Ho, Y and Er have established cation ordering between the two available cation sites with the smaller lanthanides preferring the site in between the double-layer block [72].

## 1.6 Phase Transition and phase control

### 1.6.1 Temperature induced phase transition

In a mixed-valent manganate of the type $Ln_{1-x}A_xMnO_3$ a drastic change in the magnetization behavior is observed by varying temperature [73]. In Fig. 1.14, we see three types of transitions. Néel temperatures (x-x′) are not accompanied by major resistivity changes and an activated behavior generally persists through the transition to the antiferromagnetic state.

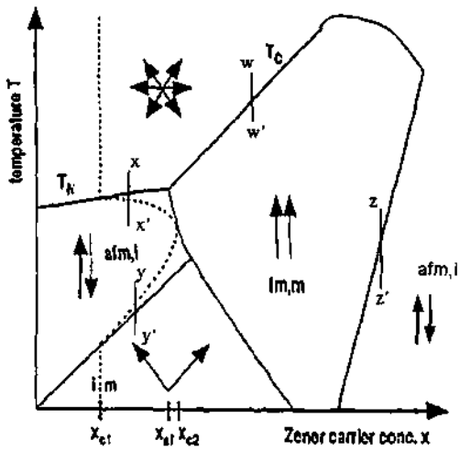


*Fig. 1.14 A schematic diagram of magnetic and eletrical phase diagram of $La_{1-x}A_xMnO_3$ (ref. 73).*

At Curie point, due to ferromagnetic ordering around w, the resistivities present large anomalies with associated CMR (w-w'). The electric and magnetic transitions are close to one another but may not coincide completely. A large discrepancy is observed for samples that are weakly crystalline with $T_{IM}$ lower than $T_c$.

The metal-insulator transitions in manganates are unusual, the low temperature phase being insulating. This has been ascribed to the magnetic nature of the transition. Large resistance changes can be observed at z-z' where a transition from a ferromagnetic to antiferromagnetic to a state is observed (Fig. 1.14). Large changes in the electron transport properties at such transition temperatures were first reported by DeGennes [74]. Resistance changes accompanying a re-entrant ferromagnetic transition is in the opposite direction.

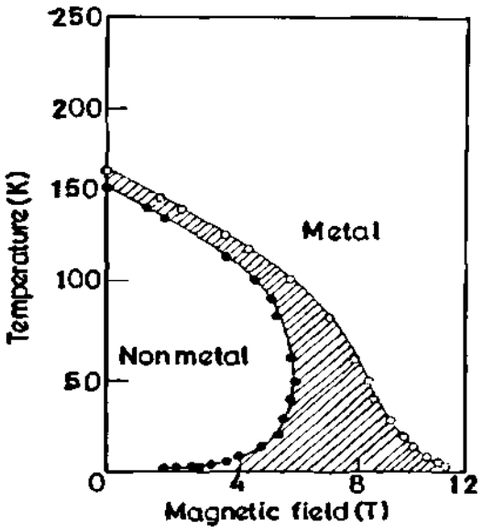


*Fig. 1.15 Magnetic phase diagram of $Nd_{0.5}Sr_{0.5}MnO_3$ showing the hysteresis at the first order phase transition (ref. 77).*

### 1.6.2 Magnetic field-induced phase transition

In mixed-valence manganate compositions close to an antiferromagnetic-ferromagnetic phase boundary show interesting properties as can be seen from the Fig.1.14. The compositions $x$~0.15 and 0.5 show interesting properties when subjected to an external magnetic field. These field-induced transitions are observed in ferromagnetic state where the magnetization (M1) is slightly higher in energy than the non-magnetic (paramagnetic) state associated with the magnetization M2. Under the influence of an external magnetic field, the former is stabilized due to the energy associated with the magnetic field $-\mu_o H(M1-M2)$. The transitions induced by magnetic fields are generally first-order and are usually associated with hysteresis.

Also, the effect of magnetic fields is large near the charge-ordered state wherein the external fields destroy charge ordering resulting in a FMM state [75].

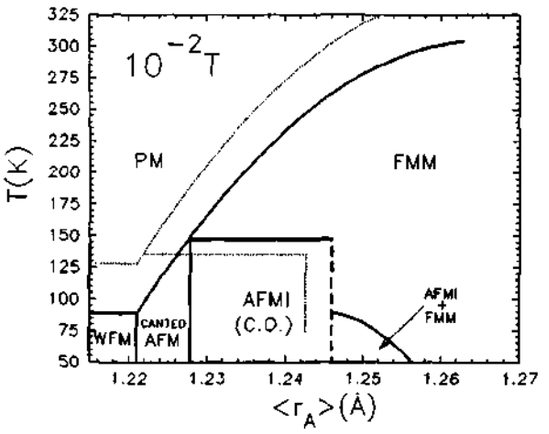


***Fig. 1.16*** *Magnetic phase diagram of $R_{0.5}Sr_{0.5}MnO_3$ compounds as a function of the average A-site cation radius (ref. 80).*

Tomioka et al [76-78] have described magnetic field effects in $x \approx 0.5$ compositions which order ferromagnetically at $T_c$ and then undergo a first-order transition at a lower temperature $T_{co}$ to a charge-ordered antiferromagnetic state [79]. These temperatures are 265 K and 140 K respectively for $Pr_{0.5}Sr_{0.5}MnO_3$ [76] and 255 K and 158 K respectively for $Nd_{0.5}Sr_{0.5}MnO_3$ [77]. Both have orthorhombic (O') structure, but the orthorhombic distortion is greater in the charge-ordered state. The large hysteresis in temperature or field at the first-order transition in $Nd_{0.5}Sr_{0.5}MnO_3$ is illustrated in Fig. 1.15.

The $Pr_{1-x}Ca_xMnO_3$ system differ from $Pr_{1-x}Sr_xMnO_3$ system as the former remains a semiconductor, with no value of $x$ leading to collinear ferromagnetic metallic phase in zero field. A strong tendency towards charge ordering impedes the tendency towards metallicity. Unlike $Nd_{0.5}Sr_{0.5}MnO_3$, the charge ordering and antiferromagnetism occur at different temperatures. When $x \approx 0.3$, there is a transition to a canted antiferromagnetic state around 100 K. Application of 4-6 T magnetic fields at 4.2 K transforms the insulating canted antiferromagnet

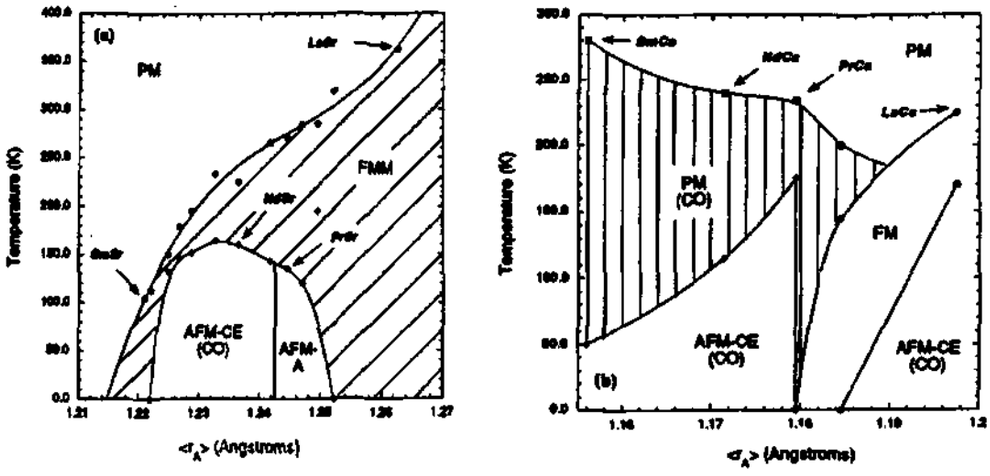


*Fig.1.17 Temperature-<$r_A$> phase diagram for a) $Ln_{0.5}Sr_{0.5}MnO_3$ b) $Ln_{0.5}Ca_{0.5}MnO_3$ (ref. 42).*

to a metastable ferromagnetic metal, with a change in resistivity of ten orders of magnitude. The complex behavior of the manganates with $x$ = 0.5 has been summarized by Damay et al [80] in a phase diagram based on average A-site cation size (Fig. 1.16). Effect of the magnetic field on the phase transition is shown by the dotted curves.

### 1.6.3 Bandwidth and bandfilling (pressure effects)

From the point of view of a single-electron band conduction, the parameters that define the properties of the compound are bandfilling and bandwidth. As the number of $Mn^{3+}$ ions varies with the substitution at the A-site, there is a corresponding change in the bandfilling across the series. Alternatively, the average size of the A-site cation, <$r_A$>, in the $ABO_3$ formula can be varied, resulting in the alteration of the lattice constant and thus the one-electron bandwidth. Bandwidth studies in manganates has been focused on $La_{0.7-x}Pr_xCa_{0.3}MnO_3$, wherein the Ca

concentration is fixed resulting in the constant number of charge carriers but, there is a systematic decrease in the $<r_A>$ with increase in the Pr concentration resulting in a decrease in $T_c$ [11]. The bandwidth phenomenon appears to be universal, and such behavior has been shown in the insulating phases of $LnNiO_3$. In rare earth manganates also, drastic changes due to $<r_A>$ is observed in charge-ordered and AFM transitions (Fig. 1.17).

It must be noted that, varying the lanthanide radius (in general, $<r_A>$) is equivalent to varying the internal pressure. This is usually termed as chemical pressure which is complementary to the external hydrostatic pressure. Moritomo et al [81] have shown that the resistivity and $T_{IM}$ of $La_{1-x}Sr_xMnO_3$ strongly depends on the concentration for a fixed pressure of 18 kbar. Similar experiments have proved the dependence of $T_c/T_{IM}$ on external pressure in $La_{1-x}Ca_xMnO_3$ [82]. The increase in $T_c$ with pressure as $x$ decreases is presumably related to an increasing sensitivity of $T_c$ towards pressure. Hwang et al have successfully established the effect of internal pressure on the $T_c$ of the solid solutions of $Pr_{0.7}Ca_{0.3}MnO_3$ and $La_{0.7}Ca_{0.3}MnO_3$ compositions [11]. In both the internal and external pressure studies there is an increase in the Mn-O-Mn bond angle towards 180° with increase in $<r_A>$ or external pressure. Thus, increasing the electron hopping matrix element and consequently the bandwidth. Hence, the $T_c$-$<r_A>$ relationship is consistent with a transition which is driven by the kinetic energy gain of the carriers on entering the metallic state. Ideally, intention of an experimental work is to keep either bandfilling ($x$) or bandwidth (W) constant, in practice both are varied at the same time. In order to view the interconnected nature of the experimental parameters in terms of

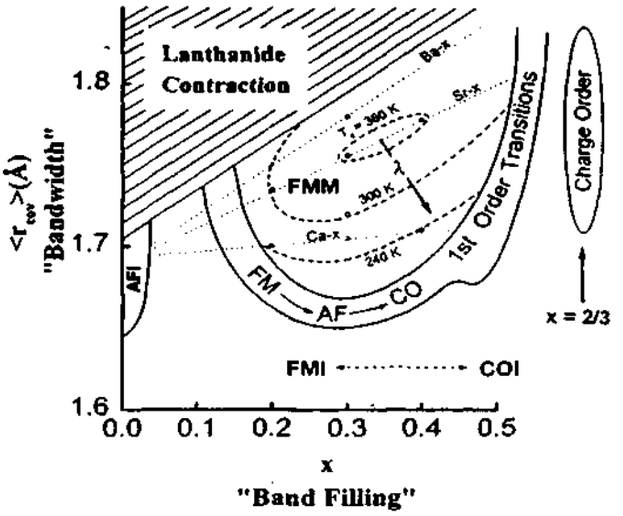


*Fig. 1.18 Phase diagram in the plane defined by average A-site radius and divalent ion concentration, x. The dashed lines show the effect of Sr, Ca and Ba substitution. The bold arrow indicates the electron-phonon coupling (ref. 1).*

microscopic variables, it is useful to plot $T_c$ of the different phases on a plot of $x$ and $<r_A>$ as in Fig. 1.18.The FM ground state is obtained in a region of the $x$-$<r_A>$ space bounded above by a large size $La^{3+}$ ion, and below by a series of transitions into CO, AF and spin-glass states which are strongly coupled to the lattice distortions.

### 1.6.4 Cation size disorder

It has been amply demonstrated that $<r_A>$ plays an important role in determining the properties of manganates such as ferromagnetism and charge ordering. While $T_c$ and $T_{IM}$ increase with $< r_A >$, the value saturates at high $<r_A>$, probably due to mismatch resulting from A-site cation size. The effect arising from the size mismatch of the A-site cation on the $T_c$ or $T_{IM}$ has been analysed by employing variance in the distribution of $< r_A >$. The variance $\sigma^2$ is defined as

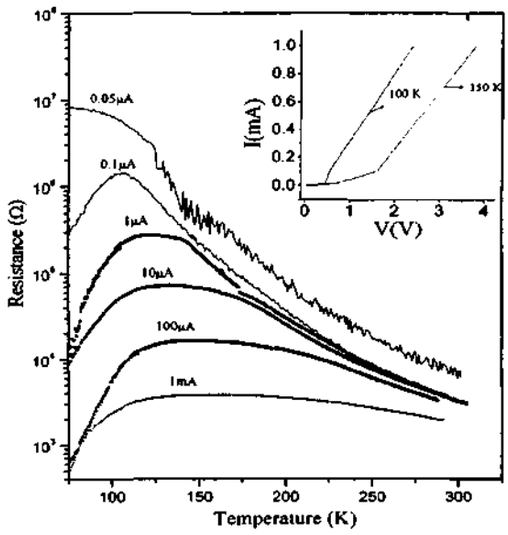


***Fig.1.19*** *Electric current induced insulator-metal transition in $Nd_{0.5}Ca_{0.5}MnO_3$ film deposited on Si(100) substrate. Inset shows non linear behavior of I-V curves (ref. 86).*

$$\sigma^2 = \Sigma x_i r_i^2 - \langle r_A \rangle^2$$

where, $x_i$ is the fractional occupancy of A-site ions and $r_i$ is the corresponding ionic radii. Such mismatch effects on the ferromagnetic $T_c$ [83] as well as charge ordering temperatures [84] have been studied on a series of manganate compositions. In $Ln_{1-x}A_xMnO_3$ ($x = 0.3$) for fixed $< r_A >$, a linear relationship exists between $T_c$ and $\sigma^2$, where a decrease in the $T_c$ is observed with increase in the $\sigma^2$. Similar disorder effects have been studied on $Ln_{0.5}A_{0.5}MnO_3$ (where Ln = rare earth; A = alkaline earth), in order to understand the influence of variance on charge ordering. The measurements on two series of manganates with fixed $< r_A >$, of 1.17 and1.24 Å reveal an insensitivity of $T_{co}$ towards A-site disorder. It must be mentioned that the manganates with $< r_A >$ 1.17 Å show only charge ordering and $< r_A >$ of 1.24 Å exhibit both ferromagnetism and charge ordering.

### 1.6.5 Electric field effects

On application of high voltages, Tokura et al [85] were able to induce a metastable low resistive states in charge-ordered manganates at low temperatures. Further experimentation on electric field-induced phase transition in series of charge-ordered manganates was performed by Rao and co-workers [86,87] to show that a constant current passing through a charge-ordered manganate could drive the system from a robust charge-ordered state to a metallic-like conductive state (Fig. 1.19). They also established low temperature switching and memory effects associated with these manganates under the influence of constant current. Thin film of rare earth manganates, with co-existing ferromagnetic and charge-ordered phases, show current-induced effects which have been attributed to a percolative behavior.

Current-induced changes in the resistivity is also observed in the manganates, exhibiting insulator-metal transition such as in $La_{0.82}Ca_{0.12}MnO_3$ [88], The current effects are manifested at low temperatures where there is a dominant insulating behavior. Thin films of $La_{0.8}Sr_{0.2}MnO_3$ also show negative differential resistance (NDR) at room temperatures, which also exhibits a thickness dependence [89].

Rao and co-workers have studied the magnetic signature associated with negative differential resistance, which occurs below the antiferromagnetic transition. They have measured both magnetization and I-V characteristics simultaneously by employing a high $T_c$ rf SQUID. They have found that, as the sample enters the NDR regime, there is a rise in the magnetization of the sample indicating the onset of ferromagnetic correlations. They propose that the onset of

NDR results in an appearance of metallic filaments which carry most of the current and the volume fraction of the filament increases with the current, which sustains the NDR regime [90].

In general, current-induced changes in the resistivity behavior are attributed to the dielectric breakdown leading to conductive paths (filamentary paths) which tend to grow with increasing current and these conductive paths have been shown to be ferromagnetic.

### 1.6.6 Radiation-induced phase transition

Since, the break down of the charge-ordered state could be induced by both magnetic and electric fields separately, it was obvious a coupled electromagnetic field should show similar trends. Indeed such electromagnetic radiation-induced phase transitions are reported.

A single nanosecond pulsed laser (2.4 eV) with a photon energy greater than the charge gap has been shown to decrease the resistance of a charge-ordered manganate also resulting in a large persistent photoconductivity [91]. Such local light-induced current paths are obtained due to the local melting of the charge/orbital ordered states. Also, these metallic paths can be sustained by passing electrical currents. It has been established by pump-probe experiments that the photo-induced melting of charge/orbital-ordered state or the local insulator-metal transition is completed within 1 ps and is associated with a large change in the optical reflectivity of the sample.

X-rays, on the other hand, offer a powerful source to obtain insulator-metal transitions. A six order increase in the conductance was noted when the X-rays were exposed between two contacts spaced ~1mm apart for 20 min.

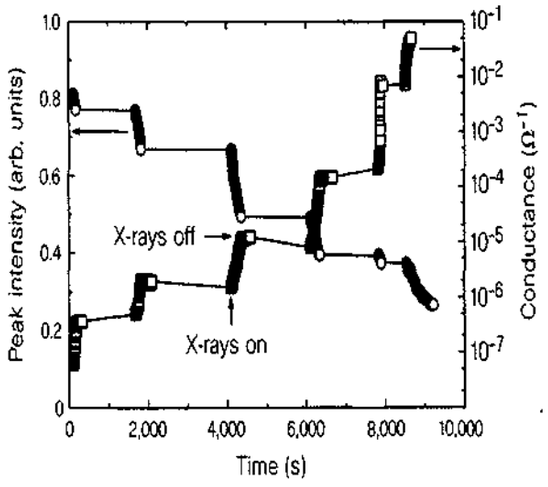


***Fig. 1.20** Effect on incident X-rays on the conductance and peak intensities in $Pr_{0.7}Ca_{0.3}MnO_3$ (ref. 92).*

Conductivity could be measured even after the X-rays were turned off without any measurable degradation. One could see continuos decrease of reflected intensity with X-ray illumination. Such changes were not noticed when the X-rays were turned off (Fig.1.20).

Another interesting aspect is the linear and non-linear conductivity obtained depending upon the exposure time, linear (ohmic) conductivity were observed for long exposures and non-linear for short exposure times. The non-ohmic conductivity is attributed to the current switching behavior. Annealing of the sample to temperatures above 60 K resulted in disappearance of the X-ray induced effects [92].

It is quite clear that magnetic field and pressure change global properties, current-induced effects and illumination of light and X-rays causes metastable phase transitions. The metastable phases resulting from local change is due to phase

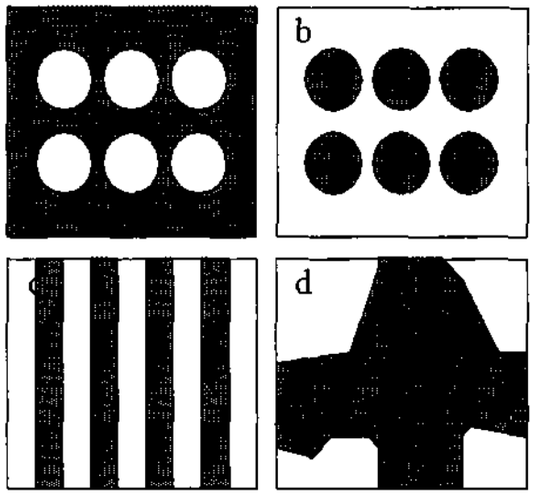


***Fig. 1.21*** *Microscopic phase-separated state giving rise to* ***a)*** *a conducting state with insulating droplets,* ***b)*** *an insulating state with a ferromagnetic droplet,* ***c)*** *charge-stripes,* ***d)*** *macroscopic phase separation involving large portion of conducting ferromagnetic phase.*

separation. The percolation conductivity in such metastable phases forms an intrinsic feature of doped manganates.

## 1.7 Phase Separation

It is evident from the previous section that the different phases that can be induced in rare earth manganates are governed by both external and internal factors. A careful manipulation of these factors can induce different phases under one condition. The coexistence of more than one phase at a particular temperature is termed as phase separation. It is generally assumed that a monophasic (or a single crystal) is pure with exact composition and a well-defined set of properties. This is not true in the case of transition metal oxides, especially manganates where such electronic inhomogeneties are encountered in many compositions. The phase separation in $Ln_{1-x}A_xMnO_3$ display a variety of effects giving rise to novel

electronic and magnetic properties. The Jahn-Teller distortion associated with the $Mn^{3+}$ ions and charge ordering of $Mn^{3+}$ and $Mn^{4+}$ ions compete with double exchange and promote the insulating behavior and antiferromagnetism [93]. The nature of phase separation in the manganates depends on the average size of the A-site cations, carrier concentration or the composition (value of $x$), temperature and other external factors such as magnetic, electric and electromagnetic fields. There are indications that unusual magnetic and transport properties of oxide materials arise from phase separation [94].

Thermodynamic equilibrium phase separation is distinct from phase separation caused by inhomogeneties in chemical composition, such as those due to non-uniformity in impurity distribution, as it can have an electronic origin or could also arise from the presence of magnetic impurities. Such phase separation can be controlled or changed by external factors. In electronic phase separation, the concentration of charge carriers giving rise to ferromagnetism and/or metallicity in a part of the crystal causes mutual charging of the two phases. This gives rise to strong Coulomb fields, which may mix the conducting ferromagnetic and insulating antiferromagnetic phases in order to lower the Coulomb energy.

When the carrier concentration is small, the conducting ferromagnetic regions are separated forming droplets as in Fig. 1.21b At higher carrier concentrations, the volume of the ferromagnetic phase increases rendering the droplets to coalesce, giving rise to a situation shown in Fig. 1.21d. Another important aspect of phase separation is the impurity phase separation which is essentially caused by the following factor: formation of impurity metal-like regions due to interaction between the doped impurities driven by Mott mechanism.

Although such impurity concentrations should be less than critical concentration of the impurity which results in a uniform distribution of the dopant. The interaction between the charge carriers associated with impurity concentration might result in ferromagnetism as in the case with electronic phase separation. The essential feature distinguishing the impurity phase separation from electronic phase separation is the absence of mutual charging of the phases at these impurity phases separated regions. As a result, the ferromagnetic regions can be obtained even at small carrier densities.

Microscopically homogeneous clusters are usually of the size of 1-2 nm in diameter dispersed in an insulating or charge-localized matrix as seen in figure 1.21a. Such a phase-separation scenario bridges the gap between the double exchange model and the lattice distortion model. Recent literature shows that in addition to microscopic phase separation there can also be mesoscopic phase separation whereby the length scale is between 30-200 nm, arising from the comparable energies of the ferromagnetic metallic and antiferromagnetic insulating states. In certain manganate compositions, mesoscopic as well as microscopic phase separation has been observed. In La-Pr-Ca-Mn compositions and other manganates, the occurrence of multiple phases has also been noticed [95,96]. The techniques used to identify phase separation in different length scales vary. For example, diffraction techniques can be used to examine macroscopic phase separation (Fig. 1.21d), for which distinct features occur in the diffraction patterns due to the different phases in the system. Techniques such as NMR spectroscopy, on the other hand, give information on the local environment at a microscopic level. Also,

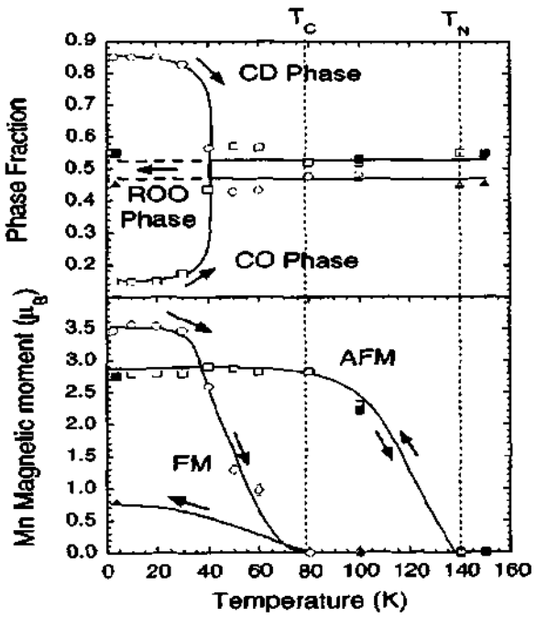


*Fig. 1.22 Phase fraction and magnetic moments of $Pr_{0.7}Ca_{0.3}MnO_3$ obtained from Rietveld refinements of neutron data (from ref. 95).*

transport measurements, under favorable conditions can provide valuable information on phase separation.

### 1.7.1 Some examples

Mesoscopic phase separation in $Pr_{0.7}Ca_{0.3}MnO_3$ has been observed by neutron scattering measurements. Intragranular strain-driven mesoscopic phase segregation (5-20 nm) between two insulating phases (one charge-ordered and another spin-glass) occurs below $T_{co}$. The charge-ordered phase is antiferromagnetic while the other is a spin-glass. On the application of a magnetic field, most of the material transforms into FM state. Microscopic phase separation (0.5-2 nm) is present at all temperatures, especially in the spin-glass phase at low temperatures. These results are shown in the form of a phase diagram in Fig.1.22.

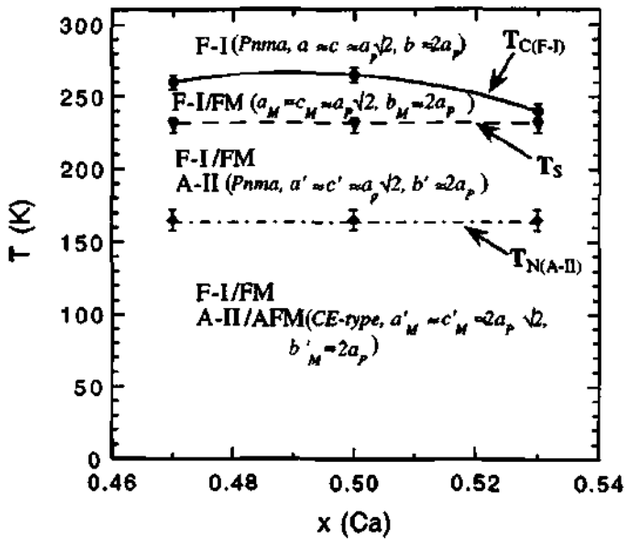


***Fig. 1.23** Phase diagram of $La_{1-x}Ca_xMnO_3$ in the composition range $0.47 \leq x \leq 0.53$ (from ref. 97).*

$La_{0.5}Ca_{0.5}MnO_3$ changes to a FM phase on cooling to 220 K ($T_c$) and then to a charge-ordered AFM phase around 150 K ($T_{co}$). This manganate is best described as magnetically phase separated over a wide range of temperatures [97,98]. At low temperatures ($T < T_{co}$), FM metallic domains are trapped in charge-ordered AFM matrix, giving rise to percolative metallic conduction. The fraction of the FM phase at low temperatures is highly dependent on the thermal treatment. Even within the FM phase, in the $T_{co} < T < T_c$ region, there is phase separation. A second crystallographic phase, probably without magnetic order, has been identified [98].

The phase diagram of $La_{1-x}Ca_xMnO_3$ in the $0.47 \leq x \leq 0.5$ range (Fig. 1.23) reveals the nature of the phase separation. Magnetization studies show three phase separated regimes: $T_c > T > T_o$, $T_o > T > T_{co}$ and $T < T_{co}$, in which $T_o$ is the onset temperature below which the cooling field plays an unbalancing role in favor of the FM state [97].

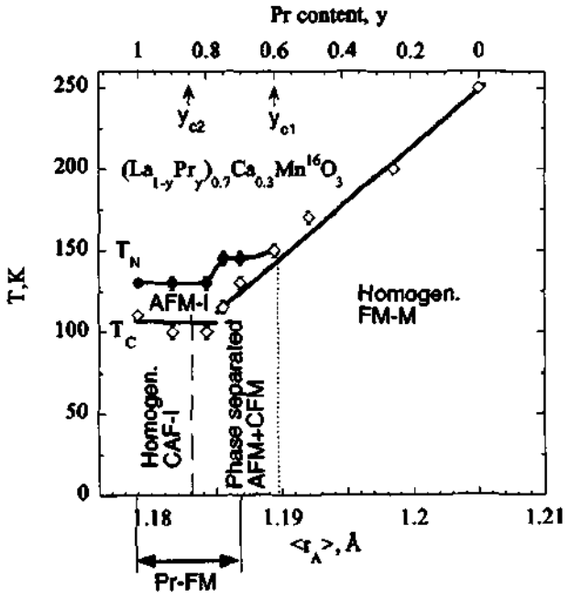


*Fig. 1.24 Phase diagram of $(La_{1-y}Pr_y)_{0.7}Ca_{0.3}MnO_3$. The diamonds and circles show $T_c$ and $T_N$ values (ref. 96).*

It is in the last regime that minority FM domains are embedded in the AFM matrix. In the first regime near the $T_c$, the FM phase grows freely with the application of a magnetic field.

$La_{5/8-y}Pr_yCa_{3/8}MnO_3$ shows tendency towards submicron sized phase separation involving ferromagnetic and charge-ordered antiferromagnetic domains. By varying y, the volume fraction and the domain size of ferromagnetic and charge-ordered domains can be varied. The electrical conduction in these manganates occurs through a percolative mechanism involving infinitely connected grains [99]. The phase diagram shows the dependence of different phases on the fraction of Pr content and also on the cation radius (Fig. 1.24)[97].

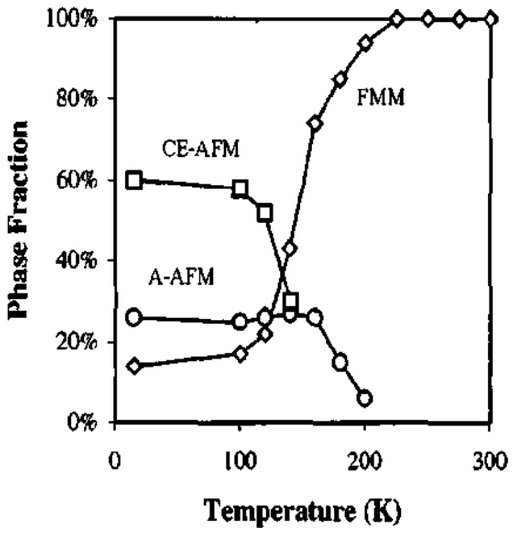


***Fig. 1.25*** *Variation in the percentage of the different phases of $Nd_{0.5}Sr_{0.5}MnO_3$ with temperature(ref. 100).*

High-resolution X-ray and neutron diffraction investigations have shown that $Nd_{0.5}Sr_{0.5}MnO_3$ separates into three macroscopically different phases at low temperatures. The phases involved are high temperature ferromagnetic metallic phase, the orbitally ordered A-type antiferromagnetic phase and the charge-ordered CE-type antiferromagnetic phase [100].

The A-type antiferromagnetic starts to manifest itself around 220 K, with the charge-ordered antiferromagnetic phase appearing around 150 K (as expected). At the so-called ferromagnetic/charge-ordered transition temperature, three phases co-exists, and this situation continues down to very low temperatures (Fig. 1.25).

In $La_{2-2x}Sr_{1+2x}MnO_7$ ($0.45 \geq x \geq 0.6$) a reentrant CO transition are observed due to the competition between charge ordering and ferromagnetism [101]. A competition between antiferromagnetism and ferromagnetism at low temperatures in $La_{1.2}Sr_{1.8}Mn_2O_7$ at 40 K results in a reentrant spin-glass behavior, which results

in phase separation and canted antiferromagnetism. A pressure-induced segregation into electron-rich FM and electron poor AFM $Mn_2O_7$ layers has been observed in $La_{2-2x}Sr_{1+2x}Mn_2O_7$ ($x$=0.32); the segregation can be considered as a first-order inversion of the exchange coupling between the FM $Mn_2O_7$ layers [102].

## 1.8 References


1. S. Jin, T.H. Tiefel, M. McCormack, R.A Fasthacht, R. Ramesh and L.H.Chen, Science, 264, 413, 1994; *Colossal magnetoresistance, charge ordering and related properties of manganese oxides*, Eds, C.N.R. Rao and B. Raveau (World Scientific, Singapore, 1998); *Colossal magnetoresistive oxides*, Y. Tokura (Gordon and Breach Sci Pub, Amsterdam, 2000). A. P. Ramirez, *J. Phys.: Condens. Matter*, 9, 8171, 1997.
2. G. H. Jonker and J. vanSanten, *Physica*, 16, 337, 1950.
3. J. vanSanten and G. H. Jonker, *Physica*, 16, 599, 1950.
4. J. Volger, *Physica*, 20, 49, 1954.
5. R. vonHelmholt, J. Wecker, B. Holzapfel, L. Schultz and K. Samwer, *Phys. Rev. Lett.*, 71, 2331, 1993.
6. K. Charara, T. Ohno, M. Kasai and Y. Kozono, *Appl. Phys. Lett.*, 63, 1990, 1993.
7. *Geochemistry*, V. Goldschmidt (Oxford University Press, 1958).
8. *Magnetism and the chemical bond*, J.B. Goodenough (Wiley Interscience, New York, 1996).
9. E. J. W Verway and J. H. DeBoer, *Rechl. Trav. Chim. Pays-Bas Belg.*, 55, 531,1936.
10. R. J. H. Vookhoeve, J. P. Remeika, L. Trimble, A. Cooper, F. Disalvo and P. Gallagher, *J. Solid. State. Chem.*, 14, 395, 1995.
11. H. Y. Hwang, S. W. Cheong, P. G. Radaeli, M. Marezio and B. Batlogg, *Phys. Rev. Lett.*, 75, 914, 1995.

12. R. Mahendiran, R. Mahesh, N. Rangavittal, S. Tiwari, A. Raychaduri, T. V. Ramakrishnan and C.N.R. Rao, *Phys. Rev.*, B 53, 3348, 1996.

13. J. L. Garcia-Munuz, J. Fontucuberta, B. Martinez, A. Seffer, S. Pinol and X. Obradors, *Phys. Rev.*, B 55, R668, 1997.

14. Q. A. Huang, A. Santoro, J. W. Lynn, R.W. Erwin, J. A. Borchers, J. L. Peng and R. L. Greene, *Phys. Rev.*, B 55 14987, 1997.

15. J. L. Garcia-Munoz, J. Fontcuberta, M. Suaaidi and X. Obradors, *J. Phys.: Condens. Matter*, 8, L787, 1996.

16. N. Sharma, A. K. Nigam, R. Pinto, N. Venkataramani, S. Prasad, G. Chandra and S.P. Pai, *Phys. Rev.*, B 53, 8992,1996.

17. J. Kanamori, *J. Phys. Chem. Solids*, 10, 87, 1959.

18. Y. Okimoto, T. Katsufuji, T. Ishikawa, A. Urushibara, T. Arima and Y. Tokura, *Phys. Rev. Lett.*, 75, 109, 1995.

19. J. Zaanen, G. A. Sawatzky and J. W. Allen, *Phys. Rev. Lett.*, 55,418, 1985.

20. E. O. Wollan and W. C. Koehler, *Phys. Rev.*, 100, 545,1955.

21. G. H. Jonker, *Physica*, 22, 707, 1956.

22. C. Zener, *Phys. Rev.*, 81, 440, 1951.

23. P. W. Anderson and H. Hesagawa, *Phys. Rev.*, 100, 675, 1955.

24. J. R. Cullen and E. Collan, *Phys. Rev.*, 7, 397, 1973.

25. J. B. A. A. Elemans, K. R. van Laar, K. R. vanDer Veen, and B. O. Loopstra, *J. Solid. State. Chem.*, 3, 238,1971.

26. E. E. Havinga, *Philips Res. Rep.*, 21,432, 1966.

27. J. Fontcuberta, B. Maritnez, A. Seffar, S. Pinol, J. L. Garcia-Munoz and X. Obradors, *Phys. Rev. Lett.*, 76, 1122, 1996.

28. J. Fontcuberta, B. Maritnex, A. Seffar, S. Pinol, J. L. Garcia-Munoz and X. Obradors, *Europhys. Lett.*, 34, 379, 1996.

29. J. R. Sun, G. H. Rao, J. K. Liang and W. Y. Zhou, Appl. Phys. A, 69, 3926, 1996.

30. R. M. Thomas, L. Ranno and J. M. D. Coey, *J. Appl. Phys.*, 81, 5763, 1997.

31. J. Topfer and J. B. Goodenough, *J.Solid. State. Chem.*, 130, 117, 1997.

32. W. H. McCarroll, K. V. Ramanujachary and M. Greenblath, and M. Cosandey, *J. Solid. State. Chem.*, 136, 322,1999.

33. J. Blasco, J. Garcia, J. M. DeTeresa, M. R. Ibarra, J. Perez, P. A. Algarabel, C. Marquina and C. Ritter, *Phy. Rev.*, B 55, 8905, 1997.

34. A. Maignan, C. Martin and B. Raveau, *Z. Phys.* B, 102, 19, 1997.

35. A. Barnabe, A. Maignan, M. Hervieu and B. Raveau. *Euro. Phys. J.* B1, 145, 1998.

36. P. V. Vanitha, A. Arulraj, A. R. Raju and C. N. R. Rao, *C. R. Acad. Sci. Paris*, 2, 595, 1999.

37. S. K. Singh, S. Palmer, D. M. Paul and M. R. Lees, *Appl. Phys. Lett.*, 69, 263, 1996.

38. H.L. Ju and H. Sohn, *J. Magn. Magn. Mater.*, 167, 200, 1992.

39. P. M. Woodward, T. Vogt, D.E. Cox, A. Arulraj, C. N. R. Rao, R. Karen and A. K. Cheetham, *Chem. Mater.*, 1998, 10, 3652.

40. K. Hirota, N. Kaneko, A. Nishizawa and Y. Endoh, *J. Phys. Soc.* Japan, 65, 3736,.1996.

41. F. Moussa, M. Hennion, J. Rodriguez-Carvajal, H. Moudden and A. Revcolevschi, *Phys. Rev.*, B 54, 15149, 1996.

42. C. N. R. Rao, *J. Phys. Chem.* B 104, 5877, 2000; Y. Tokura and N. Nagaosa, *Science*, 288, 462, 2000.

43. S. W. Cheong and C.H. Chen, in *Colossal magnetoresistance, charge ordering and related properties of manganese oxides*; Eds, C. N. R. Rao and B. Raveau ( World Scientific: Singapore, 1998).

44. S. Mori, C. H. Chen, S. W. Cheong, *Nature* (London), 392, 473, 1998.

45. Y. Yamada, O. Hino, S. Nohdo, R. Kanao, T. Inami and S. Katano, *Phys. Rev. Lett.*, 77, 904, 1996.

46. A. Anane, C. Dupas, K. LeDang, J. Renard, P. Veillet, A. Revcolevschi and A. G. M. Jansen, *J. Magn. Magn. Mater.*, 165, 377, 1997.

47. A. Urushibara, Y. Moritomo, Y. Tomioka, T. Arima and Y. Tokura, *Phys. Rev.*, B 51, 14103, 1995.

48. G. J. Snyder, R. Hiskes, S. DiCarolis, M. R. Beasley and T. H. Geballe, *Phys. Rev.*, B 53, 14434, 1996.

49. M. Jaime, P. Lin, M. B. Salamon and P. D. Han, *Phys. Rev.*, B 58, R5901, 1998.

50. G. Jakob, W. Westerburg, F. Martin and H. Adrian, *Phys. Rev.*, B 58, 14966, 1998.

51. J. M. DeTeresa, M. R. Ibarra, J. Blasco, J. Garcia, C. Marquina, P. Algarabel, Z. Arnold, K. Kamenez, C. Ritter and R. vonHelmholt, *Phys. Rev.*, B 54, 1187, 1996.

52. *Metal-insulator transitions* N. F. Mott ( Taylor and Francis, London, 1985).

53. K. Khazeni, Y. X. Jia, V.H. Crespi, M. L. Cohen and A. Zettl. *Phys. Rev. Lett.*, 76, 295, 1996.

54. J.-S. Zhou, W. Archibald and J. B. Goodenough, *Phys. Rev.*, B 57, R2017, 1998.

55. M. F. Hundley, M. Hawley, R. Hawley, R. H. Heffner, Q. X. Jia, J. J. Neumeier and J. Tesmer, *Appl. Phys. Lett.*, 67, 860, 1995.

56. G. C. Xiong, S. Bhagat, Q. Li, M. Domingnez, H. Ju, R. Greene and T. Venkatesan, *Solid. State. Commun.*, 97, 599,1996.

57. N-C, Yeh, C. C. Fu, J. Y. T. Wei, R. P. Vasquez, *J. Appl. Phys.*, 81, 97, 1997.

58. R. R. Heikes, R. C. Millerand, R. Mazelsky, *Physica*, 30, 1600, 1962.

59. G. J. Synder, M. R. Beasley and T. H. Geballe, *Mater. Res. Symp. Proc.*, 401, 541, 1995.

60. *Electronic processes in non-crystalline materials*, N. F. Mott and E. Davies ( Oxford University Press, 1971).

61. *Electronic properties of doped semiconductors*, B. I. Shklovskii and A. L. Efros ( Springer, Berlin, 1984).

62. K. V. Sarathy, S. Parashar, A. R. Raju and C. N. R. Rao, *Solid. State. Sci.*, 4, 353, 2002.

63. C. L. Canedy, K. B. Ibsen, G. Xiao, J. Z. Sun, A. Gupta and W. J. Gallagher, *J. Appl. Phys.*, 79, 4546, 1996.

64. K. Li, L. Liu, J. Sun, X. J. Xu, J. Rang, X. W. Cao, J. S. Zhu and Y. H. Zhang, *J. Phys.* D., 29, 14, 1996.

65. M. R. Lees, J. Barrat, G. Balakrishnan and D. M. Paul, *Phys. Rev.*, B 52, 14303, 1995,

66. A. Maignan, C. Simon, V. Caignaert and B. Raveau, *Solid. State. Commun.*, 96, 623, 1995.

67. Y. Moritomo, Y. Tomioka, A. Asamitsu, Y. Tokura and M. Matsui, *Phys. Rev.*, B 51, 3297, 1995.

68. B. J. Sternlieb, J. P. Hill, V. C. Wildgurber, G. M. Luke, B. Nachumi, Y. Moritomo and Y. Tokura, *Phys. Rev. Lett.*, 766, 2169, 1996.

69. Y. Moritomo, A. Asamitsu, H. Kuwahara, Y. Tokura, *Nature*, 380, 141, 1996.

70. H. Asano, J. Hayakawa and M. Matsui, *Appl. Phys. Lett.*, 68, 3638, 1996.

71. R. Seshadri, C. Martin, A. Maignan, M. Hervieu, B. Raveau and C. N. R. Rao, *J. Mater. Chem.*, 6, 1585, 1996.

72. P. D. Battle, M. A. Green, N. S. Laskey, J. E. Milburn, L. Murphy, M. J. Rosseinsky, S. P. Sullivan and J. F. Fvente, *Chem. Mater.*, 9, 552, 1996.

73. VonHelmholt, J. Wecker, K. Sanwer and K. Bahrner, *J. Magn. Magn. Mater.*, 151, 411, 1995.

74. P. G. DeGennes, *Phys. Rev.*, 188, 141, 1960.

75. Y. Tokura, Y. Tomioka, H. Kuwahara, A. Asamitsu, Y. Moritomo and M. Kasai, *Physica* C, 263, 544, 1996.

76. Y. Tomioka, A. Asamitsu, Y. Moritomo, H. Kuwahara and Y. Tokura, *Phys. Rev. Lett.*, 74, 5108, 1995.

77. H. Kuwahara, Y. Tomioka, A. Asamitsu, Y. Moritomo and Y. Tokura, *Science*, 270, 961, 1995.

78. Y. Tokura, H. Kuwahara, Y. Moritomo, Y. Tomioka and A. Asamitsu, *Phys. Rev. Lett.*, 76, 3184, 1996.

79. K. Knizek, Z. Jirak, E. Pollertz and F. Zounova, *J. Solid. State. Chem.*, 100, 292, 1992.

80. F. Damay, A. Maignan, C. Martin and B. Raveau, *J. Appl. Phys.* 81. 1372, 1997.

81. Y. Moritomo, A. Asimitsu and Y. Tokura, *Phys. Rev.* B 51, 16491, 1995.

82. J. J. Neumeier, M. F. Hundley, J. D. Thompson and R. H. Heffner, *Phys. Rev.*, B 52, R7006, 1995.

83. L. M. Rodriguez-Martinez and J. P. Attfield, *Phys. Rev.*, B 54, 2426, 1996.

84. P. V. Vanitha, P. N. Santhosh, R. S. Singh, C. N. R. Rao and J. P. Attfield, *Phys. Rev.*, B 59, 13539, 1999.

85. A. Asamitsu, Y.Tomioka, H.Kuwahara and Y. Tokura, *Nature*, 388, 50, 1997.

86. V. Ponnambalam, S. Parashar, A. R. Raju and C. N. R. Rao, *Appl. Phys. Lett.*, 74, 206, 1999.

87. C. N. R. Rao, A. R. Raju, V. Ponnambalam, S. Parashar and N. Kumar, *Phys. Rev.*, B 61, 594, 2000.

88. Y. Yuzhelevski, V. Markovich, V. Dikovsky, E. Rozenberg, G. Gorodetsky, G. Jung, D. A. Shulyatev and Ya. M. Mukovskii, *Phys. Rev.*, B 64, 224428, 2001.

89. A. K. Debnath and J. G. Lin, *Phys. Rev.* B 67, 064412, 2003.

90. A. Guha, N. Khare, A. K. Raychaudhuri and C. N. R. Rao, *Phys. Rev.*, B 62, R11941, 2000.

91. K. Miyano, T. Tanaka, Y. Tomioka, and Y. Tokura, *Phys. Rev. Lett.*, 78, 4257, 1997.

92. V. Kiryuklin, D. Casa, J.P. Hill, B. Keimer, A. Vigilante, Y. Tomioka and Y. Tokura, *Nature*, 384, 813, 1992.

93. C. N. R. Rao, P. V. Vanitha and A. K. Cheetham, *Chem. Eur. J.*, 3, 9, 2003.

94. E. Dagatto, T. Hotta and A. Moreo, *Phys. Rep.*, 1, 344, 2001.

95. P.G. Radelli, R.M. Ibberson, D. N. Argyriou, H. Casalta, K. H. Anderson, S. W. Cheong and J. F. Mitchell, *Phys. Rev.*, B 63, 172419, 2001.

96. A. M. Balagurov, V. Yu. Pomjakushin, D. V. Sheptyakov, V. L. Aksenov, P. Fisher, L. Keller, O. Yu. Gorbenko, A. R. Kaul and N.A. Babushkina, *Phys. Rev.*, B 64, 024420, 2001.

97. R.S. Freitas, L. Ghivelder, P. Levy and F. Parisi, *Phys. Rev.*, B 65, 104403, 2002.

98. Q. Huang, J. W. Lynn, R. W. Erwin, A. Santoro, D. C. Dender, V. N. Smalyaninova, K. Ghosh and R. L. Greene, *Phys. Rev.*, B 61, 8895, 2000.

99. M. Uehara, S. Mori, C. H. Chem and S. W. Cheong, *Nature*, 399, 560, 1999.

100. P. M. Woodward, D. E. Cox, T. Vogt, C. N. R. Rao and A. K. Cheetham, *Chem. Mater.* 11, 3528, 1999.

101. J. Q. Li, C. Dong, L. H. Lin and Y. M. Ni, *Phys. Rev.*, B 64, 174413, 2001.

102. J. S. Zhou, J. B. Goodenough and J. F. Mitchell, *Phys. Rev.*, B 61, R9217, 2000.

# 2. SCOPE OF THE PRESENT INVESTIGATIONS

The objectives of the various investigations carried out on rare earth manganates are presented in this section.

## 2.1 Cation-deficient lanthanum manganates, $Ln_{1-x}MnO_3$ and $LaMn_{1-x}O_3$ ($x$=0-0.1)

Magnetotransport properties of rare earth manganates of the type $Ln_{1-x}A_xMnO_3$ (Ln = rare earth, A = alkaline earth) have been investigated widely in the last few years because of the fascinating phenomena of colossal magnetoresistance (CMR) and charge ordering (CO) [1]. In these materials Mn is present in 3+ and 4+ states giving rise to ferromagnetism and insulator to metal (IM) transition around the Curie temperature, $T_c$, because of the Zener mechanism of electron hopping.

It has been shown that mixed valency of Mn in $LaMnO_3$ can be achieved by cation deficiency in A or B sites [2,3]. Thus, $La_{0.9}MnO_3$ composition with 30% $Mn^{3+}$ shows ferromagnetism similar to $La_{0.7}Ca_{0.3}MnO_3$ ($T_c$ ~ 250 K) and the IM transition around $T_c$, besides good CMR. The non-stoichiometric compounds undergo a structural change from orthorhombic, when $x < 0.04$ to a rhombohedral structure when $x > 0.04$. The deficiency varies the bond angle and hence the transport properties.

The magnetic and electronic transport measurements on $La_{1-x}MnO_3$ and $LaMn_{1-x}O_3$ are reported for polycrystalline samples. These samples show reasonably good CMR [3,4]. Surprisingly, no CMR has been found in $La_{0.93}MnO_3$ by de Brion et al [5]. Electrical resistivity of some of the polycrystalline $La_{1-x}MnO_3$ samples are also

reported to exhibit double peaks around IM transition, possibly due to the presence of similar defect phases. Single crystals of cation-deficient $LaMnO_3$ with a nominal composition of $La_{0.936}Mn_{0.982}O_3$ have been grown by fused-salt electrolysis. The crystals show a $T_c$ of 250 K with a magnetoresistance (MR) of ~ 55% at 255 K [6]. In view of the present scenario, it was our interest to grow good crystals of cation deficient $La_{1-x}MnO_3$ and $LaMn_{1-x}O_3$ by the floating zone melting technique, which has been employed widely to grow crystals of $Ln_{1-x}A_xMnO_3$, in order to understand the effect of cation deficiency on the magnetotransport properties. Hence, we chose $La_{1-x}MnO_3$ ($x$ = 0.04 and 0.1) and $LaMn_{1-x}O_3$ ($x$ = 0.1) and also stoichiometric $LaMnO_3$ for this purpose. This systematic study was necessary as there were discrepancy in the CMR values which varied from 50-77%.

## 2.2 Electric-current induced effects on rare earth manganates

Control of phases in the manganates of the type $Ln_{1-x}A_xMnO_3$ can be achieved by suitably choosing appropriate Ln and A cations to control the bandwidth as well as bandfilling. Thus, certain A-site cations lead to wide bandwidth conductors exhibiting ferromagnetism and metallicity through the double exchange mechanism. By reducing the bandwidth and increasing the coulombic repulsion, charge ordering can be induced. Charge ordering is also favored by ordering of orbitals coupled to Jahn-Teller distortion.

Since, the electronic properties are dependent on phases the tunability of properties depends upon the extent of control on the phases. Apart from substitutions at the A and B sites, electronic properties in these manganates have been modified by subjecting them to external stimuli such as magnetic fields [7], and irradiation by

application of high power lasers [8,9]. Such external stimuli can transform the CO state to a ferromagnetic metallic (FMM) state.

Electric fields are also expected to transform CO state to the FMM state, the conductive nature of the latter arising from the tunnel junctions separating neighboring ferromagnetic domains or due to the percolative nature of the conductive state. Current-induced memory effects and switching behavior have been observed in both thin films and bulk samples of manganates [10,11]. Interestingly, relatively small currents are found to cause a small decrease in the resistivity of thin films of $La_{0.7}Sr_{0.3}MnO_3$ [12]. Current-induced metastable resistive states occur in $La_{0.82}Ca_{0.18}MnO_3$ wherein the current-induced low resistive state exhibits memory effects [13]. We were interested to explore electric-field effects on rare earth manganate compositions which exhibit CMR in order to find out whether we can observe colossal electroresistance and any other effects induced by electric fields in these manganates. For this purpose, we have studied current-induced effects on crystals of $La_{0.77}Ca_{0.23}MnO_3$ and $La_{0.9}MnO_3$ which exhibit insulator-metal (IM) transitions near the ferromagnetic Curie temperatures.

We were interested to study whether electrical fields affect the CO transition, and whether the nature of the insulator-metal transition depends on the average size of the A-site cations. For this purpose, we have chosen $Nd_{0.5}Ca_{0.5}MnO_3$ and $Pr_{0.6}Ca_{0.4}MnO_3$, wherein the former with an average radius of the A-site cation, $<r_A>$ of 1.172 Å shows robust CO state with a transition temperature $T_{co}$ of 240 K which cannot be melted even under high magnetic fields of 25 T or greater. On the other hand, $Pr_{0.6}Ca_{0.4}MnO_3$ ($<r_A>$ = 1.18 Å) shows charge ordering around 230 K, and the CO state transforms to a FMM

state at fields of 6-12 T. A comparison of the electric field effects on these two manganates is of interest, specially since it is known that electric field-induced insulator-metal transition is accompanied by the appearance of magnetization.

### 2.3 Grain size effects on the ferromagnetism, charge ordering and phase separation in $Nd_{0.5}Sr_{0.5}MnO_3$ and $Nd_{0.5}Ca_{0.5}MnO_3$

The effect of particle size on the colossal magnetoresistance and related properties of $La_{0.7}Ca_{0.3}MnO_3$ has been reported in the literature [14]. The manganates with different particle sizes were prepared by sintering the material obtained by sol-gel synthesis at different temperatures. With increasing temperature of sintering the size of the particle increases. A study of such samples has shown that the grain size (particle size) affects the insulator-metal transition and the value of magnetization, although $T_c$ remains unaffected. In $La_{0.67}Ca_{0.33}MnO_3$ [15], the magnetization and the $T_c$ increase with the temperature of sintering. An exactly opposite trend was reported for $La_{0.85}Sr_{0.15}MnO_3$ [16]. These studies underline the role played by grain size on the magnetotransport properties of the rare earth manganates. It has been shown in the literature, through neutron and X-ray diffraction studies, that $Nd_{0.5}Sr_{0.5}MnO_3$ separates into three macroscopically different phases at low temperatures. The phases involved are high temperature ferromagnetic metallic phase, orbitally ordered A-type antiferromagnetic phase and the charge-ordered CE-type antiferromagnetic phase [17]. The effects of grain size in phase separation of this manganate have not been studied.

An aspect that we need to understand is the effect of particle size on the phase separation in the rare earth manganates. Phase separation can involve coexisting FM,

AFM and CO phases; the fraction of each phase being dependent on the concentration of the dopant and the temperature. Usually phase separation involves the formation of droplets of one phase in a matrix of another. It has been suggested that phase separation can be controlled by external factors such as magnetic fields, electric fields and pressure. Therefore, we considered it worthwhile to examine the grain size effect on the magnetotransport and phase separation in manganates exhibiting ferromagnetism, charge ordering and antiferromagnetism.

It was considered important to examine the effect of grain size on two typical charge-ordered manganates which show phase separation. We have chosen $Nd_{0.5}Sr_{0.5}MnO_3$ and $Nd_{0.5}Ca_{0.5}MnO_3$ for this purpose. The latter manganate shows charge ordering at 240 K and becomes AFM around 140 K [18] while the former which becomes ferromagnetic around 250 K and then transforms into a charge ordered antiferromagnetic around 150 K [19]. The comparative study was expected to help to understand the effect of the grain size on phase separation and the associated magnetic and electric properties of these manganates.

### 2.4 Electron-doped rare earth manganates, $Ln_xCa_{1-x}MnO_3$ (Ln = La, Nd, Gd and Y; $x$ = 0.02- 0.25)

The electron-doped regime of rare earth manganates of the general formula $Ln_xCa_{1-x}MnO_3$ (Ln = rare earth, $x < 0.5$) have attracted considerable attention because of the unusual properties exhibited by the compositions in this regime [20,21]. The electron-doped manganates are different from the hole-doped manganates ($x > 0.5$) in several ways, and electron-hole asymmetry in the manganate system has been discussed in some

detail [21]. The electron-doped manganates are dominated by charge ordering and do not exhibit the ferromagnetic (FM) ground state at any composition. Even small doping in the A-site ($x \leq 0.03$) has marked effects on electronic properties of the manganates [22]. In the $Ln_xCa_{1-x}MnO_3$ system, compositions with $x < 0.03$ exhibit G-type antiferromagnetism while those with $x = 0.1$-$0.15$ shows C-type antiferromagnetism, often in admixture with G-type antiferromagnetism. Ferromagnetic clusters are present in the entire antiferromagnetic (AFM) regime [23]. Compositions in the $x = 0.03$-$0.1$ range show a significant increase in magnetization around 100 K due to the presence of FM clusters in the AFM matrix. There is also a change in the resistivity behavior around 100 K and the $x \leq 0.1$ compositions exhibit low electrical resistivity above this temperature [24,28]. Magnetic susceptibility and resistivity data show some history dependence or irreversibility as well [23]. Charge ordering appears to manifest itself when $x > 0.1$-$0.15$, but the manner of evolution of this phenomenon with change in temperature and composition has not been fully examined. It is generally believed that there is phase separation at low temperatures, with the size of the ferromagnetic domains increasing with the dopant concentration in the $x = 0.02$-$0.1$ composition range [23,28,29]. Electrical conduction in this regime could be percolative.

In spite of several studies on the $Ln_xCa_{1-x}MnO_3$ system reported in the literature, there are many aspects of these materials that we do not understand fully. Some important aspects of interest are the following: Is the ferromagnetic cluster or spin-glass regime ($x < 0.1$-$0.15$) where the magnetization increases with $x$ or electron concentration, sensitive to the average A-site cation radius, $\langle r_A \rangle$? Is there a metallic behavior at

temperatures beyond the spin-glass regime? In what way is the phase separation dependent on the composition and $<r_A>$? Is the conduction percolative at low temperatures for $x < 0.1$-$0.15$, and if so, is it affected by the A-site cation radius? When exactly does charge ordering manifest itself and what is the effect of the A-site cation radius on the charge-ordering transition? In order to contribute to the understanding of some of these questions, we have carried out systematic resistivity and magnetization measurements on $Ln_xCa_{1-x}MnO_3$ (Ln = La, Nd, Gd and Y) with $x$ varying between 0.02 and 0.25, making sure that there are sufficient compositions in the $x < 0.1$ and $x > 0.1$ regimes. The latter regime is relevant to examine the emergence of charge ordering effects. Although measurements on some of these manganate compositions have been reported in the literature, it was our considered view that careful measurements were necessary on a related series of manganates, covering a range of compositions from the pure G-AFM regime at very low $x$ to the charge-ordered regime at $x = 0.1$-$0.25$, in order to fully understand the electron doped regime. The present study throws light on the various phenomena such as phase separation, charge ordering and percolative conduction occurring in the $x = 0.02$-$0.25$ range of the electron-doped rare earth manganates and helps to adequately describe the characteristics of this fascinating regime.

## 2.5 Electron-doped rare earth manganates of Ruddelsden-Popper $CaO(Pr_{0.08}Ca_{0.92}MnO_3)_n$ ($n$ = 1,2,3 and ∞) series

In the low-doping regime of the $Ln_{1-x}A_xMnO_3$ ($x > 0.08$), i.e., when small amounts of rare earth ions are substituted for Ca in $CaMnO_3$, the manganates show a variety of electronic and magnetic properties. For $Mn^{3+}$ concentrations less than 10%, there exists a

ferromagnetic-like transition around 100 K with no associated I-M transition in the resistivity. Nevertheless, the resistivity is small. In addition, the electrical conductivity scales with the concentration of dopant ions implying that the conduction is mainly percolative in nature. Further, when $x > 0.1$ ($Mn^{3+}$ concentration greater than 10%) there is CO and an associated AFM. The critical value of $x$ for which the CO is seen varies with the radius of the rare-earth cation. Interestingly, these materials also show unusually large thermopower [23, 30].

Doping of tetravalent Th or Ce into the Ca-Mn-O systems introduces two electrons resulting in $Mn^{2+}$ and $Mn^{4+}$ ions. The properties are essentially similar to those of one electron-doped systems such as $La_{1-x}Ca_xMnO_3$; however, the doping concentrations required for the observation of CO is nearly half that of the one electron-doped systems. In the two-electron-doped RP phases of the type $Th_{1-x}Ca_{2+x}Mn_2O_7$, weak ferromagnetism and negative magnetoresistance (MR) have been observed [31]. The origin of negative MR observed in this series has been explained based on a tunneling model. Interestingly, systems such as $Ln_{0.7}Ce_{0.3}MnO_3$, where doping with a tetravalent Ce ion is believed to facilitate the formation of $Mn^{2+}$ ions, exhibit ferromagnetism and associated I-M transition [31-34]. This is in contrast to the electron-doped calcium manganates where I-M transition is absent although ferromagnetic-like behavior can be obtained at critical doping concentrations.

Electron-doped La-Ca-Mn-O Ruddlesden-Popper (RP) phases with the composition $La_{2-2x}Ca_{1+2x}Mn_2O_7$ exhibit ferromagnetism and I-M transition for $x \sim 0.25$ [35]. The crossover region between $x = 0.8$ to 0.85 compositions show unusual magnetic

behavior [36]. The magnetic properties show a crossover behavior from canted antiferromagnetic (CAF) structure around $x = 0.85$ to a stable CO state for $x < 0.8$. The literature on electron-doped RP manganates is not extensive, and in particular, the available data are insufficient to point to a universal behavior in this regime.

Therefore, it was our interest to examine the electronic and magnetic properties of single electron-doped systems in RP series. In order to study the variation in electronic and magnetic properties of the RP phases, we chose the compositions $CaO(Pr_{0.08}Ca_{0.92}MnO_3)_n$ ($n$ = 1,2,3 and ∞) for several reasons. The choice of $Pr^{3+}$ is due to size compatibility with $Ca^{2+}$ in ninefold coordination environment (ionic radius of $Pr^{3+}$ = ionic radius of $Ca^{2+}$ = 132 pm). This allowed us to compare the electronic properties of the doped and undoped systems without having to consider the changes in the unit-cell volume. The value for $x$ was fixed at 0.92 based on the literature available for the three-dimensional perovskite ($n = \infty$) to observe both ferromagnetism and high conductivity at low temperatures. Previously, it has been shown that both the conductivity and magnetization in the RP series $CaO(CaMnO_3)_n$ scales with the number of perovskite layers between the rock-salt CaO layers [37]. In this study, we report for the first time the structure and electronic properties of electron-doped RP series in the Ca-Mn-O system.

## 2.6 Electronic phase separation in $(La_{1-x}Ln_x)_{0.7}Ca_{0.3}MnO_3$ (Ln = Nd, Gd and Y)

Rare earth manganates of the general formula $Ln_{1-x}A_xMnO_3$ (Ln = rare earth, A = alkaline earth) exhibit many interesting properties such as colossal magnetoresistance, charge ordering and electronic phase separation [1,38]. Phase separation in these materials has

attracted much interest in the last few years because of the fascinating features associated with the phenomenon [38]. Of the various manganite compositions, the $(La_{1-x}Pr_x)_{0.7}Ca_{0.3}MnO_3$ system has provided really valuable information on the electronic phase separation [39-41]. This is a convenient system for the study of phase separation since the Pr-rich compositions are antiferromagnetic (AFM) and charge ordered (CO) whereas the La-rich compositions are ferromagnetic metals (FMM). At a fixed Ca mole fraction of 0.3, a change in $x$ leads to a transition from FMM behavior to a charge ordered insulator (COI) behavior around a $x$ value of 0.7. That phase separation in $(La_{1-x}Pr_x)_{0.7}Ca_{0.3}MnO_3$ involves the FMM and COI domains, has been demonstrated by various types of measurements. This system exhibits several unusual features. Thus, in spite of the drop in resistivity at the insulator-metal (IM) transition, the CO peaks in the X-ray diffraction pattern continue to grow at low temperatures [42]. Besides the COI phase, another phase is suggested to be present below the charge ordering temperature [42]. Based on a neutron diffraction study, a phase diagram has been provided for this system wherein the $0.6 \leq x \leq 0.8$ region separates the homogeneous FMM and AFM phases [43].

Noting that the phase separation in $(La_{1-x}Pr_x)_{0.7}Ca_{0.3}MnO_3$ is triggered by A-site cation disorder, we considered it important to investigate a series of compounds of the type $(La_{1-x}Ln_x)_{0.7}Ca_{0.3}MnO_3$ over a range of compositions ($0 \leq x < 1$) where the variation in Ln brings about a marked change in the average A-site cation radius, $< r_A >$, as well as the size disorder. Here, we report the results of a systematic study of the electronic, magnetic and dielectric properties of three series of $(La_{1-x}Ln_x)_{0.7}Ca_{0.3}MnO_3$ with Ln = Nd,

Gd and Y. It is to be noted that in all the compositions of the three series of manganates, the $Mn^{4+}/Mn^{3+}$ ratio remains constant, the only variable being the average A-site cation radius and the associated disorder.

## 2.7 References


1. C. N. R. Rao, B. Raveau *Colossal magneto resistance, charge-ordering and related properties of rare earth manganese oxides*, (Eds.), World Scientific, Singapore, 1998.
2. C. N. R. Rao and A. K. Cheetham, *Science*, 272, 369, 1996.
3. A. Arulraj, R.Mahesh, G. N. Subbanna, R. Mahendiran, A. K. Raychaudhuri, C. N. R. Rao. *J. Solid.State. Chem.*, 127, 87, 1996.
4. J. Topfer, J. B. Goodenough, *Chem. Mater.*, 9, 1467, 1997.
5. S. de Brion, F. Ciorcas, G. Chouteau, P. Lejay, P. Radelli, C. Chaillout, *Phys. Rev.*, B 59, 1304, 1999
6. W. H. McCarroll, K. V. Ramanujachary, M. Greenblatt, F. Cosandey, *J. Solid. State. Chem.*, 36, 322, 1998.
7. Y. Tomioka, A. Asamitsu, H. Kuwahara, Y. Moritomo and Y. Tokura, *Phys. Rev.*, B 53, 1689, 1996.
8. K. Miyano, T. Tanaka, Y. Tomioka and Y. Tokura, *Phys. Rev. Lett.*, 78, 4257, 1997.
9. M. Fiebig, K. Miyano, Y. Tomioka and Y. Tokura, *Science*, 280, 1925, 1998.
10. C. N. R. Rao, A.R. Raju, V. Ponnambalam, S. Parashar and N. Kumar, *Phys. Rev.*, B 61, 594, 2000.
11. V. Ponnambalam, S. Parashar, A. R. Raju and C. N. R. Rao, *Appl. Phys. Lett.*, 74, 206, 1999.
12. A. K. Debnath and J. G. Jin, *Phys. Rev.*, B 67, 064412, 2003.
13. Y. Yuzhelevski, V. Markovich, V. Dikovsky, E. Rozeberg, G. Gordetsky, G. Jung, D. A. Shulyatev and Ya. M. Mukavskii, *Phys. Rev.*, B 64, 224428, 2001

14. R. Mahesh, R. Mahendiran, A.K. Raychaudhuri and C.N.R. Rao, *Appl. Phys. Lett.*, 68, 2291,1996.

15. R. D. Sanchez, J. Rivas, C. Vazquez-Vazquez, A. Lopex-Quintela, M. T. Causa, M. Tovar and S. Oseroff, *Appl. Phys. Lett.*, 68, 134, 1996.

16. N. Zang, W. Ding, W. Zhong, W. Yang and Y. Ku, *J. Phys. Condens. Matter.*, 9, 4279, 1997.

17. P. M. Woodward, D. E. Cox, T. Vogt, C. N. R. Rao and A. K. Cheetham, *Chem. Mater.*, 11, 3528, 1999.

18. T. Vogt, A. K. Cheetham, R. Mahendiran, A. K. Raychaudhuri, R. Mahesh and C. N. R. Rao, *Phys. Rev.*, B 54, 15303, 1996.

19. H. Kuwahara, Y. Tomioka, A. Asamitsu, Y. Moritomo and Y. Tokura, *Science*, 270, 961, 1995.

20. C. N. R. Rao, A. Arulraj, A. K. Cheetham and B. Raveau, *J. Phys.: Condens. Matter.*, 12, R 83, 2000.

21. K. Vijaya Sarathy, P. V. Vanitha, R. Seshadri, A. K. Cheetham and C. N. R. Rao, *Chem. Mater.*, 13, 787, 2001.

22. E.Granado, N. O. Moreno, H. Martinho, A. Garcia, J. A. Sanjurjo, I. Torriani, C. Rettori, J. J. Neumeier and S. B. Oseroff, *Phys. Rev. Letts.*, 86, 5385, 2001.

23. J. J. Neumeier and J. L. Cohn, *Phys. Rev.*, B 61, 14319, 2000.

24. R. Mahendiran, A. Maignan, C. Martin, M. Hervieu and B. Raveau, *Phys. Rev.*, B 62, 11644, 2000.

25. A. Maignan, C. Martin, F. Damay, and B. Raveau, *Chem. Mater.*, 10, 950, 1998.

26. A. Maignan, C. Martin, F. Damay, B. Raveau and J. Hejtmanek, *Phys. Rev.*, B 58, 2758, 1998.

27. J. Hejtmanek, Z. Jirak, M. Marysko, C. Martin, A. Maignan, M.Hervieu, and B. Raveau, *Phys. Rev.*, B 60, 14057, 1999.

28. C. Martin, A. Maignan, M. Hervieu, B. Raveau, Z. Jirak, M. M. Savosta, A. Kurbakov, V. Trounov, G. Andre and F. Bouree, *Phys. Rev.*, B 62, 6442, 2000; M. Respaud, J.M. Broto, H. Rakoto, J. Vanacken, P. Wagner, C. Martin, A. Maignan and B. Raveau, *Phys. Rev.*, B 63, 144426, 2001.

29. L. M Rodriguez-Martinez and J. P. Attfield, *Phys. Rev.*, B 54, R15622, 1996.

30. A. Maignan, C. Martin, C. Autret, M. Hervieu, B. Raveau and J. Hejtmanek, *J. Mater. Chem.*, 12, 1806, 2002.

31. M. V. Lobanov, S. Li and M. Greenblatt, in press.

32. J. R. Gebhardt, S. Roy and N. Ali, *J. Appl. Phys.*, 85, 5390, 1999.

33. P. Mandal and S. Das, *Phys. Rev.*, B 56, 15073, 1997.

34. P. Raychaudhuri, S. Mukherjee, A. K. Nigam, J. John, U. D. Vaisnav, R. Pinto and P. Mandal, *J. Appl. Phys.*, 86, 5718, 1999.

35. I. D. Fawcett, E. Kim, M. Greenblatt, M. Croft and L. A. Bendersky, *Phys. Rev.*, B 62, 6485, 2000.

36. H. Asano, J. Hayakawa and M. Matsui, *Appl. Phys. Lett.*, 68, 3638, 1996.

37. I. D. Fawcett, J. E. Sunstrom IV, M. Croft, K. V. Ramanujachary and M. Greenblatt, *Chem. Mater.*, 10, 3643, 1998.

38. C. N. R. Rao and P. V. Vanitha, *Curr. Opp. Solid State Mater. Sci.*, 6, 97, 2002.

39. M. Uehara, S. Mori, C.H. Chen and S.-W. Cheong, *Nature*, 399, 560, 1999.

40. N. A. Babushkina, A. N. Taldenkov, L. M. Belova, E. A. Chistotina, O. Yu. Gorbenko, A. R. Kaul, K. I. Kugel and D. I. Khomskii, *Phys. Rev.*, B 62, R6081, 2000.

41. H. J. Lee, K. H. Kim, M. W. Kim, T. W. Noh, B. G.Kim, T. Y. Koo, S. W. Cheong, Y. J. Wang and X. Wei, *Phys. Rev.*, B 65, 115118, 2002.

42. V. Kiryukhin, B. G. Kim, V.Podzorov, S. W. Cheong, T. Y. Koo, J. P. Hill, I. Moon and Y. H. Jeong, *Phys. Rev.*, B 63, 024420, 2000.

43. A.. M. Balagurov, Y. Yu. Pomjakushin, D. V. Sheptyakov, V.L. Aksenov, P. Fischer, L. Keller, O. Yu. Gorbenko, A. R. Kaul and N. A. Babushkina, *Phys. Rev.*, B 64, 024420, 2001.

# 3. EXPERIMENTAL

## 3.1 Synthesis

### 3.1.1 Polycrystalline materials

#### *a. Solid-state synthesis*

Polycrystalline compounds were prepared by the standard solid-state synthesis technique. The method depends upon a solid-state interdiffusion between the oxide powders and therefore it becomes necessary to use a fine, well-compacted powder. The sintering temperature for the synthesis was kept high for the diffusion length 'd' to exceed the particle size. The diffusion length 'd' is given by $(2Dt)^{1/2}$, where 'D' is the diffusion constant for the fast-diffusing species and 't' is the firing time.

Rare-earth manganates were prepared by starting with a stoichiometric mixture of the rare earth oxide with an alkaline earth carbonate and manganese oxide, thoroughly mixed in a agate mortar with the help of iso-propyl alcohol. After grinding the initial compounds homogeneously, the mixture was transferred to an alumina/platinum crucible and preheated to 1273-1373 K for 24 h with repeated intermediate grindings. The preheated sample was further fired at 1473 K for 12-24 h in a platinum crucible. The heated sample was then ground thoroughly and pelletized under a constant pressure of 40-50 $kgcm^{-2}$ in a steel pelletizing dye. The pellets were then transferred into a platinum boat which is fired at 1500-1673 K for 12 to 72 h. The sample was cooled at desired rates (10 °C $min^{-1}$ to 0.1°C $min^{-1}$) depending upon the oxygen sensitivity of the sample.

Since, one of the prerequisites for obtaining homogeneous composition is the diffusion length, a precursor that decomposes into an ultrafine-grain oxide on

preheating, yielding a highly reactive powder is preferred. Hence, at least one of the reactant precursors is chosen as carbonate or acetate.

### Synthesis of $Ln_xCa_{1-x}MnO_3$ (Ln = La, Nd, Gd and Y)

Polycrystalline powders of $Ln_xCa_{1-x}MnO_3$ (Ln = La, Nd,Gd and Y) compositions were prepared by the solid-state reaction of stoichiometric amounts of the rare earth acetate with $CaCO_3$ and $MnO_2$. The starting materials were ground and heated to 1273 K for 60 h with 3 intermediate grindings. Then the samples were reheated at 1473 K for 48 hrs with 2 intermediate grindings. The samples were then pelletized and heated to 1600 K for 36 h followed by cooling at 5°C $min^{-1}$.

### Preparation of $(La_{1-x}Ln_x)_{0.7}Ca_{0.3}MnO_3$ (Ln = Nd, Gd and Y)

Compositions of the formula $(La_{1-x}Ln_x)_{0.7}Ca_{0.3}MnO_3$ (Ln = Nd, Gd or Y) were prepared by standard solid-state synthesis. A stoichiometric mixture of the rare earth acetate, $CaCO_3$ and $MnO_2$ were mixed thoroughly in an agate mortar with the help of iso-propyl alcohol, and the mixture was first fired to 1273 K for 48 h with two intermediate grindings. This preheated sample was then further heated at 1473 K for 24 h, pressed into pellets and fired to 1648 K for 12 h to obtain the single-phase compounds.

### *b. Sol-gel synthesis*

Sol-gel synthesis is a wet chemical method and the multi-step process involves both chemical and physical processes such as hydrolysis, polymerization, drying and densification. A distinctive viscosity increase indicates the onset of gel formation. There are six important steps in the formation of a final compound [1,2].

1) Hydrolysis: The hydrolysis starts with a mixture of a metal hydroxide and water in a solvent (water/alcohol) at the ambient or at a slightly elevated temperature. Acid catalysts are added to speed up the reaction.
2) Polymerization: This step involves the condensation of adjacent molecules wherein water and alcohol molecules are eliminated and metal oxide linkages are formed. Polymeric networks grow to colloidal dimensions in the liquid state.
3) Gelation: In this step, the polymeric networks link up to form a three-dimensional network throughout the liquid. The gelation process involves removal of water or alcohol molecules, which remain inside the pores of the gel.
4) Drying: Here, water molecules are removed at moderate temperatures (373-425 K) leading to a hydroxylated metal oxide with residual organic content.
5) Dehydration: By heating the dried samples to temperatures between 625-925 K, the organic as well as chemically bound water molecules are removed. The resultant compound is ultrafine and has very high surface area.
6) Densification: Temperatures in excess of 1273 K are used to form the dense oxide product.

A schematic for preparing rare earth manganates ($Ln_{1-x}A_xMnO_3$) through sol-gel technique is shown in Fig 3.1.

### Sol-gel synthesis of $Nd_{0.5}A_{0.5}MnO_3$ (A = Ca or Sr)

A mixture of $Nd(NO_3)_3$, $Sr/Ca(NO_3)_2$ and $Mn(CH_3COO)_2$ in the required molar proportion was dissolved in water and an aqueous solution of citric acid (CA) added to it keeping the CA/metal ion ratio at 1.3 to 1.0 depending on whether it had Ca or

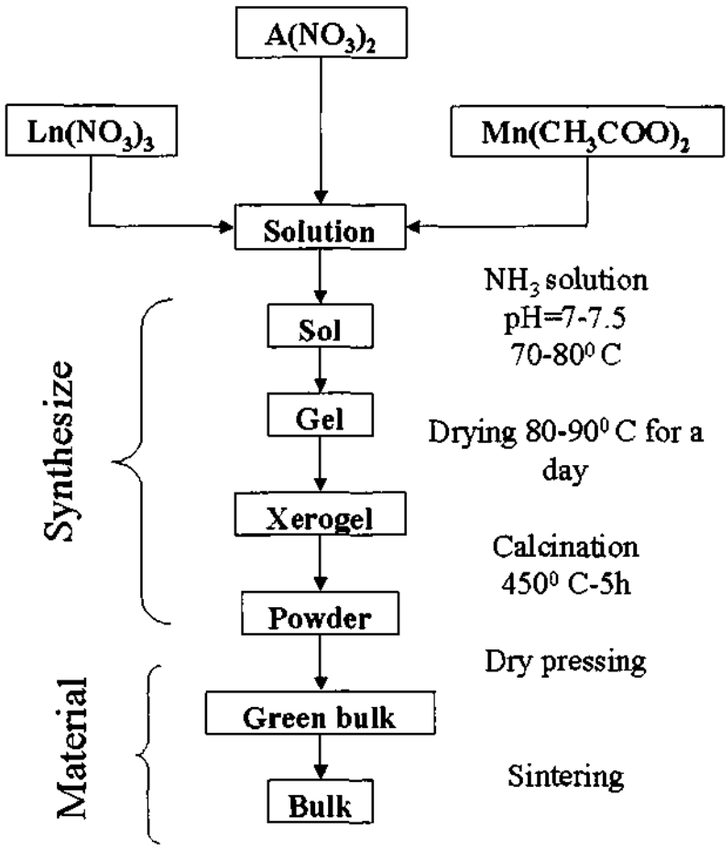


*Fig. 3.1 Schematic of the various steps involved in sol-gel synthesis.*

Sr nitrate. The solution was vigorously stirred and the pH of the solution adjusted to 7-7.5 by adding the ammonia solution. On vigorously stirring the solution at 350 K, a homogeneous transparent gel was obtained. The gel was dried in air for a day, to convert it to a xerogel.

The xerogel was first sintered to 723 K before subjecting it to sintering at different temperatures. Thus, each sample was sintered for 3 h at 1173 K, 1273 K, 1373 K, 1473 K, 1573 K and 1673 K. In another set of experiments, the temperature was kept constant at 1573 K and the period of sintering varied from 3 h to 12 h. The $Mn^{4+}$ content was estimated by volumetric redox titrations using a

$KMnO_4$ standard. The percentage of $Mn^{4+}$ was found to be around 48 (±4) independent of the temperature of sintering in both $Nd_{0.5}Ca_{0.5}MnO_3$ and $Nd_{0.5}Sr_{0.5}MnO_3$.

**Ruddlesden-Popper phases, $CaO(Pr_{0.08}Ca_{0.92}MnO_3)_n$ (n=1,2,3 and ∞)**

The materials reported were prepared by standard sol-gel method in which stoichiometric amounts of Pr acetate, Mn acetate and $Ca(NO_3)_2$ were dissolved thoroughly in distilled water resulting in a transparent solution. To this solution citric acid was added in 1:1 molar ratio. The solution was then gently heated with constant stirring over a hot plate until all the water evaporated and a translucent gel was left behind. This gel was further heated in a furnace at 723 K for 10-12 h in air to remove the carbonaceous components. This carbon-free material was further heated at 1273 K for 12 h to improve the sample homogeneity and phase formation. Finally the powders were compacted and sintered at 1473 K for 24 hours. All measurements reported here are carried out on the sintered specimens. Magnetization and ac susceptibility were performed with a Quantum Design Physical Property Measurement System (PPMS) from 350 to 5 K at applied magnetic fields up to 90 kOe.

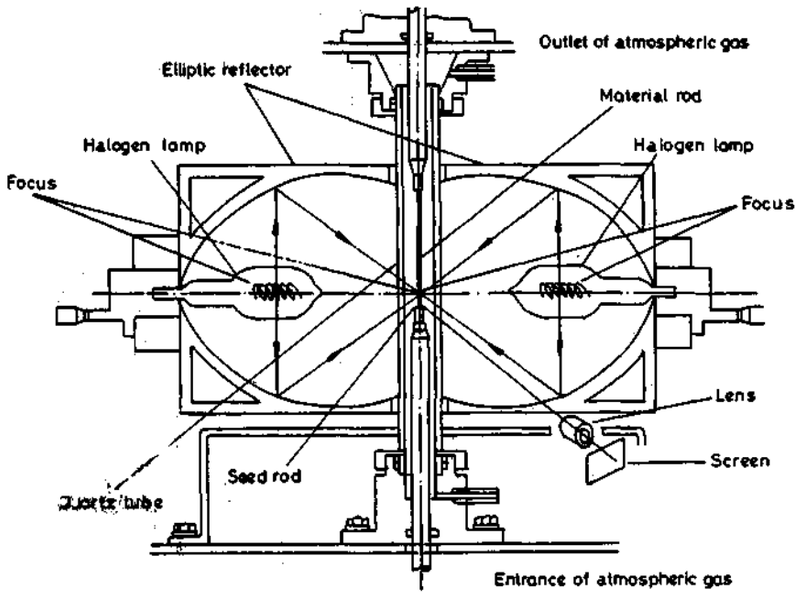


*Fig. 3.2 Schematic of the cross sectional view of the image furnace*

### 3.1.2 Crystal growth by floating zone melting technique

Preparation of high quality single crystals involves elimination of impurities. Hence, problems associated with the crucible techniques can be overcome by a floating zone technique, wherein the materials in the form of a freestanding rods are clamped by their ends. In this technique relatively small zones are melted by a suitable heating equipment (eg: irradiation by infra red rays). The melt is stabilized between the two rods giving it the name floating zone technique. The single crystal seed can be generated by spontaneous nucleation. This technique is widely used for dielectric substances [3,4]. The radiation coming from optical or thermal source is focussed on to a spot where the top and the bottom rods meet. The focussing is achieved by means of concave ellipsoidal mirrors.

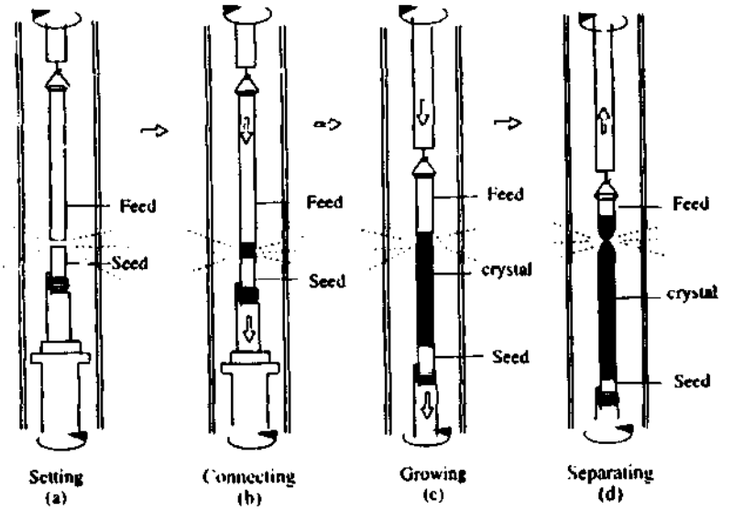


*Fig. 3.3 Schematic of the various stages in the growth of the crystal in an image furnace*

The main components of the floating zone melting technique are

1) Halogen lamps, which controls the heating.
2) Ellipsoidal mirrors, which focuses the light on to a narrow spot.
3) Quartz tube encloses the floating zone and provides a casing for passing different gases.
4) Two different pulleys that can be moved independently at very slow rate thus controlling the growth rates (Fig. 3.3).

The floating zone image furnace (SC-M35HD from Nichiden Machinery Ltd., Japan) consisting of two halogen lamps can reach maximum temperature of 2425 K. The quartz tube enables the use of different atmospheres at pressures up to 6 atm. In this technique, high purity stoichiometric compositions are prepared by standard solid-state route. High-density rods which are necessary for crystal growth are obtained by hydraulic pressing and subsequent sintering at high temperature.

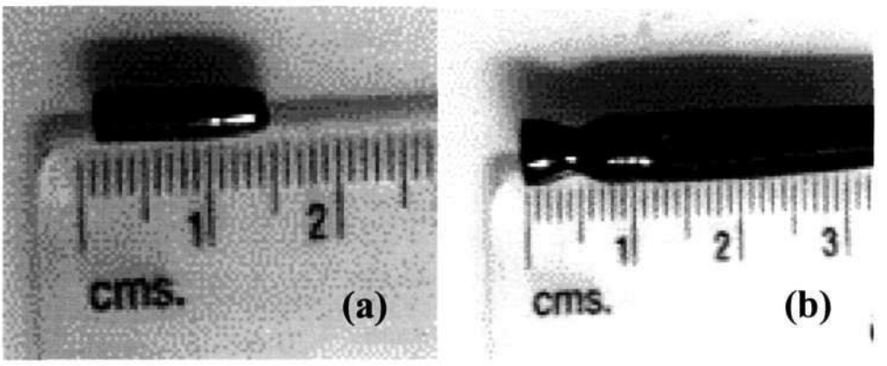


***Fig. 3.4*** *Single crystals of cation deficient $LaMnO_3$ crystal grown from floating zone melting technique.* ***(a)*** *$La_{0.9}MnO_3$.* ***(b)*** *$LaMn_{0.9}O_3$.*

These high-density rods are used as feed and seed in the floating zone melting technique. The pulleys over which the sample rods are clamped can be rotated independently at a maximum speed of 50 rpm. The growth rates can range from 0.1 mm/h to 99 mm/h. The stability of the molten zone is achieved by changing temperature, rotation speed and the pulling rate of the melt (Fig. 3.3). The growth direction can be upward or downward, but a downward direction is preferred as the molten volume is more stable in this configuration.

### Cation-deficient lanthanum manganates, $Ln_{1-x}MnO_3$ and $LaMn_{1-x}O_3$ ($x$=0-0.1)

All the polycrystalline powders used for the growth of single crystals were prepared by the solid-state reaction of stoichiometric amounts of $La_2O_3$ and $MnO_2$ (99.99% pure) fired in air at 950 $^0$C prior to use. These powders were mixed thoroughly and heated to 1473 K for 24 h. The samples were then ground and reheated at the same temperature for 24 hours. The feed and seed rods for growing the single crystals were prepared using these polycrystalline powders which were filled in a latex tube and pressed using a hydraulic press at a pressure of 5 tonnes. The rods thus obtained

were sintered at 1673 K for 24 h. and single crystals of $La_{1-x}MnO_3$ ($x$ = 0.0, 0.04 and 0.1) and $LaMn_{0.9}O_3$ were grown by the floating zone melting technique by employing SC-M35HD double reflector infrared image furnace (Nichiden Machinery Ltd., Japan). The growth rate rotation speed employed in all the experiments was 10 mm/h and 30 rpm respectively. The $LaMnO_3$ crystals were grown in a nitrogen atmosphere $La_{0.96}MnO_3$ and $La_{0.9}MnO_3$ crystals were grown in air where as the crystal of $LaMn_{0.9}O_3$ was grown in an oxygen atmosphere. The flow rate was maintained as 3 L/min for all the experiments. The diameter of the grown crystals was 6 mm and the length varies between 20 mm and 60 mm Fig. 3.4.

### $Nd_{0.5}Ca_{0.5}MnO_3$ and $Pr_{0.6}Ca_{0.4}MnO_3$ crystals

Single crystals of $Nd_{0.5}Ca_{0.5}MnO_3$ and $Pr_{0.6}Ca_{0.4}MnO_3$ were grown by the floating zone melting furnace fitted with two ellipsoid halogen lamps, having prepared the polycrystalline samples of the materials by the solid state route. Monophasic polycrystalline samples were hydrostatically pressed and sintered at 1673 K for 24 hrs to obtain feed and seed rods of dimensions 8 cm in length and 4 mm in diameter. Single crystals were then grown under 2-3 L/min of airflow. The crystals thus obtained was cut and subjected to oxygen annealing for 48h (Fig. 3.5a).

### $La_{0.77}Ca_{0.23}MnO_3$

Single crystals of $La_{0.77}Ca_{0.23}MnO_3$ were grown by the floating zone melting furnace fitted with two ellipsoid halogen lamps, having prepared the polycrystalline samples of the materials by the solid state route. Monophasic polycrystalline

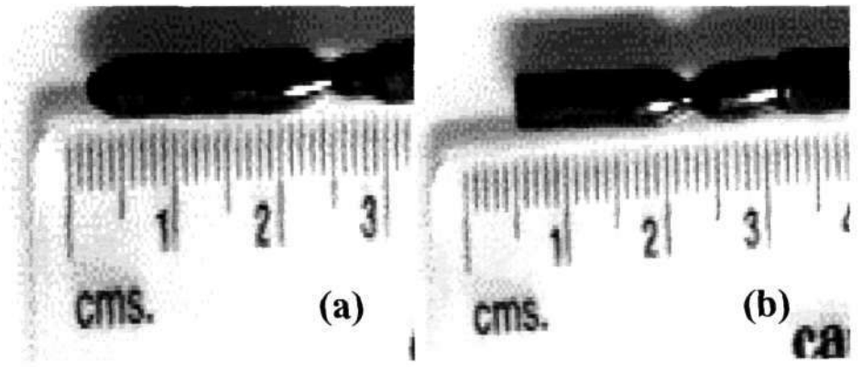


***Fig. 3.5*** *Single crystals of $Ln_{1-x}A_xMnO_3$ (Ln=rare earth; A=alkaline earth) grown by floating zone melting technique* ***(a)*** *$Pr_{0.6}Ca_{0.4}MnO_3$.* ***(b)*** *$La_{0.77}Ca_{0.23}MnO_3$*

samples were hydrostatically pressed and sintered at 1673 K for 24 hrs to obtain feed and seed rods of dimensions 8 cm in length and 4 mm in diameter. The $La_{0.77}Ca_{0.23}MnO_3$ crystals were grown in air at rate of 10 mm/h. The crystals thus obtained were cut and subjected to oxygen annealing for 48h (Fig. 3.5b). The $La_{0.77}Ca_{0.23}MnO_3$ showed ferromagnetic Curie temperatures, $T_c$ of 230 K. Electrical resistivity measurements were carried out on crystals of 4-6 mm diameter and 1 mm thickness by the standard four-probe method.

## 3.2 Methods of characterization

### 3.2.1 X-ray diffraction

X-ray diffraction measurements were carried out using Seifert 3000 (θ-θ scan) in Bragg-Brentano geometry. The data was collected from 5-40° at a scan rate of 0.01° $min^{-1}$. The power of the incident radiation (CuKα- 1.5406 Å) was adjusted by varying the input voltage and current. The X-ray counts were varied by the slit width of the detector and the X-ray source. The X-ray pattern thus obtained was fitted to relevant unit cell contents using PROZKI and CELREF packages.

### 3.2.2 Scanning electron microscopy

The grain size of the manganates was analysed by employing Leica-440I scanning electron microscope. The homogeneity and the elemental analysis of the sample was obtained by EDAX (Energy Dispersive Analysis of X-rays) attached to the scanning electron microscope.

### 3.2.3 Magnetization

Magnetization measurements were carried out using a Lakeshore 7300 vibrating sample magnetometer. The samples were cut into small pieces weighing ~0.1 g and the measurements were carried out in a field of 100-8000 G over the 300-50 K temperature range. The magnetic hysteresis measurements were carried out at a specific temperature in a –9000 to 9000 G field sweep.

### 3.2.4 Electrical transport measurements

#### *a. DC conductivity*

The electrical transport measurements in the four-probe configuration was carried out in a cryostat which operated between 15-300 K. The sample was mounted on a copper plate, and the electrical contacts using copper wires were established on the samples by silver epoxy which also acted as electrodes (Fig. 3.6). Measurements were made in the constant current mode by passing the required current (500 nA-60 mA) through the outer leads using a Keithley 224 programmable current source instrument. The voltage drop was measured across the inner leads by a HP 34401A multimeter. The silicon diode fixed to the cryostat near the sample measured the temperature to an accuracy of 0.01 K with the help of a Lakeshore 330 temperature controller.

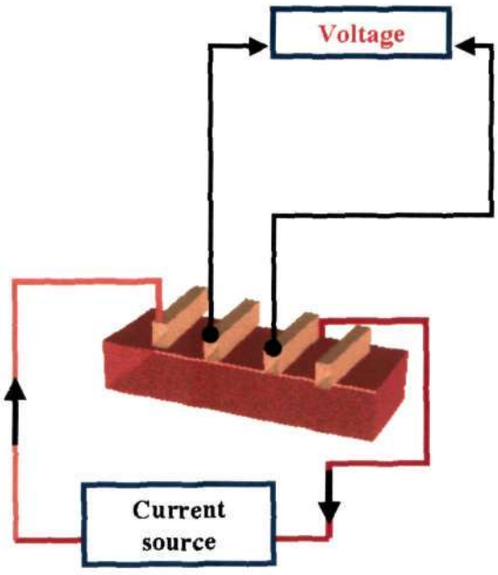


***Fig. 3.6*** *Schematic of the four-probe resistivity measurement.*

### *b. AC conductivity and dielectric measurements*

Frequency dependent dielectric measurements were carried out by dipping a closed quartz tube containing the sample in a dewar filled with liquid nitrogen (for low temperature measurement). The tube was evacuated and filled with ultra high pure helium in order to avoid any condensation on the sample. The sample preparation involved sputtering of gold on either side of the cylindrical shaped samples of dimensions (4-8 mm diameter and 1-4 mm in thickness) using silver epoxy and copper wires, leads were drawn out of the gold coated surface. The sample was cured at 373-423 K for 2-4 h. The dielectric properties were measured by Agilent 4294A meter in the 85-450 K temperature range.

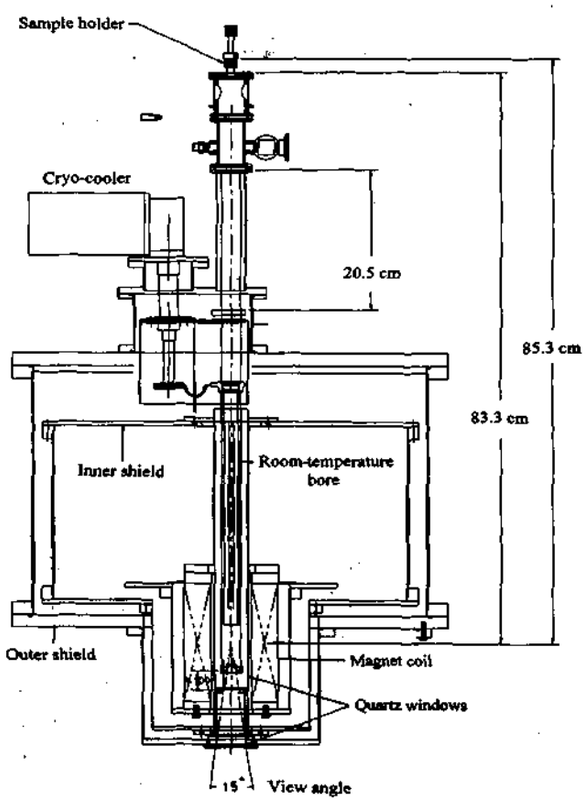


*Fig. 3.7 Schematic cross sectional view of the cryo magnet*

### c. Magnetoresistance

The magnetoresistance of the rare earth manganates of the form $Ln_{1-x}A_xMnO_3$ (Ln=rare earth; A=alkaline earth) was measured using a cryo-cooled superconducting magnet giving fields up to 15 tesla employing $Nb_3Sn$ wire, high $T_c$ $Bi_2Sr_2Ca_2Cu_3O_{10}$ (2223) leads and a close-cycle helium refrigerator of 1 W at 4.2 K. The preparation of the sample is similar to four-probe electrical conductivity method. The temperature of the sample was maintained by a separate refrigerator which operated between 20-350 K.

The magnet consists of a single-coil $Nb_3Sn$ multi-filamentary core of 1mm diameter fabricated by modified jelly- roll process with 53% copper content to allow easy heat dissipation. This wire can pass a current of 240 amps as well as to

minimize the coil temperature below 60 K when the coil quench occurs at high .currents [5]. Leads made of 2223 high-$T_c$ bismuth cuprate with a current carrying capacity at 300 amps at 77 K are connected between the $Nb_3Sn$ coil and the copper end terminals.

The first stage of a GM Sumitomo cryo-cooler (model SRDK-408 with 1.0 Watt cooling capacity at 4.2 K) is coupled to the high-$T_c$ leads and the second stage is connected to the $Nb_3Sn$ magnet coil. The temperature of the coil was maintained below 4.2 K while energizing or de-energizing the magnet at a rate 0.04 A/sec or lower. Super-insulation of 15 layers around the superconducting coil eliminated thermal losses. The cryostat has a 52 mm bore with a quartz window of 20 mm dia incorporated at the bottom of the coil to enable light to pass through (Fig. 3.7). Silicon diode, Cernox and RTD sensors at crucial places to monitor the temperature of each section and also control the temperature of the measuring sample.

## 3.3 References

1. C. N. R. Rao, *Chemical approaches to synthesis of inorganic materials*, (1994, John Wiley, New York).
2. C. N. R. Rao and J. Gopalakrishnan, *New directions in solid state chemistry*, (1986, Cambridge University press, UK).
3. A. Eyer, R. Nietsche and H. Zimmermann, *J. Cryst. Growth*, 47, 219, 1979.
4. A. M. Balbashov and S. K. Egorov, *ibid*, 52, 498, 1981.
5. G. Svenconis, L.Ying, A. R. Raju and C. N. R. Rao, *Current Science*, 77, 574, 1999.

# 4. RESULTS AND DISCUSSION

## 4.1 Cation-deficient lanthanum manganates, $Ln_{1-x}MnO_3$ and $LaMn_{1-x}O_3$ ($x$=0-0.1)

The cation-deficient lanthanum manganates grown by the floating zone melting technique were first cut into small pieces of dimension, 4 mm in dia and 2 mm in thickness. The samples were then annealed in a flow of oxygen for 24-72 h to obtain the desired electron transport properties.

***4.1.1 Characterization:*** Fig. 4.1.1 shows the EDX patterns of the four crystals of the cation-deficient manganates. The estimated La:Mn ratios in the $LaMnO_3$, $La_{0.96}MnO_3$, $La_{0.9}MnO_3$ and $LaMn_{0.9}O_3$ crystals were 1:1, 0.96:1, 0.9:1 and 1:0.9 respectively. The polished surfaces of the crystals were examined by using SEM. Typical images are shown in Fig. 4.1.2. The surface images are smooth, with no evidence of segregation and twin boundaries. Typical X-ray diffraction plots are shown in Fig. 4.1.3. The pure $LaMnO_3$ crystallizes in monoclinic crystal structure. $La_{0.9}MnO_3$ crystallizes in rhomohedral, while $La_{0.96}MnO_3$ and $LaMn_{0.9}O_3$ crystallize in orthorhombic crystal structure. The refined unit cell parameters for the crystals from X-ray diffraction data are given in Table 4.1.1. All the crystals showed orthorhombic symmetry except $La_{0.9}MnO_3$, which showed rhombohedral symmetry. The unit cell dimensions decreased with increase in the lanthanum deficiency as expected when a $Mn^{4+}$ ion replaces a Jahn-Teller $Mn^{3+}$ ion.

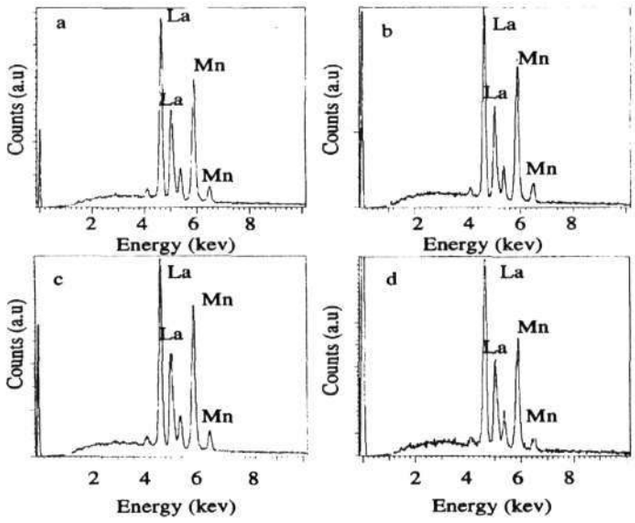


***Fig. 4.1.1*** *EDX patterns of* ***(a)*** *$LaMnO_3$.* ***(b)*** *$La_{0.96}MnO_3$.* ***(c)*** *$La_{0.9}MnO_3$ and* ***(d)*** *$LaMn_{0.9}O_3$.*

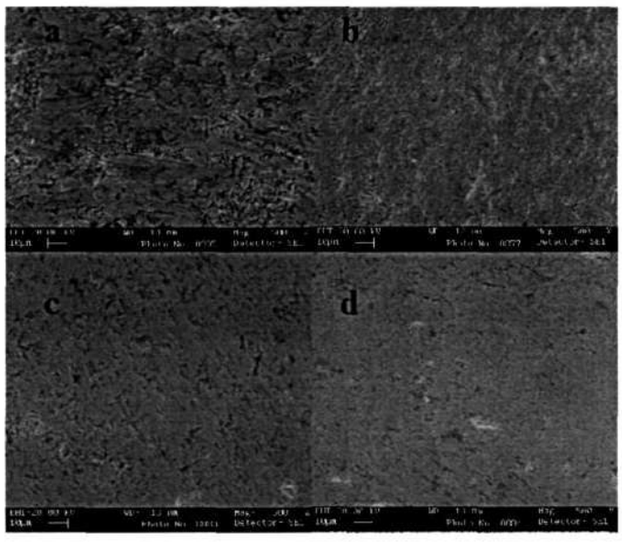


***Fig. 4.1.2*** *Scanning electron micrographs of* ***(a)*** *$LaMnO_3$.* ***(b)*** *$La_{0.96}MnO_3$.* ***(c)*** *$La_{0.9}MnO_3$. and* ***(d)*** *$LaMn_{0.9}O_3$.*

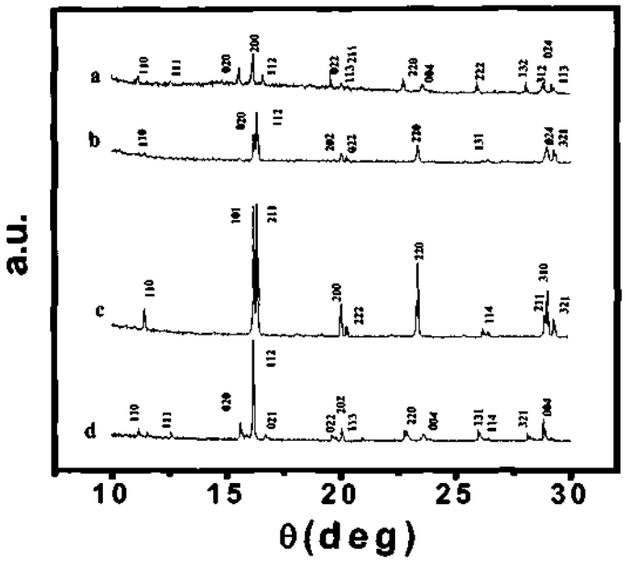


***Fig. 4.1.3*** *X-ray diffraction pattern of pure and cation deficient $LaMnO_3$.* ***(a)*** *$LaMnO_3$.* ***(b)*** *$La_{0.96}MnO_3$.* ***(c)*** *$La_{0.9}MnO_3$.* ***(d)*** *$LaMn_{0.9}O_3$.*

***Table 4.1.1*** *Lattice parameters of cation-deficient $LaMnO_3$*

| Compositions | a(Å) | b(Å) | c(Å) |
|---|---|---|---|
| $LaMnO_3$ | 5.5367 | 5.7429 | 7.7023 |
| $La_{0.96}MnO_3$ | 5.5326 | 5.6764 | 7.7009 |
| $La_{0.9}MnO_3$ [(a)] | 5.4751 | - | - |
| $LaMn_{0.9}O_3$ | 5.5385 | 5.7157 | 7.6971 |

(a) Rhombohedral

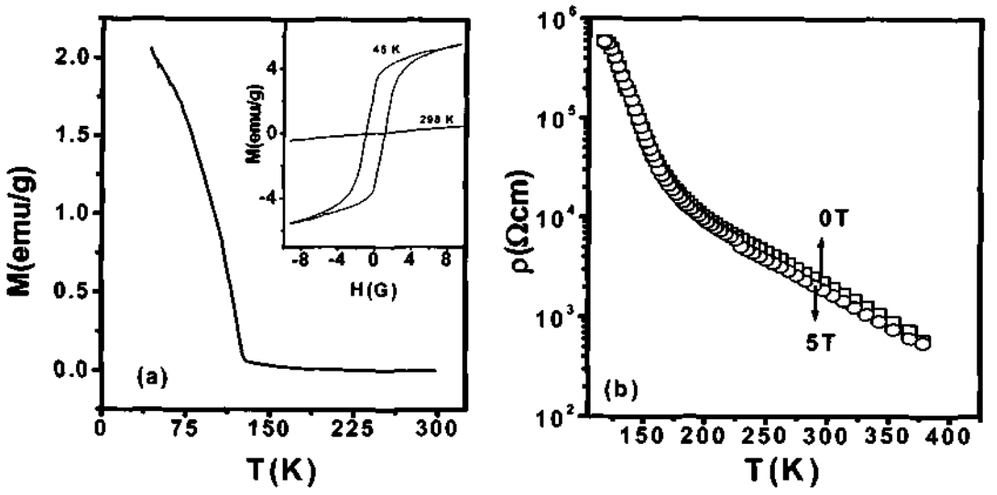


*Fig. 4.1.4 (a) Temperature variation of magnetization of $La_{0.96}MnO_3$ single crystal. The inset shows the hysteresis loop at 45 K. (b) Temperature variation of resistivity at different magnetic fields.*

***4.1.2 $LaMnO_3$:*** The $LaMnO_3$ single crystal shows the expected insulating behavior from room temperature down to 20 K. Magnetization measurements carried out at 100 gauss shows that the compound exhibits an anti-ferromagnetic transition around 150 K and shows weak canted antiferromagnetism at low temperatures due to the presence of some vacancies. Application of a magnetic field of 5T has no effect on the resistivity of this manganate.

***4.1.3 $La_{0.96}MnO_3$:*** The magnetization data (Fig. 4.1.4a) shows a weak ferromagnetic-like transition at 130 K, but no saturation. We observe magnetic hysteresis at low temperatures as shown in the inset of Fig. 4.1.4a. The magnetization value at 9000 G is low aspected of mangnates which do not show saturation. Fig. 4.1.4b shows the temperature variation of the electrical resistivity of a $La_{0.96}MnO_3$ crystal. This manganate is an insulator. Application of a magnetic field of 5T has no effect on the resistivity for this crystal. The observed magnetic

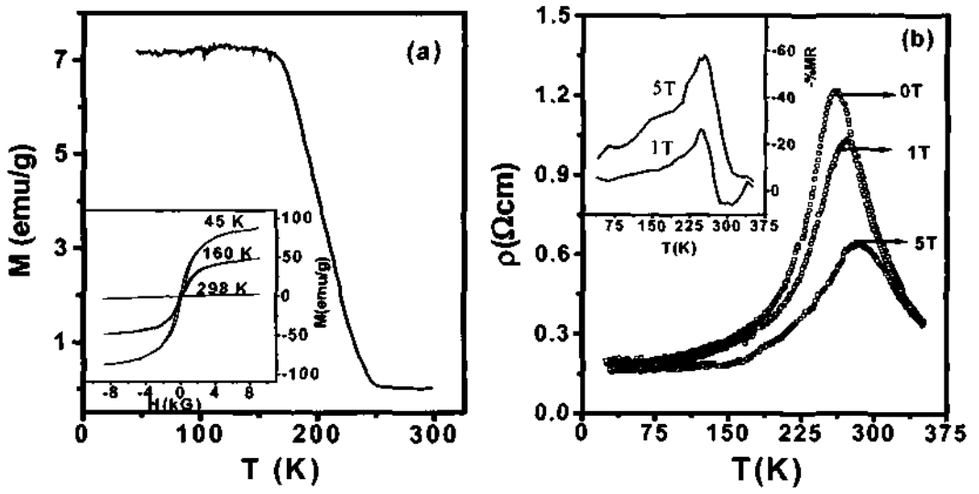


*Fig. 4.1.5 (a) Temperature variation of magnetization data of $La_{0.9}MnO_3$. Inset shows the hysteresis curves at various temperatures. (b)Temperature variation of resistivity of $La_{0.9}MnO_3$ single crystal under different magnetic fields. The inset shows the temperature variation of the magnetoresistance at 1 and 5T.*

properties can arise from the presence of ferromagnetic clusters in antiferromagnetic/paramagnetic host.

***4.1.4 $La_{0.9}MnO_3$:*** Magnetization data of crystals of $La_{0.9}MnO_3$ (Fig. 4.1.5a) show a good ferromagnetic transition and saturation behavior. This manganate shows excellent magnetic hysteresis below 250 K. The value of the saturation magnetization ($M_s$) at 45 K is 82 emu/g at 0.9 T. Typical hysteresis loop data are shown in the inset of Fig. 4.1.5a. In contrast to $La_{0.96}MnO_3$, $La_{0.9}MnO_3$ shows a sharp IM transition at 250 K (Fig. 4.1.5a). The ferromagnetic metallic sample also shows colossal magnetoresistance (CMR) at the IM transition temperature (Fig.4.1.5b). The literature values of CMR for this composition are between 50 and 55% around $T_c$ [1,2]. Application of a magnetic field causes considerable change in the resistivity, particularly around $T_c$. The negative magnetoresistance reaches 58% for 5T at 255 K, and 26% for 1T field at 245K (inset of Fig. 4.1.5b).

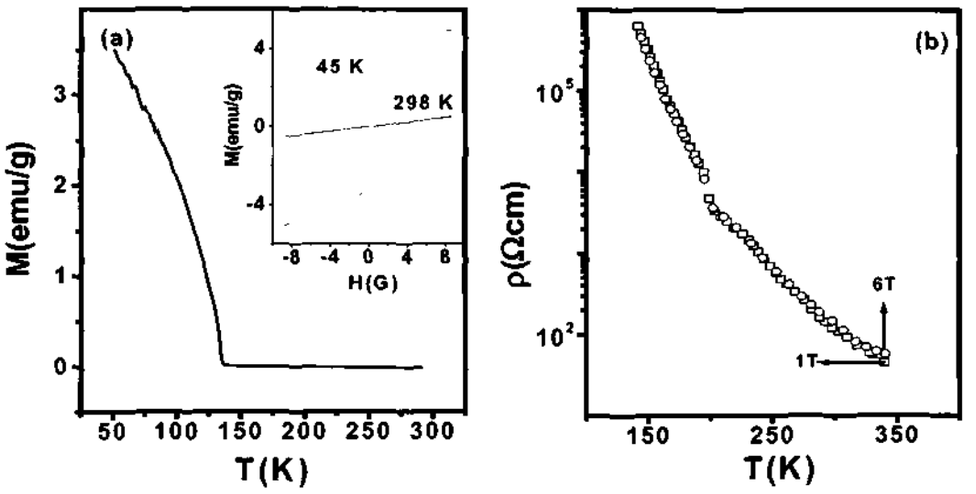


*Fig. 4.1.6 (a) Temperature variation of magnetization of $LaMn_{0.9}O_3$ single crystal. The inset shows the hysteresis loops. (b) Temperature variation of resistivity at different magnetic fields.*

***4.1.5 $LaMn_{0.9}O_3$:*** Magnetization data show a transition around 150 K similar to the one observed in $La_{0.96}MnO_3$, but there is no saturation behavior as shown in Fig. 4.1.6a. We find magnetic hysteresis at low temperatures (see inset of Fig. 4.1.6a). Electrical resistivity of the $LaMn_{0.9}O_3$ crystal shows it to be an insulator from 350 K to 20 K (Fig. 4.1.6b). Just as in $La_{0.96}MnO_3$, magnetic fields have no effect on the resistivity of $LaMn_{0.9}O_3$. The insulating behavior of $LaMn_{0.9}O_3$ is because of the deficiency in the crucial Mn sites responsible for conduction. The sharp change in slope of the resistivity curve of the $LaMn_{0.9}O_3$ crystal around 180 K may arise from charge ordering. Note that the composition of the crystal can be written as $LaMn_{0.6}^{3+}Mn_{0.3}^{4+}O_3$.

***Table 4.1.2*** *Magnetic and electrical transport properties of the crystals of cation-deficient $LaMnO_3$.*

| Compositions | $T_c$(K) | $T_{IM}$(K) | -%MR@$T_{IM}$ | $M_r$(emu/g) | $H_c$(G) |
|---|---|---|---|---|---|
| $La_{0.96}MnO_3$ | - | - | - | 5.5 | 1036 |
| $La_{0.9}MnO_3$ | 250 | 255 | 58 | 82 | 220 |
| $LaMn_{0.9}O_3$ | - | - | - | 4.9 | 896 |

***4.1.6 Conclusions:*** The present study shows that we can grow satisfactory single crystals of self- doped $LaMnO_3$ by the floating zone technique. Of the compositions studied, $La_{0.9}MnO_3$ exhibits all the desired properties of ferromagnetism, IM transition and CMR. When the lanthanum deficiency in $La_{1-x}MnO_3$ is less than 0.1, one does not observe CMR or good magnetization. Cation deficiency in the Mn site, however, does not bestow the same properties as deficiency at La site, as one would expect. Since Mn deficiency directly affects electron hopping and magnetism, $LaMn_{0.9}O_3$ shows poor magnetic properties and no CMR. For purpose of comparison we have listed the magnetic and electrical transport properties of the various compositions of the cation-deficient compositions studied are listed in Table 4.1.2.

## 4.2 Electric current-induced effects in charge-ordered $Nd_{0.5}Ca_{0.5}MnO_3$ and $Pr_{0.6}Ca_{0.4}MnO_3$ manganates

***4.2.1 Resistivity data:*** In Fig. 4.2.1, we show the resistivity of a $Pr_{0.6}Ca_{0.4}MnO_3$ and $Nd_{0.5}Ca_{0.5}MnO_3$ crystal at different applied currents when the sample is cooled from 300 K. There are four distinct features in the plot. There is a drop in the resistivity throughout the temperature range as the current, I, is increased. The temperature dependence of the resistivity changes with the increase in I. An insulator-metal transition occurs around 60 K ($T_{IM}$) at high values of I, beyond a threshold value. The change in the resistivity is not due to Joule heating as can be evidenced from the negative temperature co-efficient of resistivity at high temperatures and the change in sign at the IM transition. In fact, the irrelevance of the Joule heating can also be seen in the low-temperature metallic (positive temperature coefficient of resistivity) regime accessible in Fig.4.2.1a. Here the resistance for a given current increases with increasing temperature, while for a given temperature the resistance decreases with increasing current. Just the opposite would be true for a Joule heating. It is reasonable, therefore, to assume that the Joule heating is quite irrelevant to our transport results, qualitatively at least.

The negative differential resistance, i.e., the decrease in resistivity with increasing in current observed beyond a certain value of I (see Fig.4.2.1a and 1b) is due to the presence of the metallic filaments, which are ferromagnetic and carry most of the current [3]. The rather high value of the resistivity below the transition temperature is attributed to the co-existence of the FM and CO insulator phases.

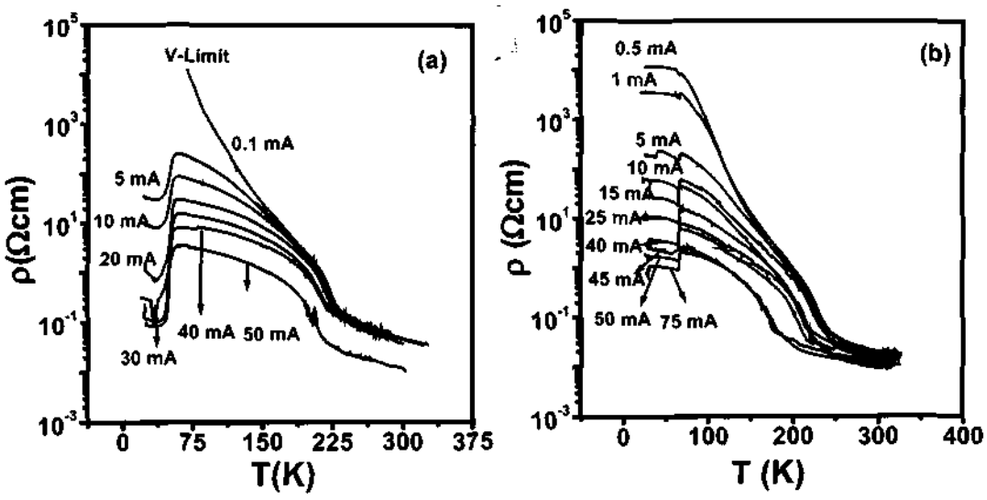


*Fig. 4.2.1 Temperature variation of resistivity of (a) $Pr_{0.6}Ca_{0.4}MnO_3$ and (b) $Nd_{0.5}Ca_{0.5}MnO_3$ crystals.*

The relative fraction of the FMM phase increases with increasing current causing a lowering of resistivity below the $T_{IM}$ [4,5]. The small rise in resistivity below the IM transition may be attributed to the tunneling of electrons between the FMM clusters through COI clusters.

***4.2.2 Charge-ordering transition:*** The charge ordering transition temperature, $T_{co}$, shifts to lower values with increase in I and become constant beyond a high I value (~50 mA). Such a current-induced shift in $T_{co}$ is indeed noteworthy. The plot of $T_{co}$ against I (see Fig. 4.2.2) is linear with a slope of ~0.8 and 1 K/mA for $Pr_{0.6}Ca_{0.4}MnO_3$ and $Nd_{0.5}Ca_{0.5}MnO_3$. The decrease in the $T_{co}$ is attributed to the charge delocalization driven by external current. The charge ordering resulting from charge localisation at the $Mn^{3+}$ site induces a lattice strain due to the mismatch between the $Mn^{3+}$ and $Mn^{4+}$ octahedra. Current through the sample induces delocalization of the charge carrier decreasing lattice distortion and $T_{co}$ (see the schematic in Fig.4.2.3).

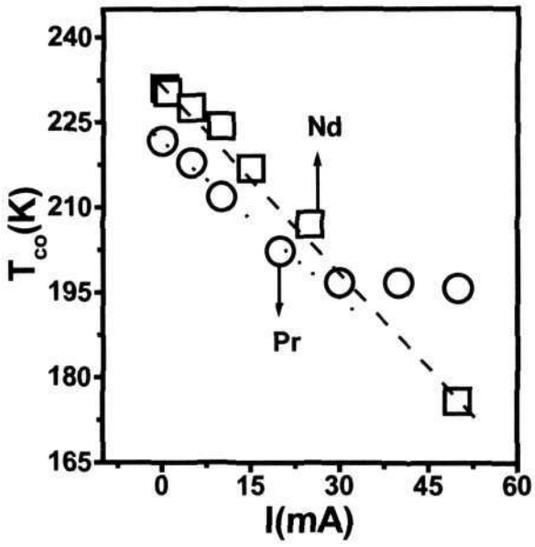


***Fig. 4.2.2*** *Variation of charge ordering temperature with current passing through the $Pr_{0.6}Ca_{0.4}MnO_3$ crystal.*

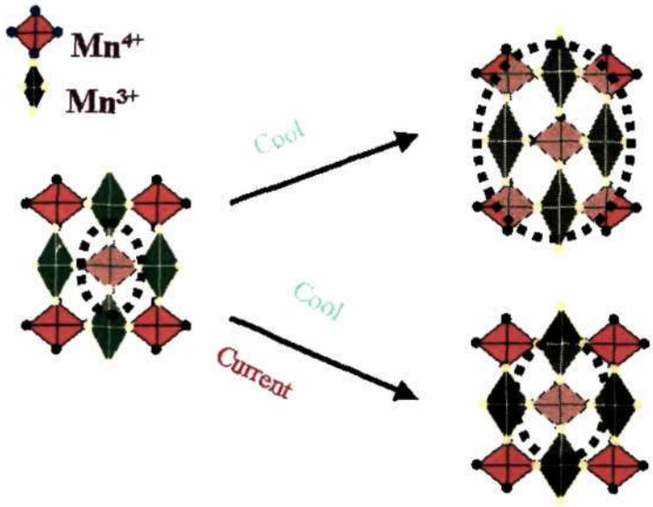


***Fig. 4.2.3*** *Schematic showing the mechanism of decrease in the $T_{co}$ due to reduction of strain upon passing a current through the charge-ordered crystal.*

The lowering of lattice distortions caused by the substitution at the A-site in $(La_{1-x}Pr_x)_{0.7}Ca_{0.3}MnO_3$ gives rise to a ferromagnetic transition at low temperatures [6]. We observe a similar behavior in the CO manganates where the increasing current lowers the lattice distortion and favors ferromagnetism and metallicity (Fig.4.2.1a).

***4.2.3 Electroresistive ratio:*** As the current through the $Pr_{0.6}Ca_{0.4}MnO_3$ crystal is increased, there is a drastic change in the resistivity. The $\rho_{0.1}/\rho_I$ ratio where $\rho_{0.1}$ is the resistivity at a current of 0.1 mA (which is the smallest I employed by us) and $\rho_I$, the resistivity at a given applied current, I, may be considered to represent the electroresistive ratio analogous to the magnetoresistive ratio.

In Fig.4.2.5a we show the temperature variation of $\rho_{0.1}/\rho_I$ for different I values. The change in resistivity at low temperatures (~20 K) is four orders of magnitude while it is one or two orders at high temperatures ($T \approx T_{co}$). The four orders of magnitude change in the resistivity is achieved by changing the applied current by two orders, indicating the non-ohmic behavior. As the current is increased, we observe a sharp drop in resistivity of the sample at the insulator-metal transition temperature, $T_{IM}$ (Fig. 4.2.1) a behavior not noticed in earlier films. When the ρ-T data are recorded in the warming run without turning off the current, we observe a thermal hysteresis, which becomes a prominent at large current.

***4.2.4 Thermal hysteresis:*** The observation of hysteresis suggests a first-order nature of the structural change induced in the transition. In the warming run, the low resistive state persists down to a temperature $T_W$, lower than $T_{IM}$ (Fig.4.2.4b). The thermal hysteresis observed here is somewhat different from that formed in a

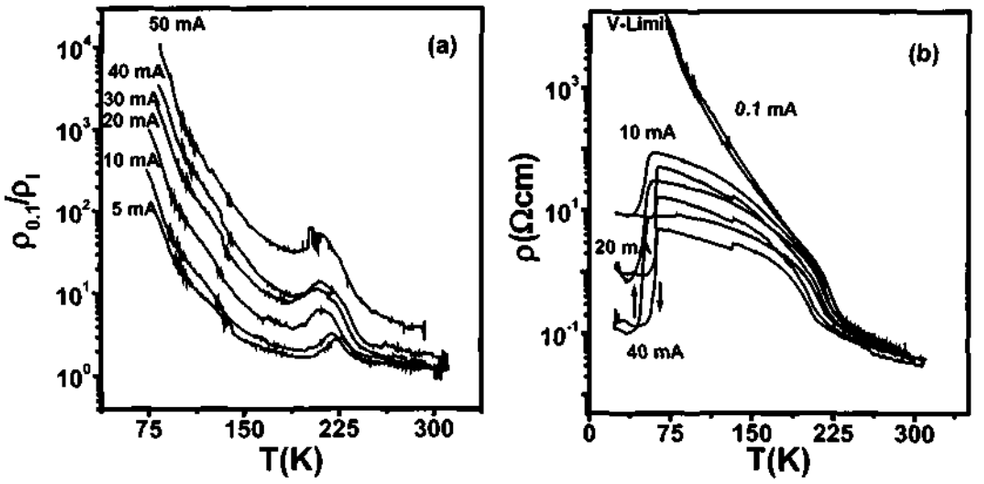


*Fig. 4.2.4 (a)Temperature variation of electro resistive ratio of $Pr_{0.6}Ca_{0.4}MnO_3$ at different currents. (b) Temperature hysteresis of $Pr_{0.6}Ca_{0.4}MnO_3$ at different currents.*

normal ferromagnetic metal at the IM transition. The transition temperature in the cooling cycle is higher than in the warming cycle in the present case because of competing FM and AFM correlations. The current-induced unusual hysteresis is attributed to the competition between the FMM and the CO-AFMI phases near the IM transition [7]. The transition from the metallic-type state to the insulating state is associated with greater charge localization compared to the transition from the insulating state to the metallic state.

The resistivity change at $T_W$ increases with the increasing current. Both $T_{IM}$ and $T_W$ are independent of the applied current as also the ratio of the peak resistivity in the heating and the cooling runs. If one compares the change in the resistivity to the ratio of resistivities, the phenomenon is quite striking (Fig.4.2.5a).

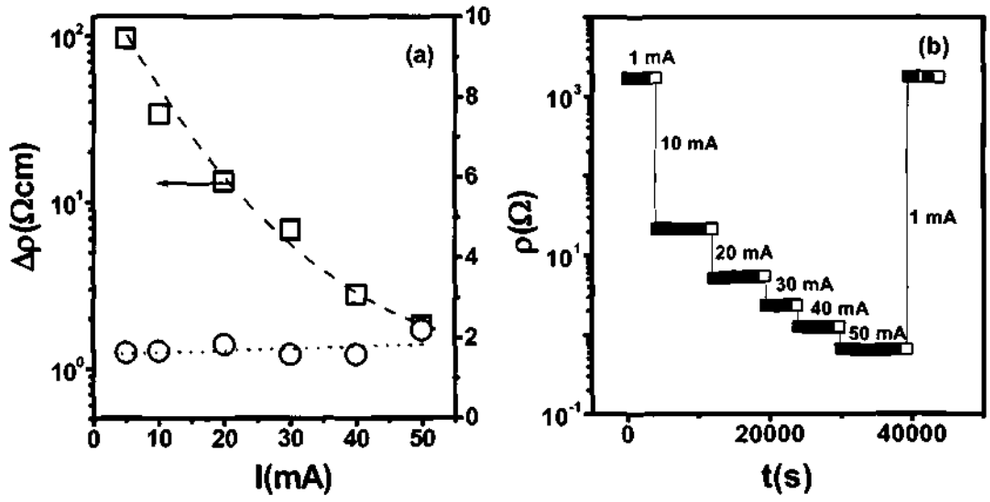


*Fig. 4.2.5 (a) Squares are difference between the resistivity of $Pr_{0.6}Ca_{0.4}MnO_3$ in the cooling and warming cycle. Circles represents the ratio of the resistivities at the IM transition. (b) Variation of resistivities of $Pr_{0.6}Ca_{0.4}MnO_3$ with time at different currents at 20 K.*

A time-dependent resistivity study of $Pr_{0.6}Ca_{0.4}MnO_3$ crystals at low temperatures shows that the resistivity does not vary with time for a given value of the current indicating that the decrease in resistivity with increase in current is not due to Joule heating (Fig. 4.2.5b). The metallic-like states of the crystals appear to be stable with time and current. The resistivity of the sample switched to the value at t = 0 when the current was decreased to the initial value showing thereby that the switching is associated with a memory [3].

***4.2.5 I-V characteristics:*** The I-V characteristics on the $Pr_{0.6}Ca_{0.4}MnO_3$ crystals show that the negative differential resistance (NDR) is observed below antiferromagnetic transition (~150 K) and the threshold current for NDR decreases

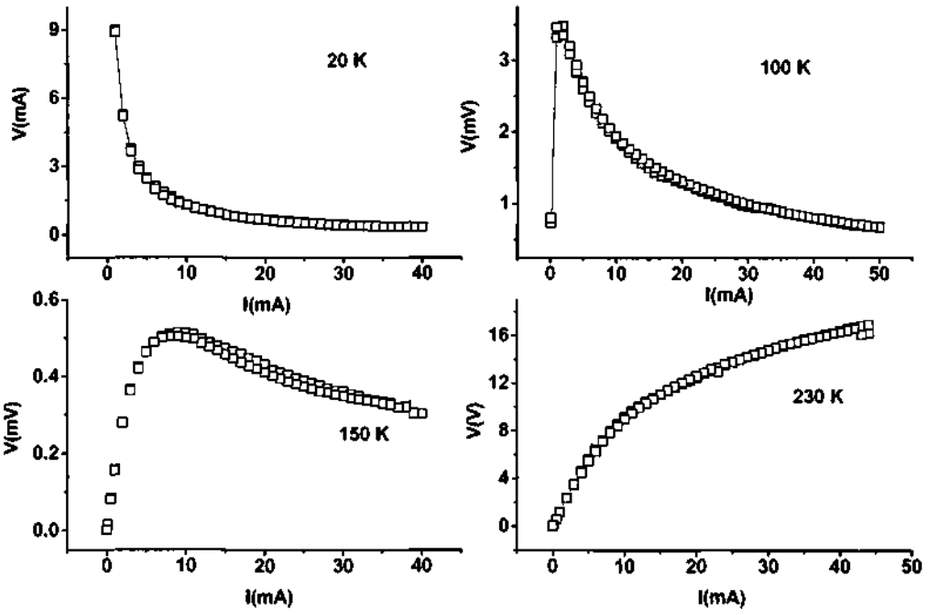


*Fig. 4.2.6 I-V characteristics of $Pr_{0.6}Ca_{0.4}MnO_3$ crystal at different temperatures.*

with decrease in temperature. Rao and co-workers have discussed the NDR in great detail, and have established that the current-induced metallic regions are ferromagnetic [8].

When the current is switched off at low temperatures, the current source is not able to pass the same current in the sample when the current is again switched on at the same low temperature due to voltage limit (V-Limit 105 V) of the source. This implies that the resistivity of the sample becomes high on switching off the current and the source meter is unable to pass the required current with the maximum voltage drop it can generate across the leads (which was possible before switching off the current). The effect of the current in the warming run is quite

different from that in the cooling run the resistivities and the $T_{co}$ in the former being higher.

***4.2.6 Conclusions:*** The main findings from the present study are as follows. Passing relatively high currents through the charge-ordered manganates, as a general rule, cause an insulator-metal transition at $T_{IM}$. This is unlike the effect of magnetic field in the charge-ordered manganates where only those with $< r_A > >$ 1.18 Å could be transformed into the metallic state at fields ≤ 15 T. Accordingly, both $Nd_{0.5}Ca_{0.5}MnO_3$ and $Pr_{0.6}Ca_{0.4}MnO_3$ attain the metallic state at low temperatures and high currents. The electroresistive ratio increases with increasing current and the charge ordering transition temperature decreases with increasing current.

The magnitude of drop in the resistivity at the insulator-metal transition parallels the effect of magnetic fields in some respect. Thus, the drop in resistivity in $Pr_{0.6}Ca_{0.4}MnO_3$ is much higher than that of $Nd_{0.5}Ca_{0.5}MnO_3$ for similar currents. It may be noted that $Nd_{0.5}Ca_{0.5}MnO_3$ contains two phases below $T_{co}$ [9], and ferromagnetic correlations are present at low temperatures [10]. The presence of two phases below $T_{co}$, in $Pr_{0.6}Ca_{0.4}MnO_3$ with one phase having spin-glass like features has also been shown recently [11]. On the application of a reasonably high electric current, metallic domains are likely to grow in size. Such a metal-like phase generated by electric fields will also be magnetic [8]. The metal-like conduction around 65 K may be facilitated by the separation of FMM, CO insulator and paramagnetic phases. When the ρ-T data are recorded in the warming run without turning off the current, we observe a thermal hysteresis, which becomes a prominent at large current.

## 4.3 Electric current-induced first-order effects on the insulator-metal transition and the colossal electroresistance in rare earth manganates.

### 4.3.1 $La_{0.77}Ca_{0.23}MnO_3$

***4.3.1a Resistivity data:*** Magnetization data of $La_{0.77}Ca_{0.23}MnO_3$ and $La_{0.9}MnO_3$ show ferromagnetic Curie temperatures, $T_c$ of 230 and 259 K respectively. In Fig.4.3.1, we show the effect of varying electric currents on the insulator-metal (IM) transition in $La_{0.77}Ca_{0.23}MnO_3$, in the cooling and warming cycles is shown. We readily see that the IM transition temperature, $T_{IM}$, which is close to the ferromagnetic $T_c$, decreases with the increase in current, although there is little change in the peak resistance. In Fig.4.3.2a, the $T_{IM}$ values in the cooling and warming cycles are plotted against the applied current. The $T_{IM}$ value decreases markedly with increasing current, in both the cooling and warming cycles. The value of $T_{IM}$ reaches as low as 190 K for 60 mA current, which is 40 K lower than the expected $T_c$ of the compound.

***4.3.1b Thermal hysteresis:*** While there is little hysteresis at a small value of the current (0.1 mA), the magnitude of hysteresis, $\Delta T$, increases with increasing current linearly, as shown in the inset of Fig.4.3.2b. A maximum hysteresis of 20 K is seen for 60 mA current. These data demonstrate that the applied current increasingly induces first-order characteristics on the IM transition and that the observed effects are thermodynamic.

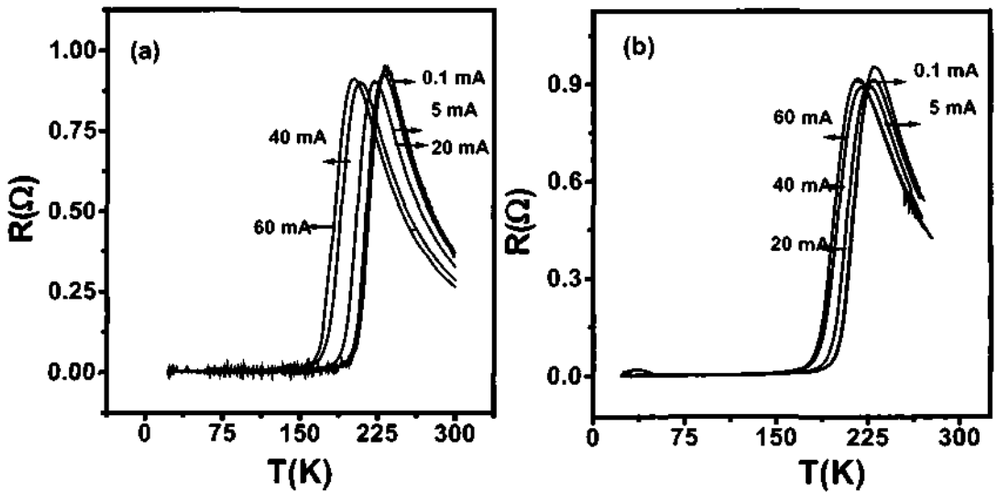


*Fig. 4.3.1 Temperature variation of resistance of $La_{0.77}Ca_{0.23}MnO_3$ crystals at different current values. (a) Cooling cycle. (b) Warming cycle.*

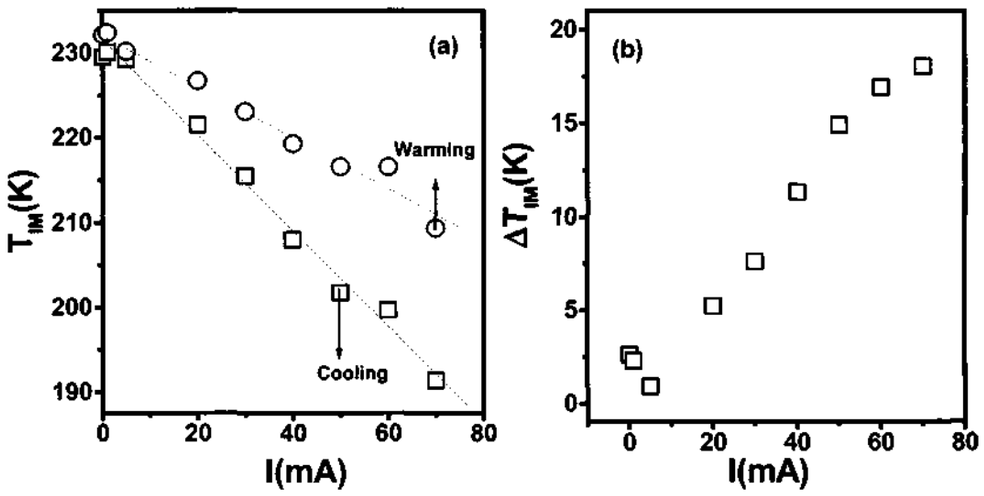


*Fig. 4.3.2 (a) Current variation of $T_{IM}$ of $La_{0.77}Ca_{0.23}MnO_3$. (b) Difference between the $T_{IM}$ ($\Delta T_{IM}$) in the warming and cooling cycle of $La_{0.77}Ca_{0.23}MnO_3$.*

***4.3.1c Electroresistive ratio:*** If we designate the IM transition temperature at the lowest applied current (0.1 mA) as $T_{IM}^{o}$, a current-induced decrease in resistance at $T > T_{IM}^{o}$ and a marked increase in resistance at $T < T_{IM}^{o}$ are observed. We can define an electroresistive ratio, ER, as

$$\%ER = \frac{R(I) - R(I\min)}{R(I\min)} X100$$

where *R(I*min*)* is the resistance at the lowest applied current at a given temperature and *R(I),* the resistance at a higher value of the current. In figure 4.3.3, we plot % ER for $T > T_{IM}^{o}$ for different values of the applied current. The value of %ER at room temperature for small current (5 mA) is around 10 which is comparable to a GMR material. As the current through the sample is increased, the %ER reaches -40% around 240 K and remains around -30% even around room temperature. In the warming cycle the value of negative ER is low compared to the cooling cycle. A maximum of –25% is obtained around 240 K for a current of 60 mA.

The positive ER in figure 4.3.4b obtained for resistance for temperatures $T < T_{IM}^{o}$ reaches very high values in the 200-150 K range. The value of positive ER increases with increasing current and peaks around 200 K, reaching high values of 5000 for 60 mA in the cooling cycle. In the warming cycle, the values are small reaching a high value of 1500 around 200 K for 60 mA. Such colossal electroresistance could find applications.

### *4.3.2 $La_{0.9}MnO_3$*

We have examined current-induced effects on crystals of self-doped $La_{0.9}MnO_3$. In Fig.4.3.5a, the effect of applied current on the IM transition at different current

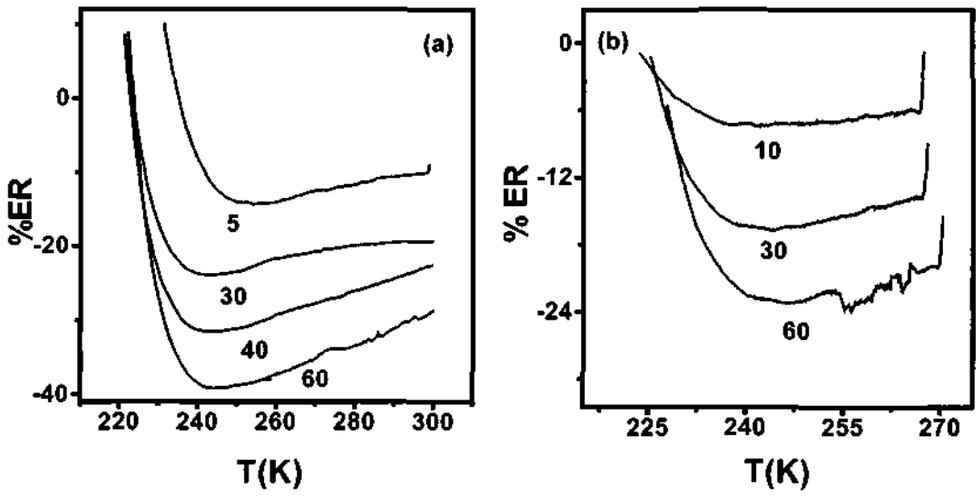


*Fig. 4.3.3 Temperature variation of negative electroresistive ratio of $La_{0.77}Ca_{0.23}MnO_3$ crystal in the **(a)** cooling cycle **(b)** warming cycle.*

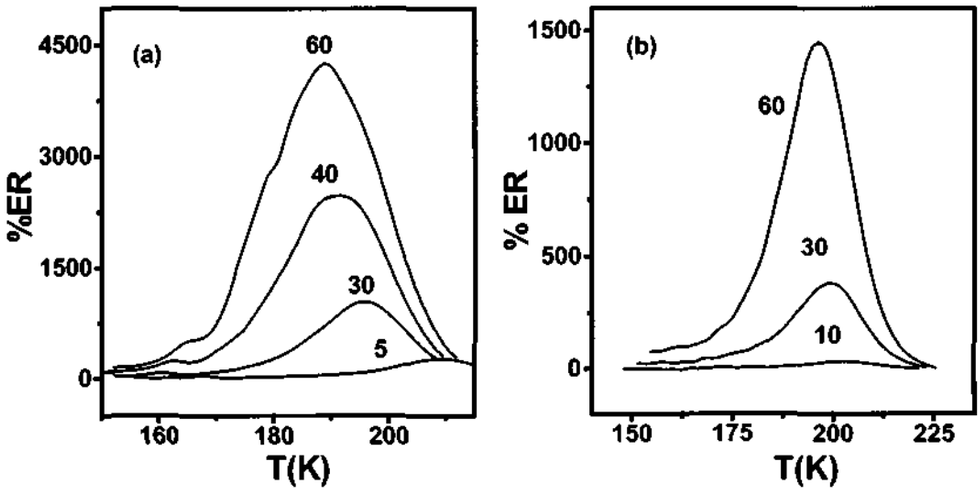


*Fig. 4.3.4 Temperature variation of positive electroresistive ratio of $La_{0.77}Ca_{0.23}MnO_3$ in **(a)** cooling cycle **(b)** warming cycle.*

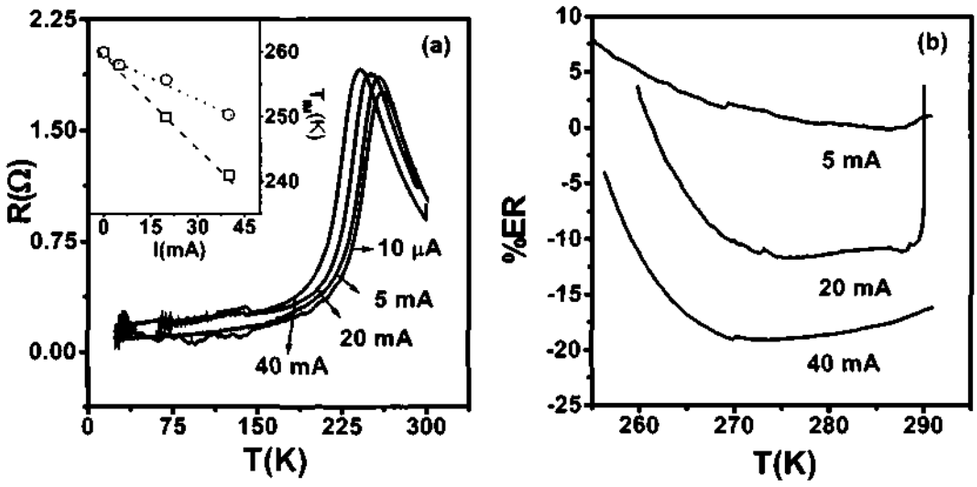


*Fig. 4.3.5 (a) Temperature variation of resistance in $La_{0.9}MnO_3$ for different currents. The squares and circles in the inset shows the $T_{IM}$ in the cooling and warming cycle. (b) Temperature variation of negative electroresistance of $La_{0.9}MnO_3$ in the cooling cycle.*

values in the cooling cycle is shown. The decrease in the $T_{IM}$ is somewhat smaller than in $La_{0.77}Ca_{0.23}MnO_3$.

The thermal hysteresis increases with increasing current as can be seen from the inset in Fig. 4.3.5a. There appears to be a threshold current below which the hysteresis appears to be negligible. The difference in the $T_{IM}$ in the warming and cooling cycles reaches a maximam value of 10 K for 60 mA.

The negative ER of $La_{0.9}MnO_3$ is low compared to $La_{0.77}Ca_{0.23}MnO_3$ with the room temperature ER value being negligible for small currents (Fig. 4.3.5b). The ER value increases with increasing currents and reaches a maximum of –20% around 270 K for 40 mA.

It must be noted that the effects discussed above are not due to ohmic heating. Such heating cannot explain our observations and one would expect, if any, an opposite effect with a decrease in the peak resistance for high currents. The

marked decrease in $T_{IM}$ with applied current is understandable since the magnetic order and its fluctuations are coupled strongly to electron transport in the manganates. The coupling is strong around $T_{IM}$ ($T_c$), manifesting as a resistance peak due to critical spin disorder scattering of the conduction electrons. In the presence of finite transport current under non-equilibrium conditions, one expects a softening of the spin wave excitation spectrum which would, in turn, enhance the spin fluctuations and lower the $T_c$. Such a charge-transport driven phase transition can indeed become first order.

***4.3.3 Conclusions:*** Passing electric currents through a single crystal of $La_{0.77}Ca_{0.23}MnO_3$ causes a marked decrease in the temperature of the insulator-metal transition, $T_{IM}$, the $T_{IM}$ decreasing with increasing current. The transition exhibits thermal hysteresis, the magnitude of which increases with increasing current. Large negative electroresistance is observed close to room temperature and a maximum of -35% is observed at 240 K. Large positive electroresistance is obtained at low temperatures. Similar results are observed with $La_{0.9}MnO_3$ as well. The shift in $T_{IM}$ and the electroresistance is less compared to $La_{0.77}Ca_{0.23}MnO_3$.

## 4.4. Grain size effects on charge ordering, phase segregation and related properties of rare earth manganates, $Nd_{0.5}A_{0.5}MnO_3$ (A = Ca or Sr).

**4.4.1 $Nd_{0.5}Ca_{0.5}MnO_3$:** The X-ray diffraction patterns of $Nd_{0.5}Ca_{0.5}MnO_3$ gel sintered at various temperatures were fitted to orthorhombic unit cell with a P*nma* space group (Fig. 4.4.1). The full-width-at-half-maximum decreases with increasing sintering temperature indicating that the grain size of the material increases with increasing sintering temperature. $Nd_{0.5}Sr_{0.5}MnO_3$ crystallizes in orthorhombic I*mma* space group (Fig. 4.4.2). The unit cell dimensions of both these manganates heated at different temperatures for 3h. is shown are Tables. 4.4.1a and 1b.

In figure 4.4.3, we show typical SEM images of $Nd_{0.5}Ca_{0.5}MnO_3$ sintered for 3 h at different temperatures. The images clearly show an increase in the grain size as the sintering temperature is increased. The average grain size increases from ~0.1 μm at 1173 K to ~2.5 μm at 1673 K. The unit cell volume also increases to some extent (0.48 %) on sintering to 1673 K. The grain size of the sample sintered at 1573 K for different periods also shows the expected increase, but the grain size was ~2 μm even after sintering for 12 h.

In figure 4.4.4a, the magnetic susceptibility data of $Nd_{0.5}Ca_{0.5}MnO_3$ sintered at different temperatures are depicted. The sample sintered at 1173 K shows the charge-ordering transition at 240 K ($T_{co}$) weakly, but the magnetization keeps increasing as the temperature is lowered to 50 K. There is no evidence of antiferromagnetic ordering around 140 K. The charge-ordering transition appears clearly in the samples sintered at 1273 K or above. The value of the magnetic

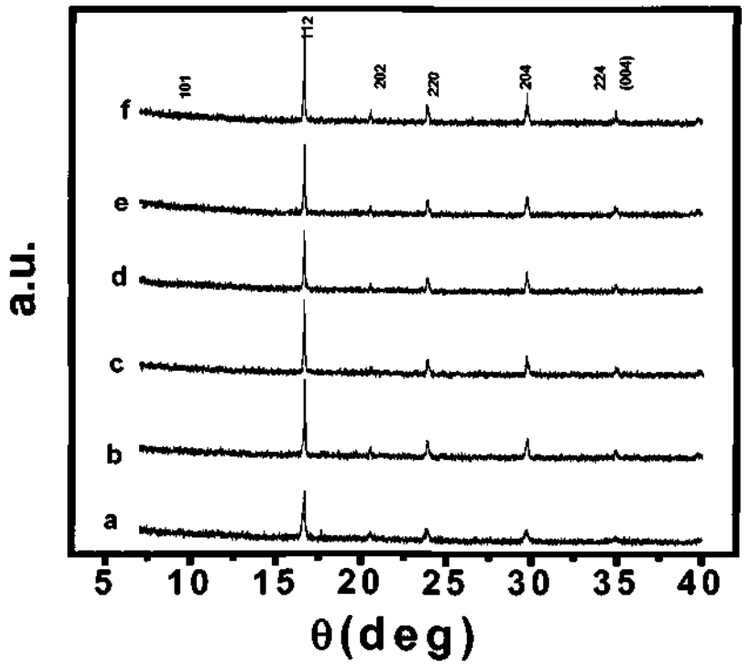


*Fig. 4.4.1 X-ray diffraction patterns of $Nd_{0.5}Ca_{0.5}MnO_3$ gel sintered at (a) 1173K. (b) 1273 K. (c) 1373 K. (d) 1473 K. (e) 1573 K and (f) 1673 K.*

susceptibility at $T_{co}$, increases to a small extent in the samples sintered to higher temperatures. The antiferromagnetic transition temperature shifts to slightly lower values in the samples sintered at higher temperatures (T > 1273 K). Thus, grain-size effects appear to be more marked on the antiferromagnetic ordering in $Nd_{0.5}Ca_{0.5}MnO_3$, although charge-ordering is affected to some extent. At the smallest grain size (1173 K, 3 h), the ferromagnetic interactions become prominent. This is likely to be due to phase segregation. We see the effects of phase segregation more vividly in the samples of $Nd_{0.5}Sr_{0.5}MnO_3$ sintered at different temperatures.

The resistivity of $Nd_{0.5}Ca_{0.5}MnO_3$ shows an insulating behavior with little variation in the temperature dependence of the resistivity. The room temperature resistivity value drops with increasing grain size as sintering reduces the porosity and increases conductivity in the material.

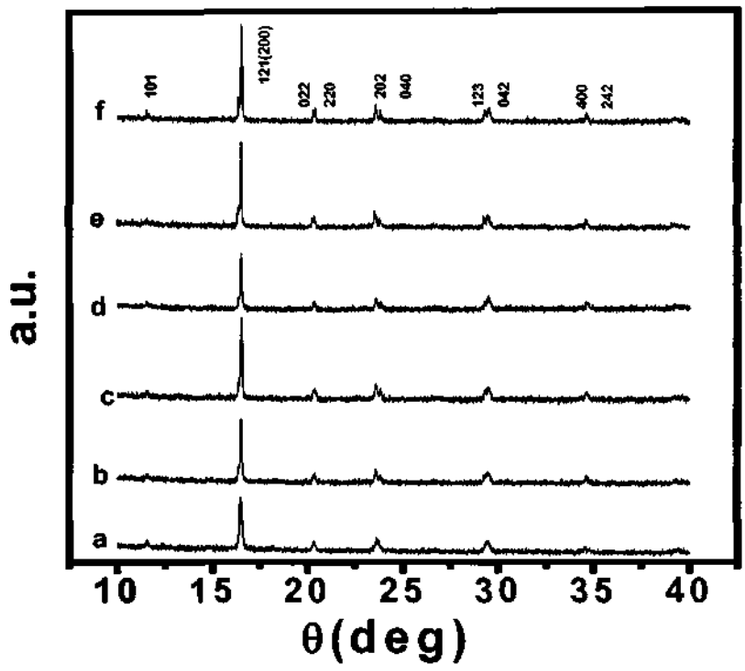


*Fig. 4.4.2 X-ray diffraction patterns of $Nd_{0.5}Sr_{0.5}MnO_3$ gel sintered at (a) 1173K. (b)1273 K. (c) 1373 K. (d) 1473 K. (e) 1573 K and (f) 1673 K.*

***Table 4.4.1a.*** *Unit cell dimensions of $Nd_{0.5}Ca_{0.5}MnO_3$ heated at different temperatures for 3 h.*

| T(K) | a(Å) | b(Å) | c(Å) | Vol.(Å$^3$) |
|---|---|---|---|---|
| 1173 K | 5.3797 | 7.5566 | 5.3994 | 219.49771 |
| 1273 K | 5.3841 | 7.5769 | 5.3883 | 219.81455 |
| 1373 K | 5.3648 | 7.5723 | 5.3839 | 218.71488 |
| 1473 K | 5.3878 | 7.6617 | 5.4049 | 223.11269 |
| 1573 K | 5.3806 | 7.6054 | 5.4056 | 221.20588 |
| 1673 K | 5.3778 | 7.5962 | 5.4349 | 222.02025 |

***Table 4.4.1b.*** *Unit cell dimensions of $Nd_{0.5}Sr_{0.5}MnO_3$ heated at different temperatures for 3 h.*

| T(K) | a(Å) | b(Å) | c(Å) | Vol.( Å$^3$) |
|---|---|---|---|---|
| 1173 K | 5.4245 | 5.4578 | 7.6663 | 226.96722 |
| 1273 K | 5.4242 | 5.4599 | 7.6655 | 227.0183 |
| 1373 K | 5.4164 | 5.4651 | 7.6975 | 227.85499 |
| 1473 K | 5.4171 | 5.4671 | 7.7071 | 228.25214 |
| 1573 K | 5.4179 | 5.4672 | 7.7007 | 227.59418 |

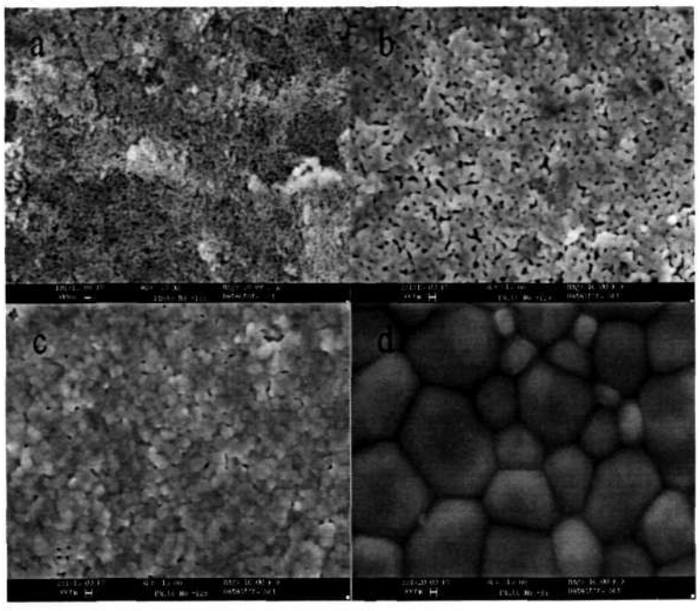


***Fig. 4.4.3*** *SEM micrographs of $Nd_{0.5}Ca_{0.5}MnO_3$ xerogel heated at* ***(a)*** *1173 K.* ***(b)*** *1273 K.* ***(c)*** *1473 K.* ***(d)*** *1673 K.*

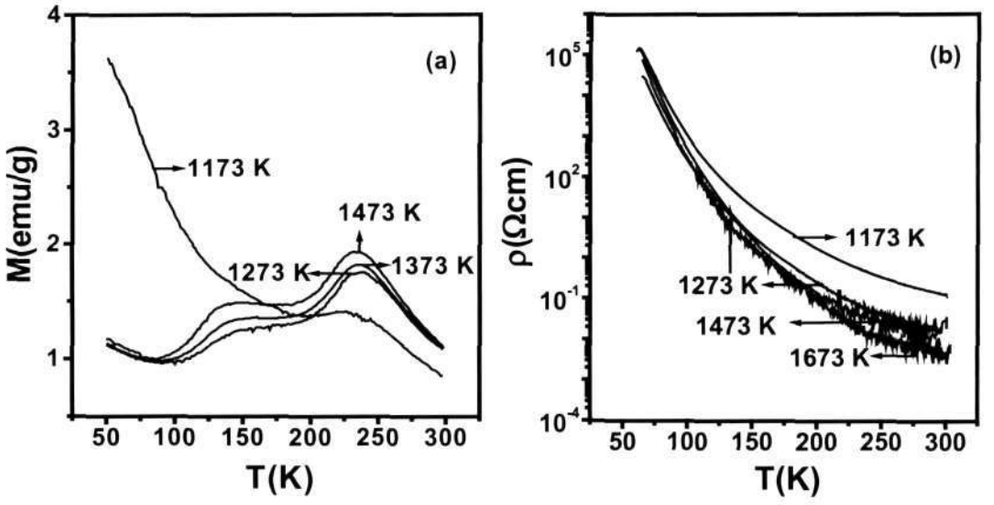


***Fig. 4.4.4 (a)*** *Temperature variation of magnetization of $Nd_{0.5}Ca_{0.5}MnO_3$ sintered at different temperatures.* ***(b)*** *Temperature variation of resistivity of $Nd_{0.5}Ca_{0.5}MnO_3$ sintered at different temperatures.*

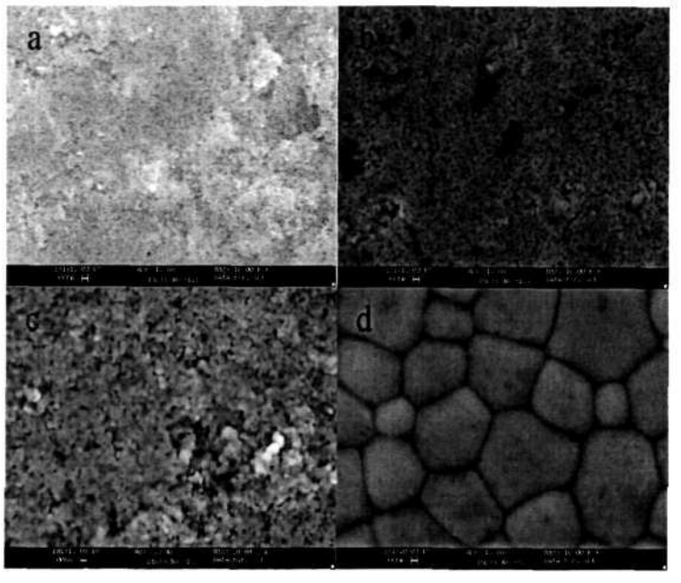


***Fig. 4.4.5*** *SEM micrographs of $Nd_{0.5}Sr_{0.5}MnO_3$ xerogel heated at* ***(a)*** *1173 K.* ***(b)*** *1273 K.* ***(c)*** *1473 K.* ***(d)*** *1673 K.*

**4.4.2 $Nd_{0.5}Sr_{0.5}MnO_3$:** In figure 4.4.5, the SEM images of $Nd_{0.5}Sr_{0.5}MnO_3$ sintered at different temperatures for 3h are shown. The grain size increases with the increasing temperature of sintering from ~0.1μm at 1173 K to ~2.1 μm at 1673 K. The unit cell volume also increases to a small extent on sintering at high temperatures. The grain size also increases when the gel is sintered at 1573 K for different periods, the size increasing with increasing duration of sintering. Thus, the grain size after sintering at 1573 K for 12 h was ~2μm, compared to 1μm after 3 h. The effect of temperature on the grain growth is marked compared to time.

In figure 4.4.6, the magnetization data of the $Nd_{0.5}Sr_{0.5}MnO_3$ gel sintered at different temperatures for 3 h are shown. The sample sintered at 1173 K shows a wide ferromagnetic transition around 270 K with the magnetization increasing gradually as the temperature is lowered below the $T_c$. The sample, however, does not exhibit charge-ordering and CE type antiferromagnetism at low temperatures. As we increase the temperature of sintering, the ferromagnetic transition temperature decreases from 274 K for 1173 K sintered sample to 250 K for 1673 K heated sample. Also, the width of the ferromagnetic transition decreases showing a relatively sharp transition in the sample sintered at 1673 K. If the width of the ferromagnetic transition is taken into account, the $T_c$ can be considered to be nearly constant. We start seeing the effect of charge-ordering and antiferromagnetism in samples sintered at 1273 K and above. The magnetization value is high in samples sintered at 1273-1473 K, and decreases to a small value in the sample sintered at 1573 K and above.

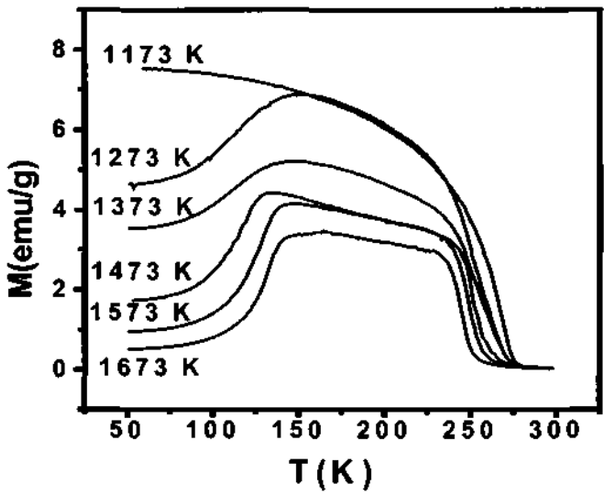


*Fig. 4.4.6 Temperature variation of magnetization of $Nd_{0.5}Sr_{0.5}MnO_3$ sintered at different temperatures.*

The sample sintered to 1673 K shows the decrease in magnetization around 150 K where the transition to a charge-ordered antiferromagnetic state occurs. Thus, the width of the low-temperature charge-ordering transition also decreases markedly with increasing grain size. What is clearly seen in Fig. 4.4.6 is that the apparent $T_c$-$T_{co}$ gap decreases markedly with the increase in grain size.

A sample of $Nd_{0.5}Sr_{0.5}MnO_3$ sintered for different durations at 1573K also shows a decrease in the value of the magnetization with the increasing period of sintering, accompanied by a sharpening of the charge-ordering transition (Fig. 4.4.7). The value of the low-temperature magnetization along the apparent $T_c$-$T_{co}$ gap decreases with the increasing grain size or the sintering temperature, the highest value being found in the sample sintered at 1173 K (gain size ~0.1μm).

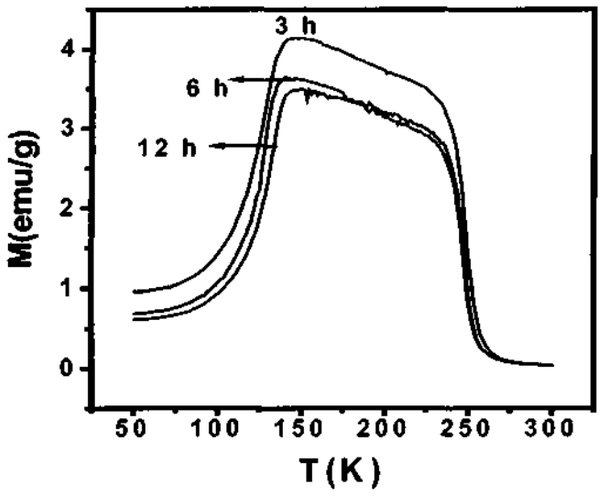


*Fig. 4.4.7 Temperature variation of magnetization of $Nd_{0.5}Sr_{0.5}MnO_3$ sintered at 1573 K for different time intervals.*

Thus, the effect of sintering of the sample at different time intervals at constant temperature appears to have similar effect as sintering at different temperatures at constant time. Hence, the transport properties of these manganates depend largely on the grain size and to a lesser extent on sintering temperature. Our observations can be understood qualitatively on the basis of the change in unit cell volume with the sintering temperature. It is also possible that the domains of the CO-AFM phase, unlike that of the FM phase, grows significantly only when the sample is sintered at a sufficiently higher temperature. The decrease in magnetization with increasing sintering temperature is likely to be due to the decrease in phase segregation. Thus, there is least segregation of the FM and AFM domains in the sample sintered at 1673 K, the segregation being greatest in samples sintered at 1273 K and below.

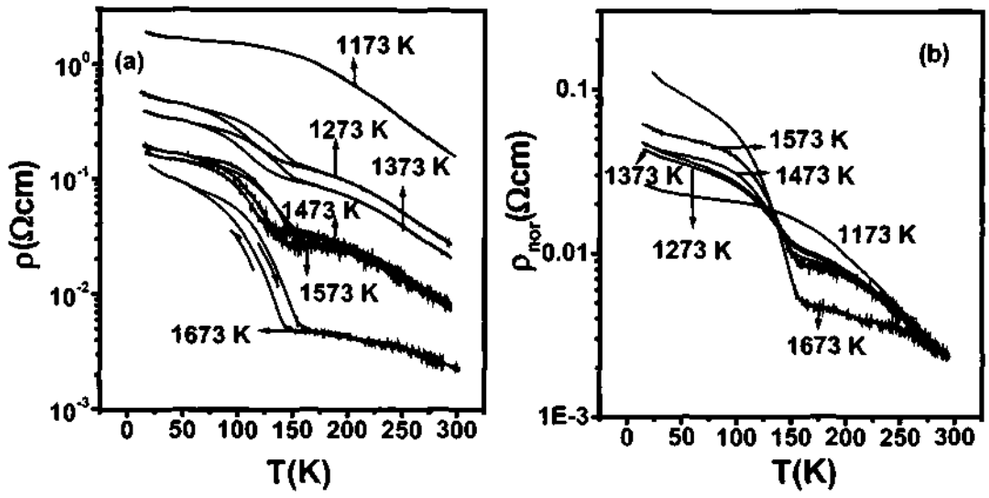


*Fig. 4.4.8 (a) Temperature variation of resistivity of $Nd_{0.5}Sr_{0.5}MnO_3$ sintered at various temperatures. (b) Temperature variation of normalized resistivity of $Nd_{0.5}Sr_{0.5}MnO_3$ sintered at various temperatures.*

Electrical resistivity measurements on $Nd_{0.5}Sr_{0.5}MnO_3$ sintered at different temperatures also show interesting trends (Fig. 4.4.8a). The sample sintered at 1173 K does not show the MI transition characteristic of the charge-ordering AFM transition, consistent with the magnetic measurements. We start seeing the MI transition in the sample sintered at 1273 K, which also shows a transition in the magnetization data (Fig. 4.4.6). The low-temperature charge-ordering transition become sharp in samples sintered at 1473 K and above (Fig. 4.4.6), the best behavior being found in the 1673 K sample, which shows the first order transition around 150 K. The magnitude of hysteresis at this transition is maximum in the sample sintered at 1673 K and decreases markedly at the lower sintering temperatures.

If the resistivity data in Fig. 4.4.8a is plotted by normalizing the resistivity values of samples sintered at different temperature to that of 1673 K heated sample

at 300 K, an interesting feature as shown in Fig. 4.4.8b is observed. All the resistivity curves pass through a narrow region (iso-resistive point) around 145 K, a temperature close to CO transition when the material becomes antiferromagnetic. The magnitude of resistivity beyond this point increases with the sintering temperature. The resistivity of the sample sintered at 1173 K barely passes through this iso-resistive region and does not show a jump in resistivity either; as expected for systems showing no charge ordering. We can therefore consider the magnitude of resistivity jump at T < 145 K as also a measure of phase segregation; smaller the jump, greater the phase segregation.

***4.4.3 Conclusions:*** Grain size has marked effects on charge-ordering and other properties of $Nd_{0.5}A_{0.5}MnO_3$ (A = Ca or Sr). The antiferromagnetic transition in $Nd_{0.5}Ca_{0.5}MnO_3$ is observed distinctly only in samples sintered at 1273 K or higher. The sample with a small grain size (sintered at 1173 K) shows evidence for greater ferromagnetic interaction at low temperatures, probably due to phase segregation. The ferromagnetic transition as well as the charge-ordering transition in $Nd_{0.5}Sr_{0.5}MnO_3$ becomes sharper in samples sintered at 1273 K or higher. The sample sintered at 1173 K does not show the AFM-CO transition around 150 K and is ferromagnetic down to low temperatures; the apparent $T_c$-$T_{co}$ gap decreases with the increase in the grain size. The samples sintered at lower temperatures (< 1673 K) show evidence for greater segregation of the AFM and FM domains.

## 4.5 A systematic study of four series of electron-doped rare earth manganates, $Ln_xCa_{1-x}MnO_3$ (Ln=La, Nd, Gd and Y) over the x=0.02-0.25 composition range

***4.5.1 Characterization:*** X-ray powder diffraction patterns showed that all the manganate compositions had an orthorhombic structure (as shown typically in the case of $La_xCa_{1-x}MnO_3$ in Fig. 4.5.1), the lattice parameters varying with the Ln ion in the $Ln_xCa_{1-x}MnO_3$ ($x$ = 0.02-0.25) compositions (Table 4.5.1). The volume increases with increasing Ca concentration as $Mn^{3+}$, which is Jahn-Teller distorted replaces the $Mn^{4+}$ ion. Also, the lattice parameters decrease as we go from La to Y. The $< r_A >$ decreases with increase in $x$ (except when Ln = La) in each series (Fig. 4.5.2a). It is to be noted that the site disorder as measured by the variance $\sigma^2$ [11], also varies with $x$ and the Ln ion. When Ln = La or Nd the $\sigma^2$ is relatively small, varying little with $x$, but when Ln = Gd or Y, $\sigma^2$ becomes appreciable increasing with $x$ as shown in Fig. 4.5.2b. The $\sigma^2$ is maximum and $< r_A >$ smallest in the yttrium system Fig. 4.5.2.

***Table 4.5.1*** *Unit cell dimensions and unit cell volume of* ***(a)*** *$La_xCa_{1-x}MnO_3$.* ***(b)*** *$Nd_xCa_{1-x}MnO_3$.* ***(c)*** *$Gd_xCa_{1-x}MnO_3$.* ***(d)*** *$Y_xCa_{1-x}MnO_3$*

**(a)**

| x | a(Å) | b(Å) | c(Å) | V(Å$^3$) |
|---|---|---|---|---|
| 0.02 | 5.31 | 7.477 | 5.2549 | 208.6346 |
| 0.04 | 5.32 | 7.5005 | 5.2609 | 209.9239 |
| 0.06 | 5.3231 | 7.5162 | 5.2774 | 211.1461 |
| 0.08 | 5.3477 | 7.5681 | 5.3075 | 214.8048 |
| 0.1 | 5.3459 | 7.5018 | 5.3073 | 212.8433 |
| 0.15 | 5.3424 | 7.5207 | 5.3084 | 213.2840 |
| 0.2 | 5.3397 | 7.5392 | 5.3082 | 231.4090 |
| 0.25 | 5.3736 | 7.5546 | 5.3084 | 215.4966 |

(b)

| x | a(Å) | b(Å) | c(Å) | V(Å$^3$) |
|---|---|---|---|---|
| 0.02 | 5.2804 | 7.4640 | 5.2627 | 207.4210 |
| 0.04 | 5.2826 | 7.4729 | 5.2617 | 207.7127 |
| 0.06 | 5.2846 | 7.4847 | 5.2305 | 206.8853 |
| 0.08 | 5.2959 | 7.4864 | 5.1817 | 205.4400 |
| 0.1 | 5.304 | 7.4982 | 5.2415 | 208.4568 |
| 0.15 | 5.3139 | 7.5189 | 5.2783 | 210.8928 |
| 0.2 | 5.3207 | 7.5188 | 5.2827 | 211.3359 |
| 0.25 | 5.3277 | 7.5462 | 5.2803 | 212.2886 |

(c)

| x | a(Å) | b(Å) | c(Å) | V(Å$^3$) |
|---|---|---|---|---|
| 0.02 | 5.2808 | 7.4617 | 5.2363 | 206.32983 |
| 0.04 | 5.2866 | 7.4879 | 5.2499 | 207.82009 |
| 0.06 | 5.2874 | 7.4852 | 5.24 | 207.38477 |
| 0.08 | 5.2976 | 7.4807 | 5.2403 | 207.67181 |
| 0.1 | 5.3116 | 7.5047 | 5.2618 | 209.74568 |
| 0.15 | 5.3389 | 7.508 | 5.2813 | 211.69806 |
| 0.2 | 5.3336 | 7.4972 | 5.2915 | 211.59156 |
| 0.25 | 5.3314 | 7.5285 | 5.2962 | 212.57594 |

(d)

| x | a(Å) | b(Å) | c(Å) | V(Å$^3$) |
|---|---|---|---|---|
| 0.02 | 5.2764 | 7.4638 | 5.2349 | 206.1608 |
| 0.04 | 5.2799 | 7.47 | 5.227 | 206.1573 |
| 0.06 | 5.2791 | 7.4739 | 5.2292 | 206.3252 |
| 0.08 | 5.2827 | 7.4834 | 5.2428 | 207.2613 |
| 0.1 | 5.2874 | 7.4846 | 5.2748 | 208.7453 |
| 0.15 | 5.2876 | 7.4921 | 5.2771 | 209.0535 |
| 0.2 | 5.3297 | 7.4811 | 5.2975 | 211.2220 |
| 0.25 | 5.345 | 7.458 | 5.2971 | 211.1584 |

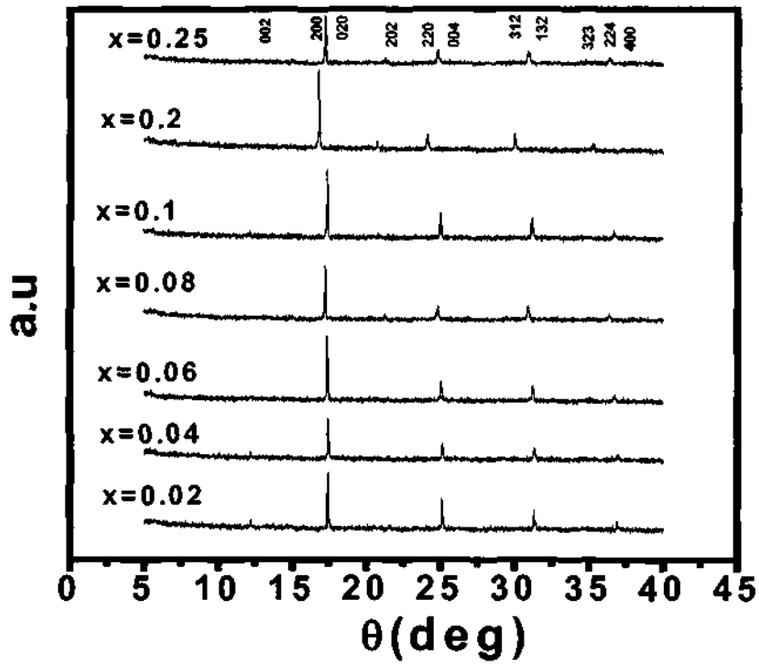


*Fig.4.5.1 X-ray diffraction patterns of $La_xCa_{1-x}MnO_3$*

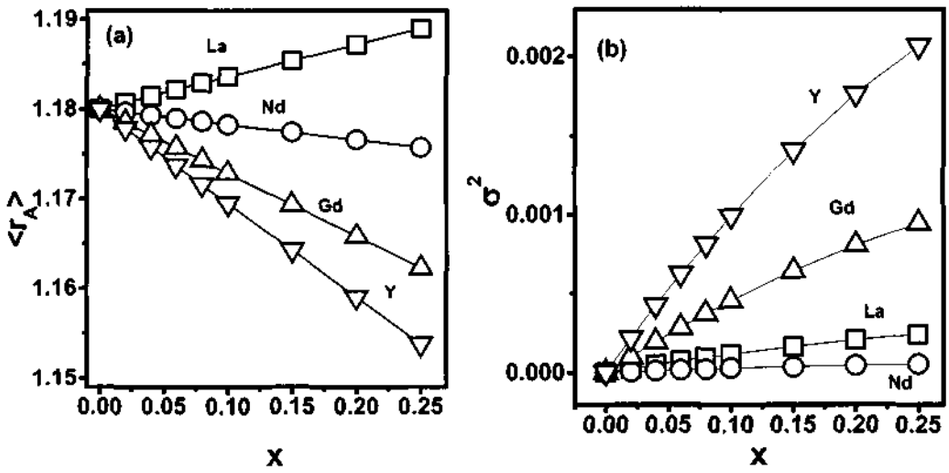


*Fig. 4.5.2 (a) Variation of $<r_A>$ with concentration in $Ln_xCa_{1-x}MnO_3$. (b) Variation of $\sigma^2$ with concentration in $Ln_xCa_{1-x}MnO_3$.*

***4.5.2 Magnetization data:*** In figures 4.5.3 the temperature variation of magnetization in several compositions of $Ln_xCa_{1-x}MnO_3$ with Ln = La, Nd, Gd and Y is shown. The compositions with $x \leq 0.1$ in all the four series of manganates exhibit a marked increase in magnetization as in a ferromagnet around 100-120 K ($T_M$). These materials are, however, not real ferromagnets and show only small values of saturation magnetization even at 9000 gauss. At low $x$ values ($x \leq 0.1$), the magnetization increases with $x$ or the electron concentration and then decreases sharply. The maximum value of magnetization occurs at $x$ = 0.08, 0.08, 0.10 and 0.15 ($x_{max}$) for Ln = La, Nd, Gd and Y respectively.

Accordingly, plots of $\mu_\beta$ versus $x$ show maxima at increasing values of $x$ as the average radius of the A-site cation, $<r_A>$, decreases, the maximum value of $\mu_\beta$ being found when Ln = Gd (Fig. 4.5.4). The increase in $x_{max}$ with decrease in $<r_A>$ can arise from phase separation due to presence of significant FM fractions in the

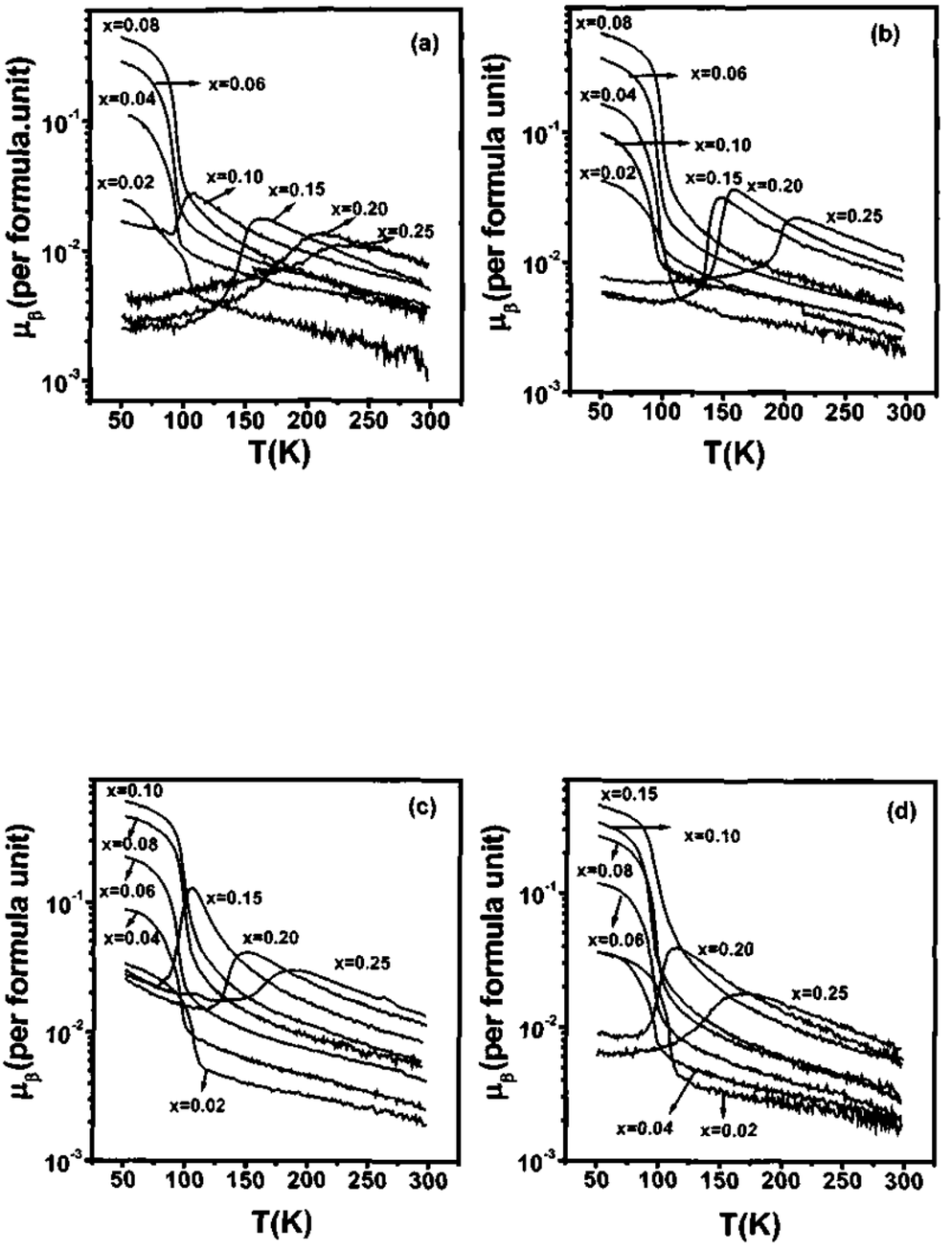


*Fig. 4.5.3 Temperature variation of magnetic moments of **(a)** $La_xCa_{1-x}MnO_3$. **(b)** $Nd_xCa_{1-x}MnO_3$. **(c)** $Gd_xCa_{1-x}MnO_3$. **(d)** $Y_xCa_{1-x}MnO_3$.*

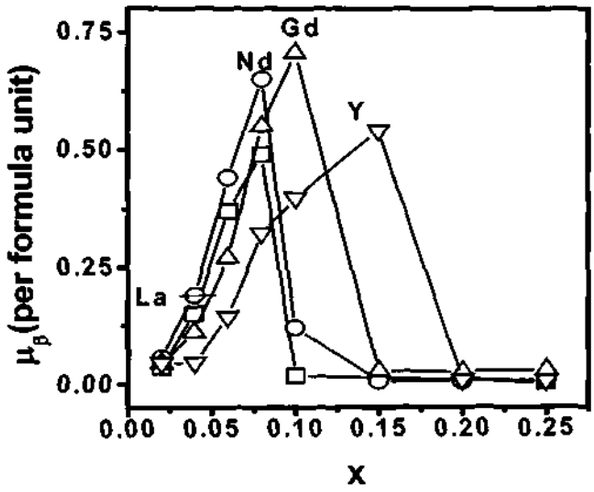


*Fig. 4.5.4 Variation of $\mu_\beta$ with composition at 50 K for $Ln_xCa_{1-x}MnO_3$.*

AFM matrix. The largest ferromagnetic fraction occurs around $x_{max}$ when the magnetization is maximum. In the composition range $x > 0.15$ ($x > x_{max}$), the ferromagnetic fraction is small, with the concentration decreasing with increasing $x$. We would therefore expect phase separation to be prominent up to $x_{max}$. Considering that ferromagnetism itself would be favored by large $\langle r_A \rangle$, the observed trend in Fig. 4.5.4 can be taken to reflect an increase in the width of the phase separation regime. Interestingly, the $x_{max}$ is highest when Ln = Y. This is likely to be because of the large cation size disorder (Fig. 4.5.1b). This observation indirectly suggests that the phase separation in these manganate compositions is induced by size disorder, the separation regime increasing with $\sigma^2$.

After the magnetization attains a maximum value at $x_{max}$, we not only see a sudden drop in magnetization, but also evidence for a competition between ferromagnetism and antiferromagnetism. This competition gives rise to a peak in the magnetization-temperature curves (see Fig. 4.5.3).

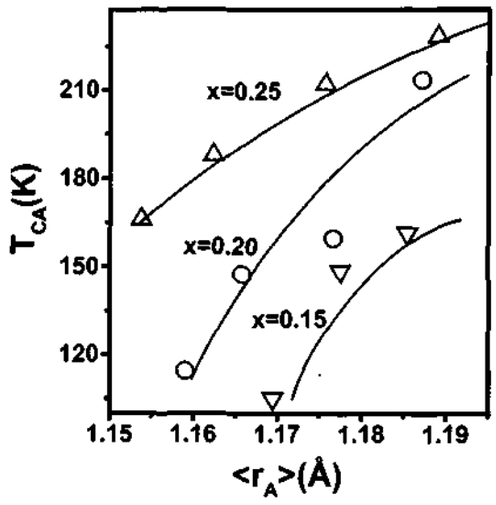


***Fig. 4.5.5*** *Variation of $T_{CA}$ with <$r_A$> at a given Ca concentration in $Ln_xCa_{1-x}MnO_3$.*

These peaks are reminiscent of the magnetization peaks found in charge-ordered systems such as $Nd_{0.5}Ca_{0.5}MnO_3$ and $Pr_{0.6}Ca_{0.4}MnO_3$ [13,14]. The temperature corresponding to the peak maximum ($T_{CA}$) increases with increasing $x$ in the $x$ = 0.1-0.25 composition range in all the four series of manganates. The peak occurs at $x$~0.1 when Ln = La, at 0.15 for Nd and Gd and at 0.2 for Y. As shown in Fig. 4.5.5, $T_{CA}$ increases with <$r_A$>. It has been shown that the temperature corresponding to the magnetic susceptibility anomaly due to charge-ordering in electron- doped manganate compositions, increases up to $x$ = 0.3 and then decreases slightly in the $x$ = 0.3-0.5 composition range [14,15]. The effect of <$r_A$> in negligible when $x \geq 0.3$.

***4.5.3 Resistivity data:*** The changes in the magnetization of $Ln_xCa_{1-x}MnO_3$ with composition and temperature are reflected in the electrical resistivities [16] as shown in figures 4.5.6.

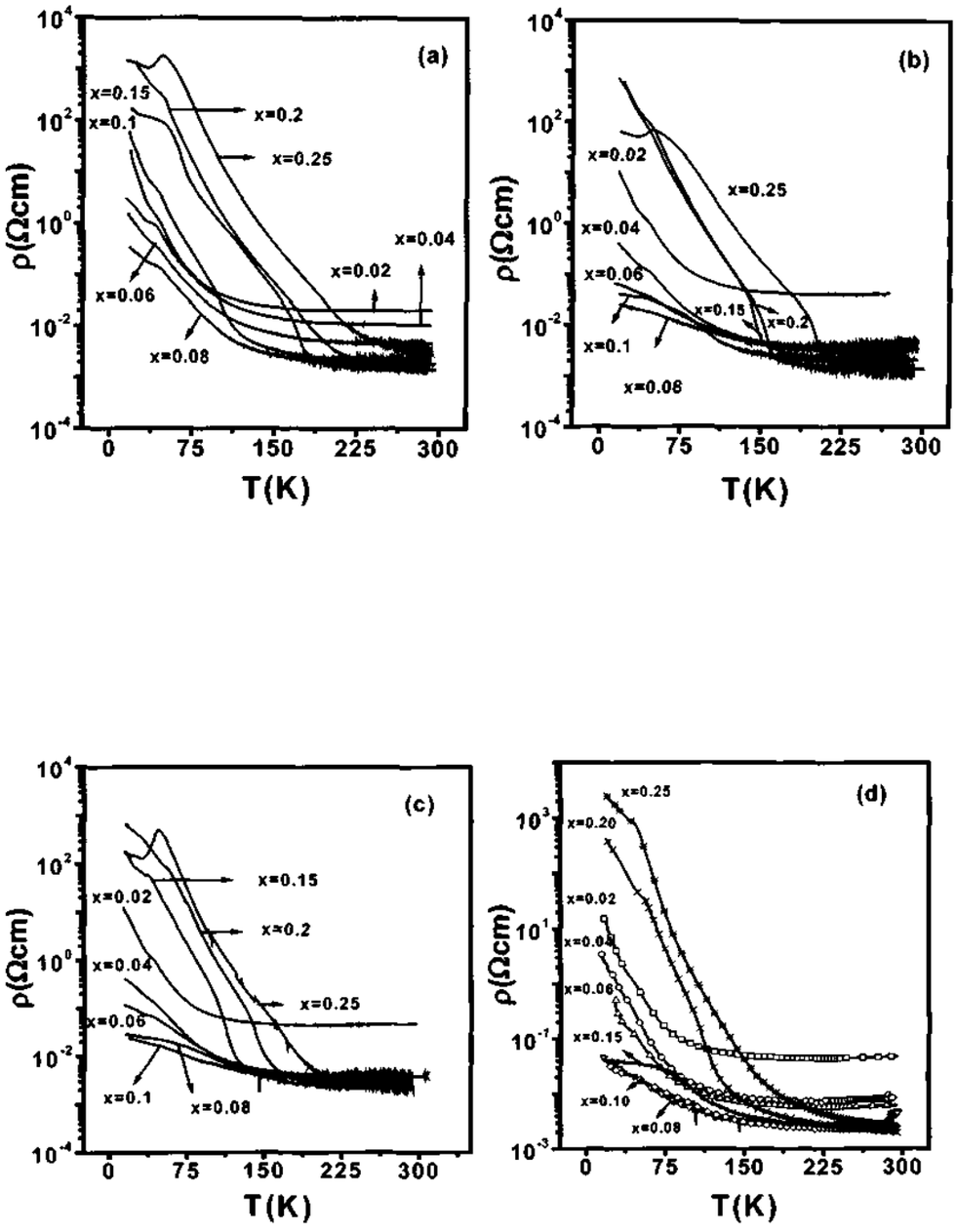


***Fig. 4.5.6*** *Temperature variation of electrical resistivity of* $Ln_xCa_{1-x}MnO_3$. ***(a)*** $La_xCa_{1-x}MnO_3$. ***(b)*** $Nd_xCa_{1-x}MnO_3$. ***(c)*** $Gd_xCa_{1-x}MnO_3$. ***(d)*** $Y_xCa_{1-x}MnO_3$.

Thus, all the four series of manganates with $x < x_{max}$ show low resistivities from 300 K down to 100-120 K ($T_M$), independent of $<r_A>$. The activation energies for conduction are rather small (25-30 meV) as reported by other workers [17,18]. In this low dopant concentration regime ($x < x_{max}$), the resistivity increases below $T_M$, the change possibly representing a semi-metal-insulator transition. The low-temperature resistivity (at $T < T_M$) increases with the decrease in electron concentration or x in this composition regime, paralleling the magnetization data in agreement with the earlier literature [16]. The resistivity also decreases with decrease in $<r_A>$ in the $Ln_xCa_{1-x}MnO_3$ series showing a minimum for Ln = Gd ($<r_A>$~1.179 Å) where the magnetization is maximum. Such a correspondence between the magnetization and the resistivity data is interesting and may have its origin in the phase separation resulting in percolative conduction.

The resistivity behavior drastically changes when $x > x_{max}$ in the four series of manganates. In this composition regime, the resistivity increases sharply as can be seen from figures 4.5.6. The increase in resistivity occurs around the same temperature as the peak in the magnetization-temperature curves ($T_{CA}$). The occurrence of a sharp change in resistivity at the same temperature as the magnetization peak suggests the occurrence of charge-ordering associated with antiferromagnetism. This transition temperature may, therefore, be considered to represent the onset of C-type antiferromagnetism.

***4.5.4 Magnetic hysteresis:*** The $x < x_{max}$ compositions in $Ln_xCa_{1-x}MnO_3$ exhibit magnetic hysteresis at $T < T_M$ (Fig. 4.5.7). The hysteresis loops throw light on the nature of phase separation. In the multilayers of spin valve and permalloy materials

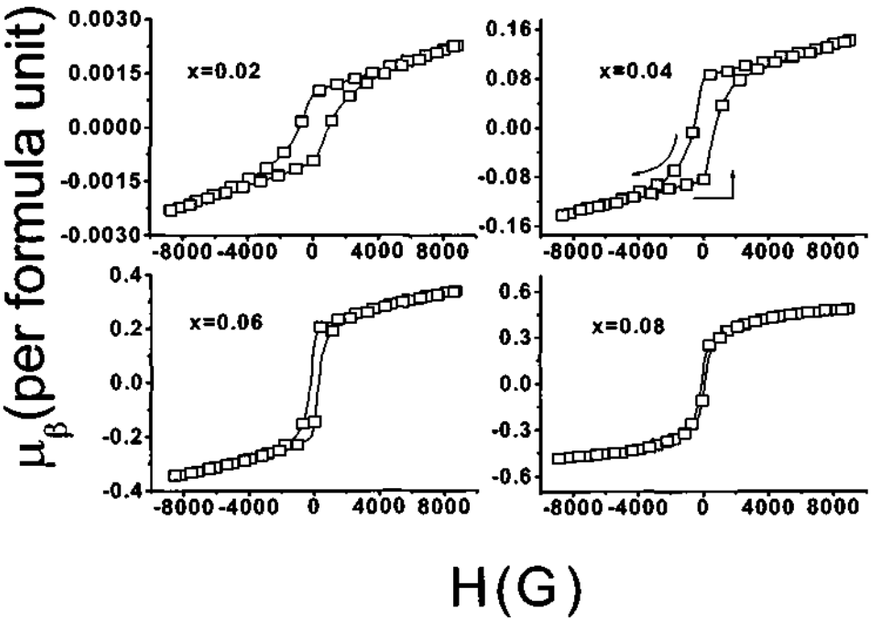


*Fig. 4.5.7 Magnetic hysteric loopd in $La_xCa_{1-x}MnO_3$ at 50 K.*

[19-21] wherein the ferromagnetic layers are coupled to antiferromagnetic layers, the hysteresis loops reflect the extent of exchange coupling between the ferromagnetic and the antiferromagnetic layers. The coercivity of the ferromagnetic layer increases due the coupling with an antiferromagnetic layer. Since the phase-separated compositions of the manganates contain both the ferromagnetic and the antiferromagnetic regions, they would be expected to show similar behavior. We see from Fig. 4.5.7, that the hysteresis loops are broad at small $x$ values ($x \leq 0.04$) and the width decreases as $x$ reaches $x_{max}$. When the system is subjected to magnetization reversal process, the interfacial spins between antiferromagnetic and ferromagnetic domains rotate with the ferromagnetic domain but experience an increased rotational drag due to the antiferromagnetic domains leading to broadening of the hysteresis loops. As the electron concentration or $x$ increases, the

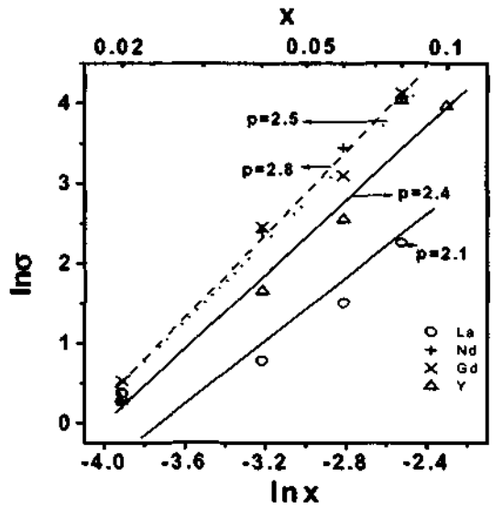


*Fig. 4.5.8 conductivity data of $Ln_xCa_{1-x}MnO_3$ fitted to a scaling law $\sigma \propto |x_c-x|^p$*

ferromagnetic character (domain/cluster size) increases, thereby reducing the drag substantially and causing a decrease in the width as expected. It must be recalled that the ferromagnetic fraction reaches a maximum at $x_{max}$. The width of the hysteresis loop for a given $x$ value increases with the decrease in the radius of the Ln (or $<r_A>$), reflecting the effect of phase separation.

The ferromagnetic hysteresis loops are symmetric, indicating two equivalent directions of magnetization. On the other hand, when a ferromagnetic /antiferromagnetic material is cooled in an external magnetic field (as in this case for obtaining M versus T plots) below the Neel temperature (< 100 K), the loop is shifted from zero due to the exchange bias effect. The small differences in the coercive fields (Table 4.5.2) seen for the phase-separated samples may be due to the pinning of a small fraction of ferromagnetic interfacial spins to the antiferromagnetic domains. The pinned spins do not rotate in an external field as they are coupled leading to exchange biasing.

Magnetization reversal in a ferromagnetic system occurs through rotation of spins, and via domain nucleation and growth. An examination of the hysteresis loops shows that magnetization drops from a maximum value to zero sharply compared to the increase from zero to the maximum value. This suggests that for $0.02 < x \leq 0.06$, one mechanism dominates over the other in a particular region of magnetization reversal process, bringing about an asymmetry in the hysteresis loops. Thus, it is much harder to magnetize the $0.02 < x \leq 0.06$ compositions wherein the ferromagnetic clusters are embedded in a antiferromagnetic matrix.

***Table 4.5.2*** *Coercivity ($H_c$ and $-H_c$ in gauss) of $Ln_xCa_{1-x}MnO_3$ obtained from hysteresis measurement at 50 K.*

| x | La | | Nd | | Gd | | Y | |
|---|---|---|---|---|---|---|---|---|
| | $H_c$ | $-H_c$ | $H_c$ | $-H_c$ | $H_c$ | $-H_c$ | $H_c$ | $-H_c$ |
| 0.02 | 966 | 849 | 454 | 340 | 508 | 395 | 429 | 338 |
| 0.04 | 706 | 604 | 454 | 449 | 580 | 572 | 865 | 589 |
| 0.06 | 300 | 203 | 215 | 124 | 373 | 279 | 579 | 473 |
| 0.08 | 94 | 100 | 114 | 32 | 154 | 62 | 344 | 247 |
| 0.10 | - | - | 870 | 776 | 154 | 62 | 322 | 220 |
| 0.15 | - | - | - | - | - | - | 310 | 208 |

***4.5.5 Percolation:*** It was mentioned earlier that the conducting mechanism in the phase-separated regime maybe percolative. We have employed the scaling law, $\sigma \propto |x_c - x|^p$, to treat the resistivity data in the x = 0.02-0.1 composition regime. We show $\ln\sigma$ -$\ln x$ plots at 50 K from the series of manganates studied by us in Fig. 4.5.8. The value of the exponent p is between 2.1 and 2.8 at 50 K. Percolative conduction becomes less dominant as the temperature approaches $T_M$ or $x$ reaches $x_{max}$ (0.1-

0.15). This is understandable since antiferromagnetism is the main interaction when $x > x_{max}$ and $T > T_M$, leading to lesser phase separation and a more homogeneous antiferromagnetic phase.

***4.5.6 Conclusions:*** The present study of the four series of electron-doped manganates, $Ln_xCa_{1-x}MnO_3$ (Ln = La, Nd, Gd and Y), over a wide range of compositions ($x$ = 0.02-0.25) has been useful in understanding the evolution of various phenomena. Thus, these materials which show ferromagnetic-like behavior at $T<T_M$ upto a value of $x$ ($x_{max}$), become antiferromagnetic with charge ordering at $T_{CA}$ for $x > x_{max}$. The values of $x_{max}$ and $T_{CA}$ depend on the average radius of A-site cation ($<r_A>$), the former being related to the phase separation and site disorder ($\sigma^2$). Phase separation is favored at low temperatures ($T < T_M$) by small $x$ ($< x_{max}$) and small $<r_A>$ (or large $\sigma^2$). The AFM CO transition temperature, $T_{CA}$, on the other hand, increases with increasing $x$ and $<r_A>$ and does not vary significantly with $<r_A>$ when $x \geq 0.3$. All these materials show low resistivity at $T > T_M$ when $x \leq x_{max}$, but show a sharp increase in resistivity at $T_{CA}$ when $x > x_{max}$, due to charge ordering. When $x < x_{max}$ and $T < T_M$, conduction appears to be percolative. Since the above features are found in all the four series of manganates covering a wide range of $<r_A>$, they can be taken to be intrinsic to the electron doped compositions of the rare earth manganates. Thus, the present study clearly identifies the phase-separated regime with percolative conduction ($x$ = 0.02-$x_{max}$) and the charge-ordered antiferromagnetic regime with $x_{max}$ in the ~ 0.1-0.15 range. The percolative regime increases with size disorder or decrease in $<r_A>$.

## 4.6 Investigation of the Electrical and Magnetic properties of Electron-doped Ruddlesden-Popper phases, $CaO(Pr_{0.08}Ca_{0.92}MnO_3)_n$ (n=1,2,3 and ∞)

***4.6.1 Characterization:*** X-ray diffraction analysis of these materials confirmed that the samples were mono-phasic (Fig. 4.6.1). The lattice parameters for n = 1 were calculated based on symmetry group that was reported for $Ca_2MnO_4$ ($I4_1/acd$). For n = 2, *Cmcm* space group was employed for estimating the lattice parameters [22], whereas, for n = 3 P*bca* space group was chosen. From Table 4.6.1, one can clearly see a systematic increase in the lattice parameters as n increases from 1 to ∞. The lattice constant, c, of these samples showed a dramatic variance compared to a and b. The systematic increase in c, with increasing n is clearly due to the addition of perovskite layers between the rock-salt-like CaO layers. On the other hand, a substantial difference in the lattice constants of a and b as compared to the lattice constants of the parent Ca-Mn-O RP phases could be attributed to the presence of larger $Mn^{3+}$ ions in the perovskite ab-plane [23]. The amount of $Mn^{3+}$ determined by iodometric titrations is consistent with the expected value within experimental errors (Table 4.6.1).

***Table 4.6.1*** *Space group, unit cell parameters and the percentage of $Mn^{3+}$ determined from iodometric titration across the series $CaO(Pr_{0.08}Ca_{0.92}MnO_3)_n$ (n=1,2,3 and ∞).*

| *n* | Space group | *a*(Å) | *b*(Å) | c(Å) | $Mn^{3+}$ |
|---|---|---|---|---|---|
| 1 | $I4_1/acd$ | 5.2231 | 5.2231 | 24.0503 | 8%(±2%) |
| 2 | *Cmcm* | 5.2407 | 5.2817 | 26.7183 | 7%(±2%) |
| 3 | *Pbca* | 5.2494 | 5.2831 | 27.0095 | 8%(±2%) |
| ∞ | *Pbca* | 5.2819 | 5.3059 | 7.4791 | 8%(±2%) |

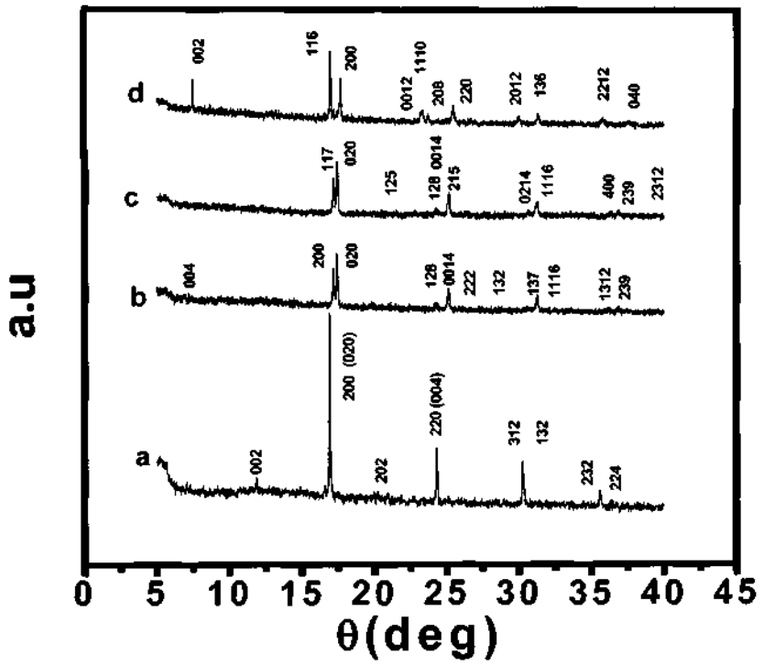


***Fig. 4.6.1*** *X-ray diffraction patterns of $CaO(Pr_{0.08}Ca_{0.92}MnO_3)_n$* ***(a)*** *n=∞;* ***(b)*** *n=3;* ***(c)*** *n=2 and* ***(d)*** *n=1.*

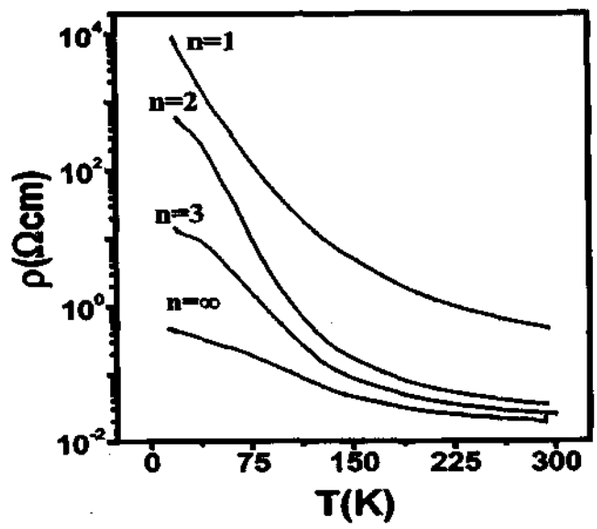


***Fig. 4.6.2*** *Temperature variation electrical resistivity of $CaO(Pr_{0.08}Ca_{0.92}MnO_3)_n$ for n=1,2,3 and ∞.*

***4.6.2 Resistivity and magnetization data:*** The temperature-dependent electrical resistivity of $CaO(Pr_{0.08}Ca_{0.92}MnO_3)_n$ ($n$=1,2,3 and ∞) is shown in Fig.4.6.2. As can be seen, the electron-doped RP phases did not show an I-M transition. The resistivity variation indicates that the samples are semiconducting with no anomalous features in the entire temperature range. It is also interesting to note that the resistivities of the electron-doped samples are three orders of magnitude smaller in comparison with those of RP phases of the calcium manganates although the trend in resistivities across the series as expected [23,24].

The inverse susceptibility after correcting for the paramagnetic contributions due to $Pr^{3+}$ (p= $g\sqrt{J(J+1)}$ = 3.58) are shown in Fig. 4.6.3. From the Curie-Weiss law, one expects

$$\frac{1}{\chi} = \frac{3k_B(T-\theta)}{N_a g^2 \mu_B^2 S(S+1)} \qquad (1)$$

where $k_B$ is Boltzmann's constant, θ the Weiss temperature, $N_a$ Avogadro's number, $\mu_B$ the Bohr magneton, and S the spin. The resulting values of the effective magnetic moment ($\mu_B$) from the fits are 2.90, 2.85, 2.80 and 2.55 for $n$ = 1, 2, 3, and ∞, respectively. The expected value for the moment is 3.08 $\mu_B$ for the measured Mn valence. The respective Weiss temperatures are –58 K, -44 K, -37 K, and 72 K. It is notable that the Weiss temperature for the low-dimensional materials is negative while that of the pseudo-cubic system is positive. The observation of large negative Weiss constants is common to manganese oxides and in particular to the undoped RP series in the Ca-Mn-O manganates [23].

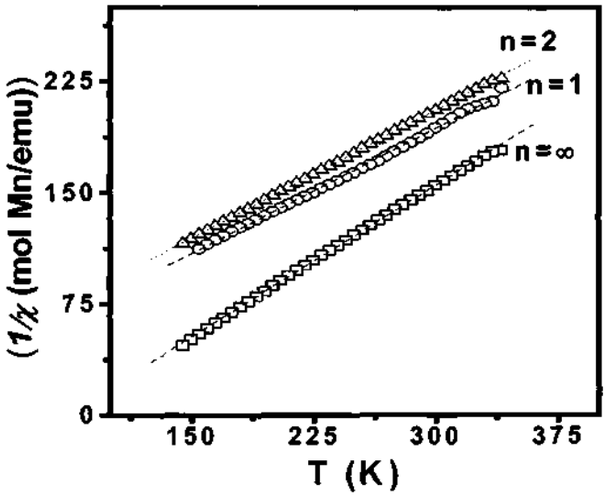


***Fig. 4.6.3*** *Inverse magnetic susceptibility of $CaO(Pr_{0.08}Ca_{0.92}MnO_3)_n$ for n=1,2 and ∞ as a function of temperature in the range 150-350K. Plot for the n=3 composition is similar to the n=2 and hence was omitted for clarity.*

The low-temperature magnetization behavior of the samples is shown in Fig. 4.6.4. A remarkable result is the onset of ferromagnetic-like ordering at 100 K, irrespective of dimensionality. This is in sharp contrast to nearly all other systems, which generally demonstrate a strong dependence of the magnetic ordering temperature on dimensionality, such as in the RP phases of Ca-Mn-O manganates [23]. The $n$=1 compound has a rather peculiar looking temperature dependence, being nearly linear in T. This effect becomes less pronounced with increasing dimensionality.

The low-temperature magnetization loops (Fig. 4.6.5) display a non-monotonic dependence on dimensionality, with the $n$=2 phase having the least magnetization. The exact contribution to the high-field susceptibility at low temperature from the $Pr^{3+}$ ion

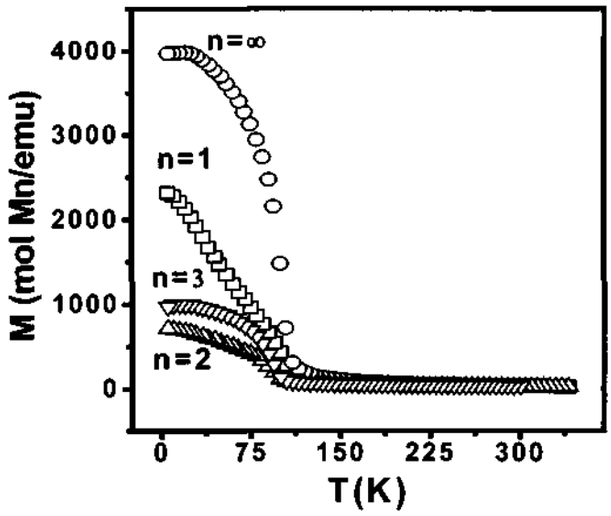


*Fig. 4.6.4 Temperature dependent magnetization of $CaO(Pr_{0.08}Ca_{0.92}MnO_3)_n$ for n=1,2,3 and ∞.*

is difficult to assess – one needs to know the exact crystal-field splitting to be precise; however, it is not unreasonable to attribute nearly all of the high-field susceptibility to the $Pr^{3+}$ ion. This behavior may also be the result of a slight variation in the $Mn^{3+}$, as the magnetic properties are very sensitive to electron doping in this range.

One way to understand these observations is to invoke "ferromagnetic droplets" as suggested in [25,26] for $Ln_{1-x}A_xMnO_3$, where Ln is a rare earth and A is an alkaline earth metal. It is suggested that the ferromagnetic clusters form around $Mn^{3+}$ ions and the existence of such clusters in the $Ln_xCa_{1-x}MnO_3$ compositions with $x$~0.1[27]. The calcium manganate RP phases show effectively a temperature-independent susceptibility with a small indication of magnetism occurring near 100 K, in contrast to the electron-doped compounds studied here. Presumably the presence of $Mn^{3+}$ nucleates the ferromagnetic interactions, giving rise to a reasonable magnetic susceptibility.

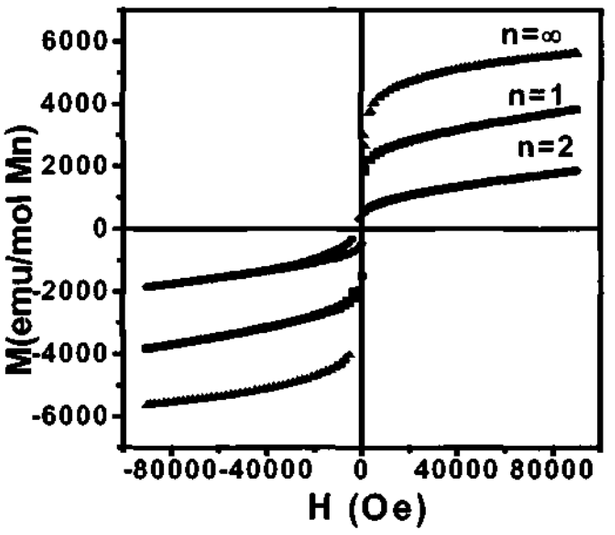


***Fig. 4.6.5*** *Field dependent magnetization of $CaO(Pr_{0.08}Ca_{0.92}MnO_3)_n$ for n=1,2 and ∞ at 5K. Plot of the n=3 was omitted for clarity.*

The unusual temperature dependence of the magnetization for $n$=1 can be attributed to the difficulty in maintaining ferromagnetism in low-dimensional systems. Perhaps the non-linear dependence of the "ferromagnetic" moment and Weiss temperature on dimensionality can be attributed to small variations in the Mn valence. That is, if the $Mn^{3+}$ is truly what gives rise to the magnetization, small changes will have a large effect on the magnetic properties.

The "droplet" model is also consistent with electron transport measurements; i.e. the resistivity of the $n$=1 compound is significantly larger than that of $n$=2 even though its "ferromagnetic" magnetization is larger. Since the number of the droplets, which are presumably metallic, is well below the percolation threshold, their contribution to the conductivity is minimal. Thus, the $n$=2 compound will have a higher conductivity than that of $n$=1 due to increased dimensionality.

***4.6.3 Conclusions:*** We prepared single phase Ruddlesden-Popper compositions with the formula $CaO(Pr_{0.08}Ca_{0.92}MnO_3)_n$ ($n$=1,2,3 and $\infty$) by a gel-pyrolysis method. The electron-doped RP series bear structural resemblance to their parent phases, however, dramatic differences are seen in their electronic properties. Notably, the electrical resistivity of the doped series show three orders of magnitude reduction compared to the undoped series. The magnetization data also displays an unusual behavior which can be explained invoking a 'ferromagnetic-cluster' model. The cluster size and interaction are observed to depend on the number of perovskite layers. Anomalous deviation in the magnetization of the $n$=1 phase has been attributed to the difficulties associated with maintaining ferromagnetic order in two-dimensional system.

## 4.7 Electronic phase separation in the rare earth manganates, $(La_{1-x}Ln_x)_{0.7}Ca_{0.3}MnO_3$ (Ln = Nd, Gd and Y)

***4.7.1 Characterization:*** All the compositions were fitted to an orthorhombic unit cell with P*nma* space group. The X-ray diffraction patterns of the members of the $(La_{1-x}Nd_x)_{0.7}Ca_{0.3}MnO_3$ series are shown in Fig. 4.7.1 The unit cell dimensions of $(La_{1-x}Ln_x)_{0.7}Ca_{0.3}MnO_3$ decrease with the increase in $x$ in all the three series of manganates (Table 4.7.1), with a corresponding decrease in the unit cell volume as expected when a large cation is replaced by smaller cation. The dependence of the unit cell dimensions and volume for the three different compositions parallels the dependence of the average radius of the A-site cations, $< r_A >$, on $x$. Thus a plot of the unit cell volume of the three series of manganates against $< r_A >$ is linear as shown in the Fig. 4.7.2.

***Table 4.7.1*** *Unit cell dimensions of* $(La_{1-x}Ln_x)_{0.7}Ca_{0.3}MnO_3$ ***(a)*** *Ln=Nd;* ***(b)*** *Ln=Gd;* ***(c)*** *Ln=Y.*

**(a)**

| *x* | *a*(Å) | *b*(Å) | *c*(Å) | Vol. (Å$^3$) |
|---|---|---|---|---|
| 0 | 5.4800 | 7.7107 | 5.4549 | 230.4948 |
| 0.2 | 5.4654 | 7.7185 | 5.4441 | 229.6978 |
| 0.4 | 5.4519 | 7.7111 | 5.4360 | 228.5302 |
| 0.5 | 5.4647 | 7.6967 | 5.4310 | 228.4287 |
| 0.6 | 5.4704 | 7.6889 | 5.4276 | 228.2922 |
| 0.7 | 5.4601 | 7.6815 | 5.4265 | 227.5970 |
| 0.8 | 5.4527 | 7.6680 | 5.4150 | 226.4082 |
| 0.9 | 5.4684 | 7.6677 | 5.4140 | 227.0093 |

(b)

| x | a(Å) | b(Å) | c(Å) | Vol. (Å$^3$) |
|---|---|---|---|---|
| 0.1 | 5.4653 | 7.7153 | 5.4597 | 230.2161 |
| 0.3 | 5.467 | 7.6859 | 5.4338 | 228.3218 |
| 0.4 | 5.4666 | 7.6678 | 5.4241 | 227.3609 |
| 0.5 | 5.4686 | 7.6441 | 5.4088 | 226.1015 |
| 0.6 | 5.4812 | 7.625 | 5.3972 | 225.5714 |
| 0.7 | 5.4871 | 7.5967 | 5.3884 | 224.6093 |
| 0.8 | 5.5061 | 7.5714 | 5.3903 | 224.7156 |

(c)

| x | a(Å) | b(Å) | c(Å) | Vol. (Å$^3$) |
|---|---|---|---|---|
| 0.1 | 5.4619 | 7.7071 | 5.4447 | 229.1969 |
| 0.2 | 5.4594 | 7.7 | 5.4348 | 228.4648 |
| 0.26 | 5.4446 | 7.7049 | 5.4204 | 227.3863 |
| 0.4 | 5.4496 | 7.7001 | 5.4128 | 227.1344 |
| 0.5 | 5.4424 | 7.6922 | 5.4067 | 226.3463 |
| 0.7 | 5.3814 | 7.6742 | 5.3762 | 222.0177 |
| 0.9 | 5.4229 | 7.6719 | 5.3494 | 222.5562 |

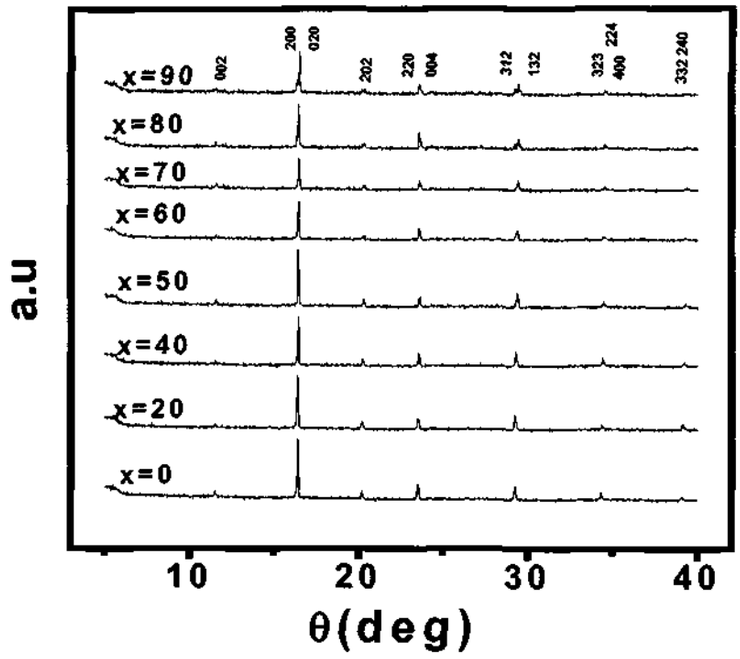


*Fig. 4.7.1 X-ray diffraction pattern of $(La_{1-x}Nd_x)_{0.7}Ca_{0.3}MnO_3$ sintered at 1653 K.*

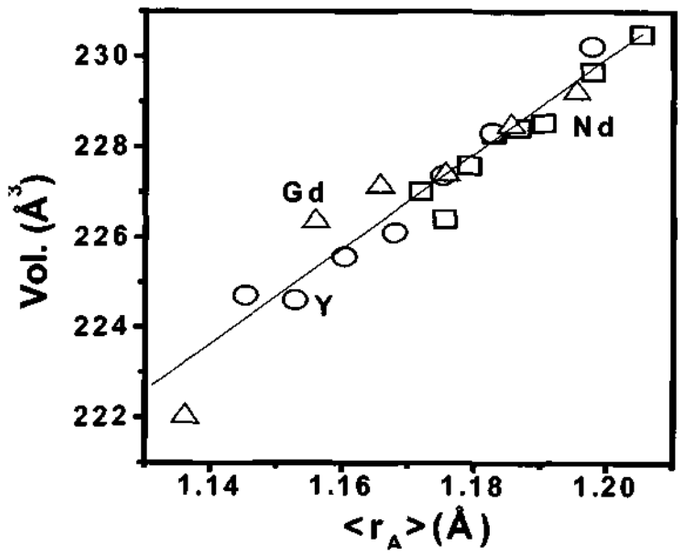


*Fig. 4.7.2 Variation of unit cell volume of $(La_{1-x}Ln_x)_{0.7}Ca_{0.3}MnO_3$ with $\langle r_A \rangle$.*

***4.7.2 Magnetization data:*** In Fig.4.7.3a, we show the results of magnetic measurements of the $(La_{1-x}Nd_x)_{0.7}Ca_{0.3}MnO_3$ series to show how the magnetic moment ($\mu_\beta$) is sensitive to the substitution of the smaller $Nd^{3+}$ cation in place of $La^{3+}$. We see a clear FM transition down to $x = 0.5$ with a saturation magnetic moment close to $3\mu_\beta$. The ferromagnetic Curie temperature, $T_c$, shifts to lower temperatures with increase in $x$. We fail to see magnetic saturation in compositions with $x \geq 0.6$ and instead, the maximum value of $\mu_\beta$ is far less than three at low temperatures. We designate the composition up to which ferromagnetism occurs as the critical composition $x_c$. The compositions with $x > x_c$ show a gradual, definitive increase in the magnetization or $\mu_\beta$ at a temperature $T_M$, the $T_M$ value decreasing with increasing $x$. It is possible that $T_M$ represents the onset of canted antiferromagnetism (CAF). In $(La_{1-x}Gd_x)_{0.7}Ca_{0.3}MnO_3$, ferromagnetism is observed up to $x = 0.3$. The $T_c$ decreases with increase in $x$ in the composition range $0.0 \leq x \leq 0.3$. For $x > 0.3$, we observe a gradual increase in $\mu_\beta$ value at low temperature around $T_M$, with the value of $T_M$ decreasing with increase in $x$. Note that the value of $x_c$ (~0.3) in the Gd series is considerably lower than that in the Nd series where it was 0.6, showing that $x_c$ decreases with the decrease in the average radius of the A-site cation, $< r_A >$. The results of the $(La_{1-x}Gd_x)_{0.7}Ca_{0.3}MnO_3$ series of manganates (Fig.4.7.3b) obtained by us agree with those reported for the $x$ = 0.0-0.25 compositions by Terashita and Neumeier [28].

In $(La_{1-x}Y_x)_{0.7}Ca_{0.3}MnO_3$, ferromagnetism is seen only for compositions with $x \leq 0.2$, the $T_c$ decreasing with increase in $x$. Compositions with $x > 0.2$, show a

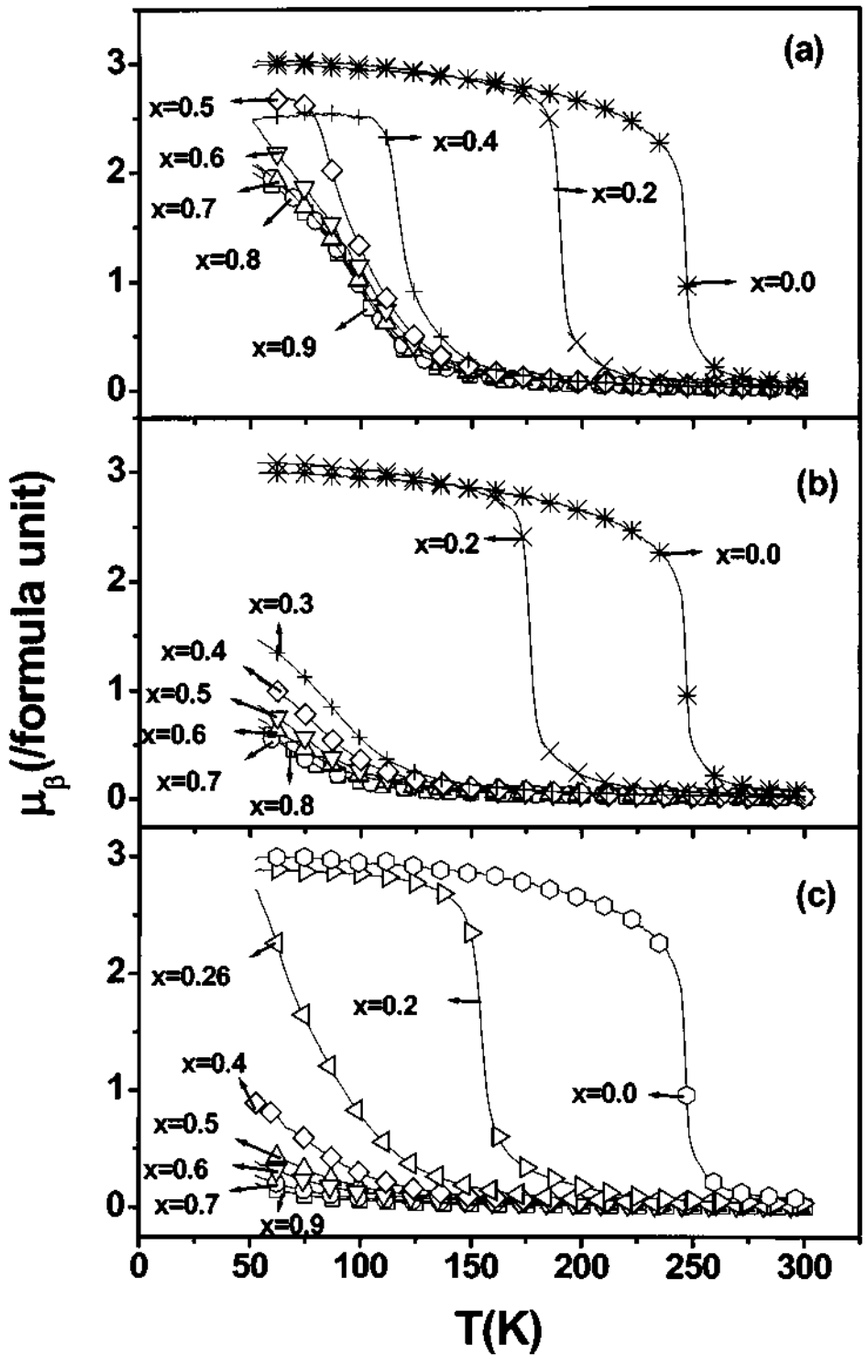


*Fig. 4.7.3 Temperature variation of $\mu_\beta$ in* **(a)** $(La_{1-x}Nd_x)_{0.7}Ca_{0.3}MnO_3$, **(b)** $(La_{1-}Gd_x)_{0.7}Ca_{0.3}MnO_3$ *and* **(c)** $(La_{1-x}Y_x)_{0.7}Ca_{0.3}MnO_3$.

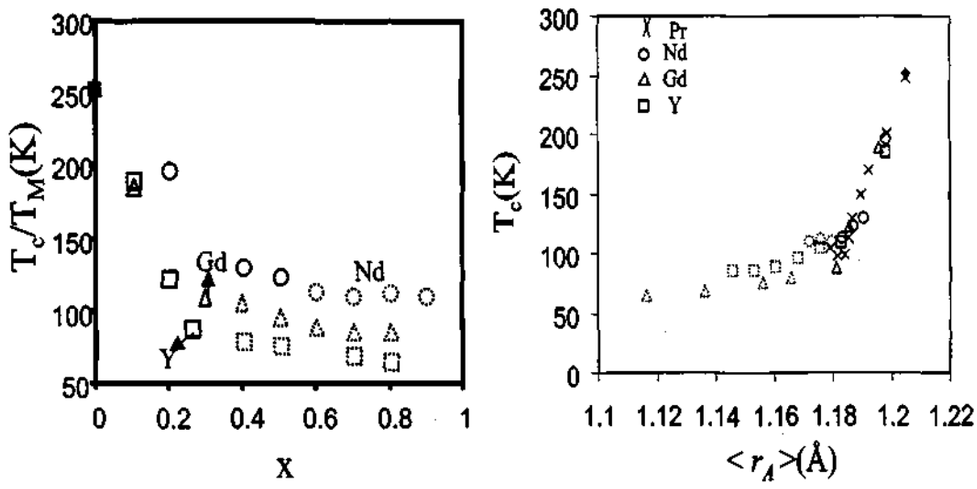


*Fig. 4.7.4 (a) Variation of $T_c$ with x of $(La_{1-x}Ln_x)_{0.7}Ca_{0.3}MnO_3$. Solid symbols represent real $T_c$ and broken symbols represent $T_M$. (b) Variation of $T_c$ with $< r_A >$ (Å) for $(La_{1-x}Ln_x)_{0.7}Ca_{0.3}MnO_3$(x=0 data is shown as ♦). $(La_{1-x}Ln_x)_{0.7}Ca_{0.3}MnO_3$ data taken from ref. 8.*

gradual increase in the $\mu_\beta$ value below $T_M$ and the $T_M$ decreases with increase in $x$ (Fig. 4.7.3c).

Thus, the $x_c$ value in $(La_{1-x}Ln_x)_{0.7}Ca_{0.3}MnO_3$ is 0.75, 0.6, 0.3 and 0.2 for Ln = Pr, Nd, Gd and Y respectively, showing a sensitive dependence of $x_c$ on $< r_A >$. The magnetization data of $(La_{1-x}Ln_x)_{0.7}Ca_{0.3}MnO_3$ with Ln = Nd, Gd and Y in the composition range $x \geq x_c$ show certain features of significance . Thus, we find that in the compositions close to $x_c$ ($x \sim 0.6$-$0.7$ when Ln = Nd; $x \sim 0.3$-$0.4$ in the case of Gd), the low temperature $\mu_\beta$ value is significant, reaching values anyway between 1-2.5. It is only when $x$ is considerably large ($x >> x_c$), the $\mu_\beta$ value decreases to values less than unity. These relatively high values of $\mu_\beta$, when Ln = Nd and Gd, are probably due to moments of the rare earths. When Ln = Y, the $\mu_\beta$ values are all low, the highest value of $\sim 1\mu_\beta$ being observed when $x \sim x_c$ (Fig. 4.7.3c).

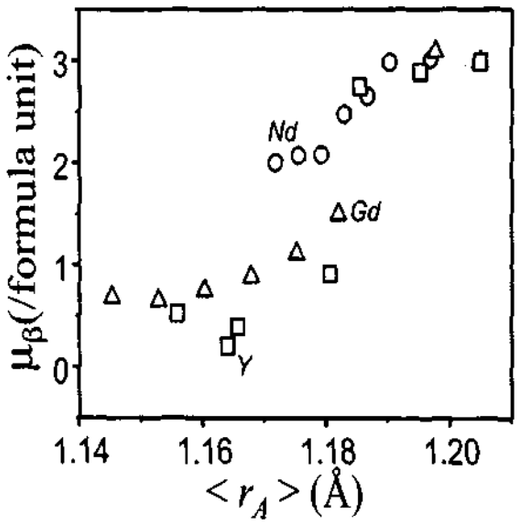


***Fig. 4.7.5*** *Variation of $\mu_\beta$ with $< r_A >$ (Å) in $(La_{1-x}Ln_x)_{0.7}Ca_{0.3}MnO_3$ at 50 K.*

When $x > x_c$, the magnetic moment decreases below $0.5\mu_\beta$. When $x >> x_c$, the presence of small FM clusters cannot be ruled out, even though the CAF interactions may be dominant. The drastic change in the values of $\mu_\beta$ around $x_c$ in the three series of manganates can be attributed to phase separation due to disorder caused by substitution of the smaller rare earth cations in place of La. In the Pr system, phase separation have been reported in the regime of $x \sim x_c$ ($x \sim 0.6$-$0.8$) [29]. To some extent, the results found here are somewhat comparable to those of de Teresa et al [30] who find FMM behavior at low $x$ and spin-glass behavior at large $x$ ($\geq 0.33$) in $(La_{1-x}Tb_x)_{0.67}$ $Ca_{0.33}MnO_3$. In Fig. 4.7.4a, we have plotted the ferromagnetic $T_c$ of the $(La_{1-x}Ln_x)_{0.7}Ca_{0.3}MnO_3$ composition against $x$ ($x \leq x_c$). The $T_c$ decreases with increase in $x$ linearly. In Fig. 4.7.4a, we have also plotted the $T_M$ values of the non-ferromagnetic compositions ($x > x_c$), to show how the $T_M$ value also decreases with increase in $x$, albeit with a considerably smaller slope. In Fig. 4.7.4b, we have plotted the $T_c$ and $T_M$ values against $< r_A >$. The $T_c$ value increases

with increase in $< r_A >$ for $< r_A > \geq 1.18$ Å (or $x < x_c$), while $T_M$ increases with $< r_A >$ with a smaller slope. The $< r_A >$ value of 1.18 Å marks the critical radius beyond which ferromagnetism manifests itself in $(La_{1-x}Ln_x)_{0.7}Ca_{0.3}MnO_3$. It must be noted that in a variety of manganates of the general composition $Ln_{1-x}A_xMnO_3$, an $< r_A >$ of 1.18 Å marks the critical value below which charge ordering becomes robust, rendering it difficult to destroy it by applying magnetic fields or impurity substitutions [13]. An $< r_A >$ 1.18 Å also marks the critical value below which reentrant FM transitions with $T_c < T_{co}$ are seen [31]. The compositions with $< r_A >$ < 1.18 Å are AFM insulators. In Fig. 4.7.5, we have plotted $\mu_\beta$ against $< r_A >$ for the three series of $(La_{1-x}Ln_x)_{0.7}Ca_{0.3}MnO_3$. The $\mu_\beta$ values when $< r_A >$ < 1.18 Å are rather small, well below $3\mu_\beta$, generally less than $1\mu_\beta$. Magnetization in this regime arises from FM interactions in a primarily AFM environment probably due to the presence of magnetic clusters. Thus, the $\mu_\beta$ values in the range of 1-2.5$\mu_\beta$ in Fig. 4 correspond to the phase separation regime where the $< r_A >$ values are in the 1.18-1.165 Å range. This is consistent with results reported for $(La_{1-x}Pr_x)_{0.7}Ca_{0.3}MnO_3$ system [29]. When $< r_A > \leq 1.165$ Å, the $\mu_\beta$ values become considerably smaller, although ferromagnetic interactions due to clusters are likely to be present at low temperatures in this regime as well.

***4.7.3 Resistivity:*** The electrical resistivity data of $(La_{1-x}Ln_x)_{0.7}Ca_{0.3}MnO_3$ (Ln = Nd, Gd and Y) reflect the magnetization data, with the $x \leq x_c$ compositions showing IM transitions (Fig. 4.7.6). The compositions with $x > x_c$ are insulating and do not exhibit IM transitions. For $x \leq x_c$, the value of the resistivity at the IM transition increases with the increase in $x$, and a change in the resistivity of 3-4 orders magnitude is observed at the transition. Thus, the value of resistivity at 20 K for $x \approx x_c$ is considerably higher than that of $La_{0.7}Ca_{0.3}MnO_3$. The temperature of the IM transition, $T_{IM}$, in $x \leq x_c$ compositions decreases linearly with increasing $x$ (Fig.4.7.7). The $T_{IM}$ versus $< r_A >$ plot is linear with a positive slope as expected (see inset of Fig. 4.7.7). We have not observed any resistivity anomaly at $T(<T_{IM})$ in any of the compositions unlike Uehara et al [32] and Deac et al [33].

The small but finite magnetic moments and relatively large resistivities at low temperatures found in $(Ln_{1-x}Ln_x)_{0.7}Ca_{0.3}MnO_3$ for Ln = Pr, Nd, Gd and Y around $x_c$ or $< r_A^c >$ are a consequence of phase separation. Phase separation also causes thermal hysteresis in the resistivity behavior around the IM transitions (see the insets in Fig. 4.7.6). The insets in figures 4.7.6 a, b and c show that the resistivity in the warming cycle is lower than that in the cooling cycle up to a certain temperature beyond which the resistivities in the two cycles merge. Upon cooling the sample below the IM transition, the FMM phase grows at the expense of AFM insulating phase causing a decrease in the resistivity value. When the same sample is warmed, the insulating phase grows at the expense of the FMM phase, the latter providing the conductive path. The thermal hysteresis in resistivity is therefore due to percolative conductivity in these manganates, the hysteresis decreasing with the increase in $< r_A >$ or decrease in $x$ as expected.

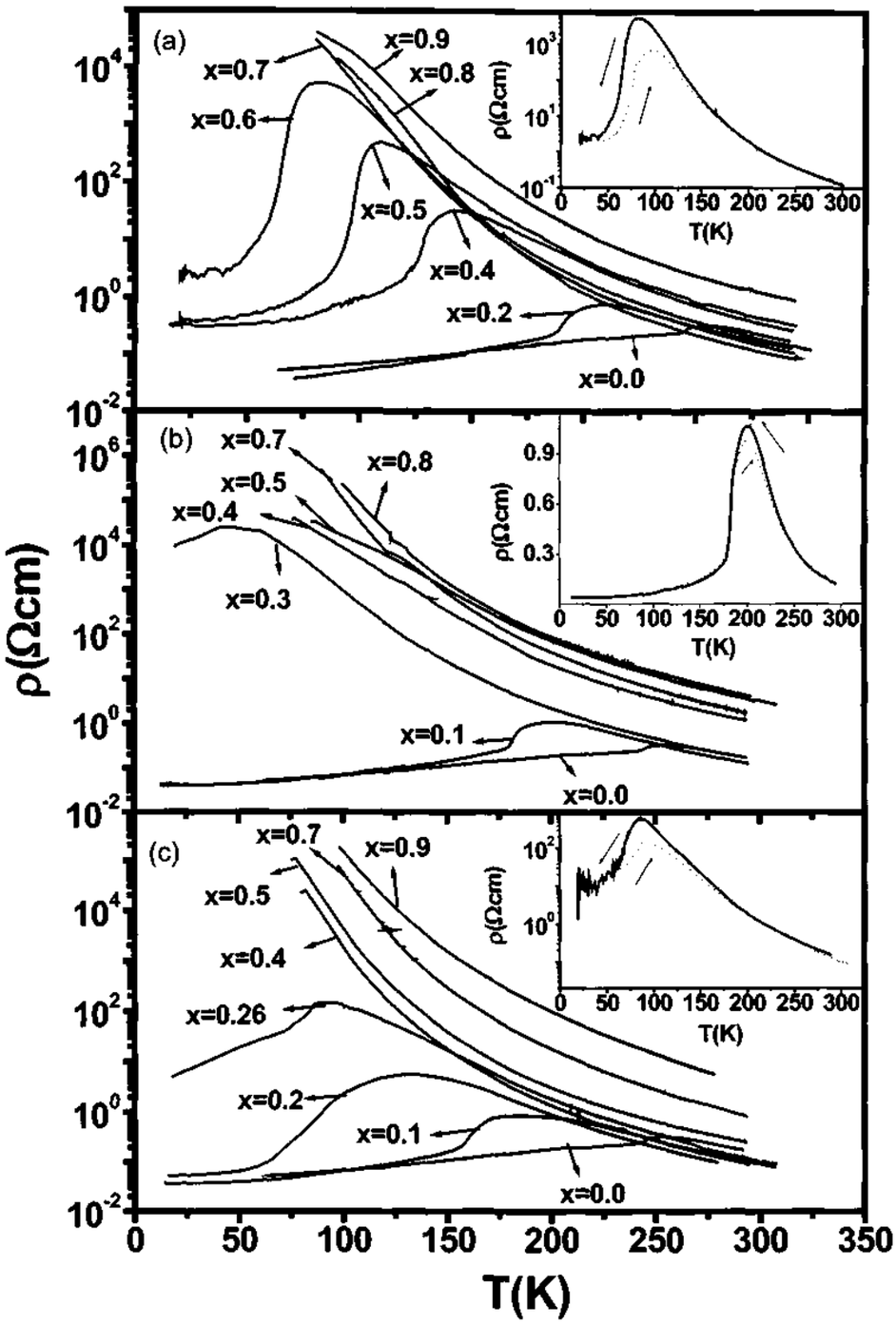


*Fig. 4.7.6 Temperature variation of resistivity in* **(a)** $(La_{1-x}Nd_x)_{0.7}Ca_{0.3}MnO_3$, **(b)** $(La_{1-x}Gd_x)_{0.7}Ca_{0.3}MnO_3$ *and* **(c)** $(La_{1-x}Y_x)_{0.7}Ca_{0.3}MnO_3$. *The broken lines in the inset show warming cycle data.*

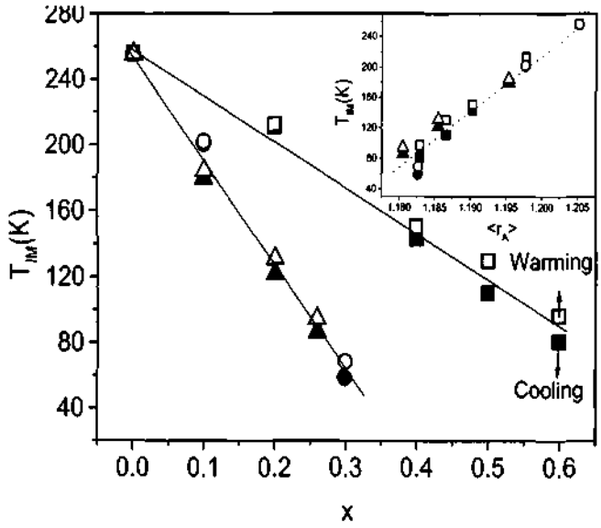


*Fig. 4.7.7 Variation of $T_{IM}$ with x in $(La_{1-x}Ln_x)_{0.7}Ca_{0.3}MnO_3$ for $x \leq x_c$. Inset shows the variation of $T_{IM}$ with $< r_A >$ (Å) for the same composition range.*

It must be noted that the compositions with $< r_A > > 1.18$ Å which are in a homogenous FM phase do not show any hysteresis around $T_{IM}$. Furthermore, the ratio of the peak resistivities in the cooling and heating cycles ($\rho_c/\rho_w$) is constant for samples with $< r_A > > 1.18$ Å in the homogenous FM regime, but increases significantly with decrease in $< r_A >$.

***4.7.4 Size disorder effects:*** Since phase separation in the $(La_{1-x}Ln_x)_{0.7}Ca_{0.3}MnO_3$ series of manganates is related to size disorder caused by the substitution of small ions in place of La, we have quantitatively examined the effect of size disorder in these manganates, in terms of the size variance of the A-cation radius distribution, $\sigma^2$ [12,34]. For two or more A-site species with fractional occupancies $x_i$ ($\sum x_i = 1$), the variance of the ionic radii $r_i$ about the mean $< r_A >$ is given by $\sigma^2 = (\sum x_i r_i^2 - <r_A>^2)$. We have examined the electrical and magnetic

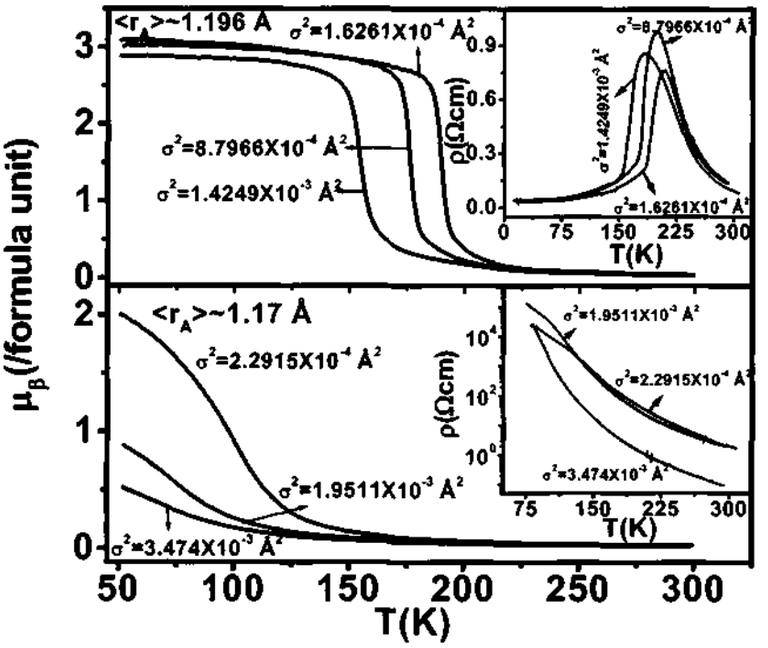


*Fig. 4.7.8 Temperature variation of $\mu_\beta$ in $(La_{1-x}Ln_x)_{0.7}Ca_{0.3}MnO_3$ (a) $< r_A > = 1.196$ Å; (b) $< r_A > = 1.17$ Å. The inset shows the corresponding variations in resistivities.*

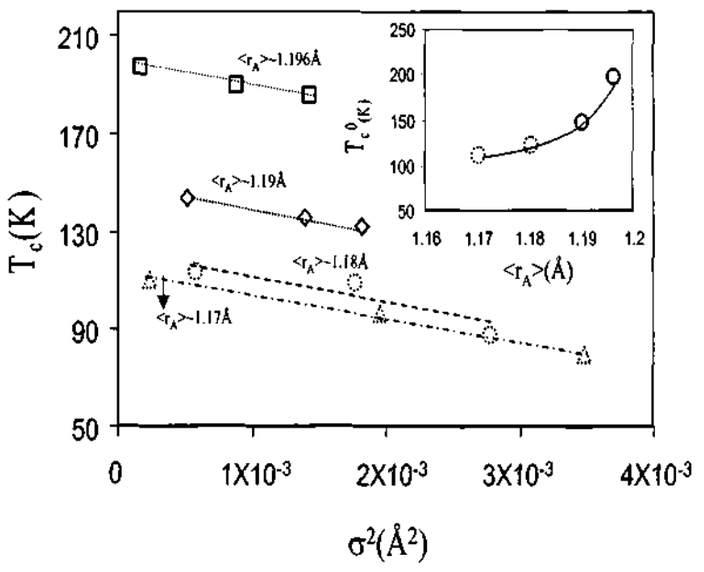


*Fig. 4.7.9 Variation of $T_c$ (solid symbol) and $T_M$ (broken symbol) against $\sigma^2$ (Å$^2$). Inset shows the variation of $T_c^o$ and $T_M^o$ against $< r_A >$ (Å).*

properties for a series of $(La_{1-x}Ln_x)_{0.7}Ca_{0.3}MnO_3$ with fixed $< r_A >$ and variable $\sigma^2$. In Fig.4.7.8, we have shown typical plots of temperature variation of $\mu_\beta$ for fixed $< r_A >$ values of 1.196 and 1.17 Å. We see a decrease in $T_c$ with increase in $\sigma^2$. For $< r_A > = 1.17$ Å the material is not ferromagnetic. The $\mu_\beta$ value as well as $T_M$ show a marked decrease with increase in $\sigma^2$. The resistivity decreases with an increase in magnetization, and when $< r_A > = 1.196$ Å the $T_{IM}$ decreases with increase in $\sigma^2$. In Fig. 4.7.9, we have plotted $T_c$ values of the manganates against $\sigma^2$ for compositions with fixed $< r_A >$ values > 1.18 Å along with the $T_M$ value for fixed $< r_A >$ values ≤ 1.18 Å. Surprisingly, the slopes of the $T_c$ and $T_M$ plots are similar (~9000 K/Å$^2$). The slope of $T_c$ versus $\sigma^2$ in $Ln_{0.5-x}La_xCa_{0.5}MnO_3$, where Ln = Nd and Pr, compositions is reported to be ~ 15000 K/Å$^2$ [31]. The similarity in behavior of these different compositions may be due to presence of ferromagnetic correlations even when $< r_A > \leq < r_A^c >$ or $x > x_c$. By extrapolating the $T_c$ and $T_M$ values to $\sigma^2 = 0$, we obtain the intercepts $T_c^o$ and $T_M^o$, which represent the transition temperatures in the absence of any size disorder. We have plotted the $T_c^o$ and $T_M^o$ values against $< r_A >$ in the inset of Fig. 4.7.9. The $T_c^o$ and $T_M^o$ values increase with increase in $< r_A >$ as expected.

***4.7.5 Percolation:*** As can be seen from Fig. 4.7.6, the resistivity of $(La_{1-x}Ln_x)_{0.7}Ca_{0.3}MnO_3$ compositions show an a IM transition up to $x_c$, and these compositions show a significant increase in resistivity with increase in $x$ more prominently than the compositions with $x > x_c$. Electrical conductivity in the $x \approx x_c$ compositions, are percolative at low temperatures and accordingly, we are able to

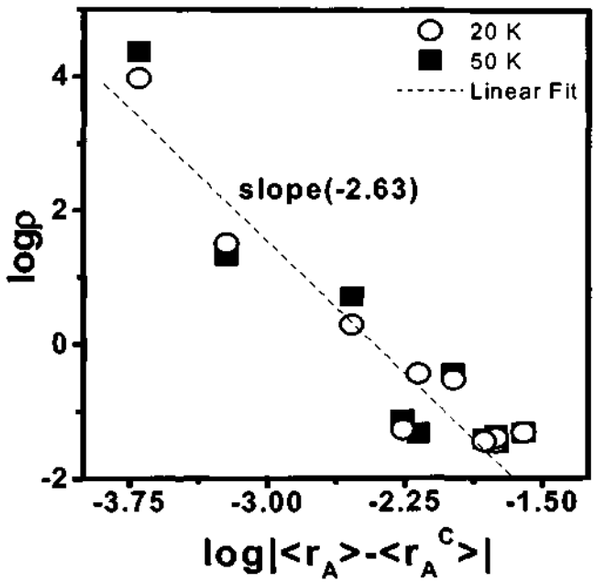


*Fig. 4.7.10 Linear scaling of logρ with log|< $r_A$ >-< $r_A^c$ >| in $(La_{1-x}Ln_x)_{0.7}Ca_{0.3}MnO_3$ at 20 and 50 K.*

fit the low temperature data for the compositions with < $r_A$ > > 1.18 Å to a percolative scaling law, logρ ∝ log| < $r_A$ >-< $r_A^c$ >| as shown in Fig.4.7.10. The slope of the plot is -2.63, a value close to the experimental and predicted values for percolative systems [35].

***4.7.6 Dielectric spectroscopy:*** We have examined the resistivity data of the insulating compositions with $x > x_c$ in some detail to explore whether they conform to activated hopping defined by logρ ∝ $1/T^n$ where, n = 1, 2 or 4. Here, n = 1 corresponds to a simple Arrhenius conductivity. When n = 2, the hopping is called nearest neighbor hopping (NNH). The hopping is controlled by Coulombic forces. When n = 4, the hopping is termed variable range hopping (VRH) and the hopping dynamics is controlled by collective excitation of the charge carries. Figure 4.7.11 shows typical fits of the resistivity data of $(La_{1-x}Y_x)_{0.7}Ca_{0.3}MnO_3$ for $x > x_c$.

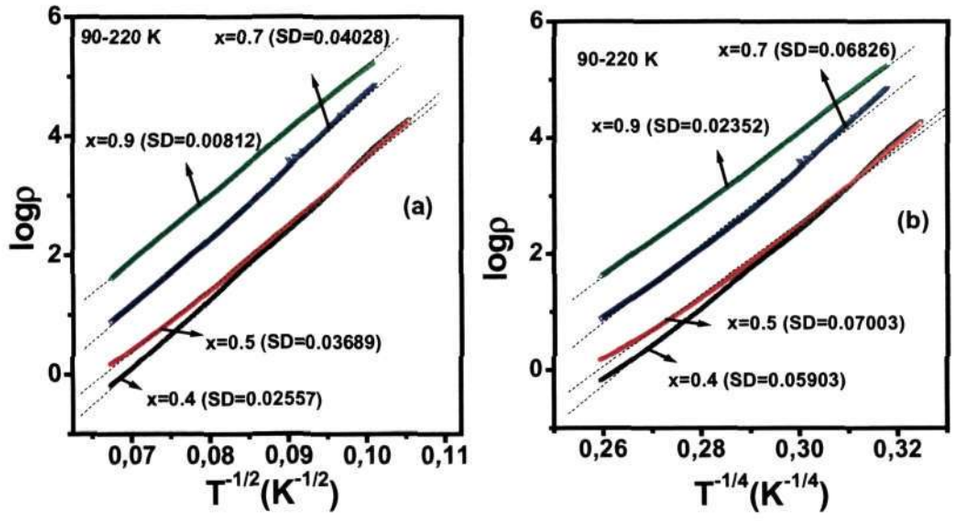


***Fig. 4.7.11*** *Fits of the resisitivity data of $(La_{1-x}Y_x)_{0.7}Ca_{0.3}MnO_3$ for $x > x_c$ to **(a)** $T^{-1/2}$ and **(b)** $T^{-1/4}$ laws in the 90-220 K range. The open symbols are experimental data points and broken lines represents the corresponding linear fits.*

The resistivity data could be fitted to $T^{-1/2}$ dependence with standard deviations varying from 0.008-0.04.The standard deviations for the $T^{-1/4}$ fits were 0.02-0.07. AC conductivity ($\sigma_{ac}$) measurements show a frequency dependence of conductivity, the conductivity increasing with increasing frequency, ω, and decreasing x for a given Lanthanum cation (Fig. 4.7.12a). A fit of $\sigma_{ac}$ to $\omega^s$,gives a value of s in the range 0.5-0.8, consistent with the VRH mechanism [36]. At high temperatures (>150 K), the conductivity exhibits a frequency independence indicating the dominance of DC conductivity.

In Fig. 4.7.12c, we show the temperature response of the real part of the dielectric constant (ε') for $(La_{0.3}Y_{0.7})_{0.7}Ca_{0.3}MnO_3$ at different frequencies. The ε' reaches a high values at ordinary temperatures but decreases dramatically below ~120 K. The temperature at which the drop in ε' occurs increases with increasing frequency, exhibiting a relaxor type behavior. The dielectric relaxation obtained in

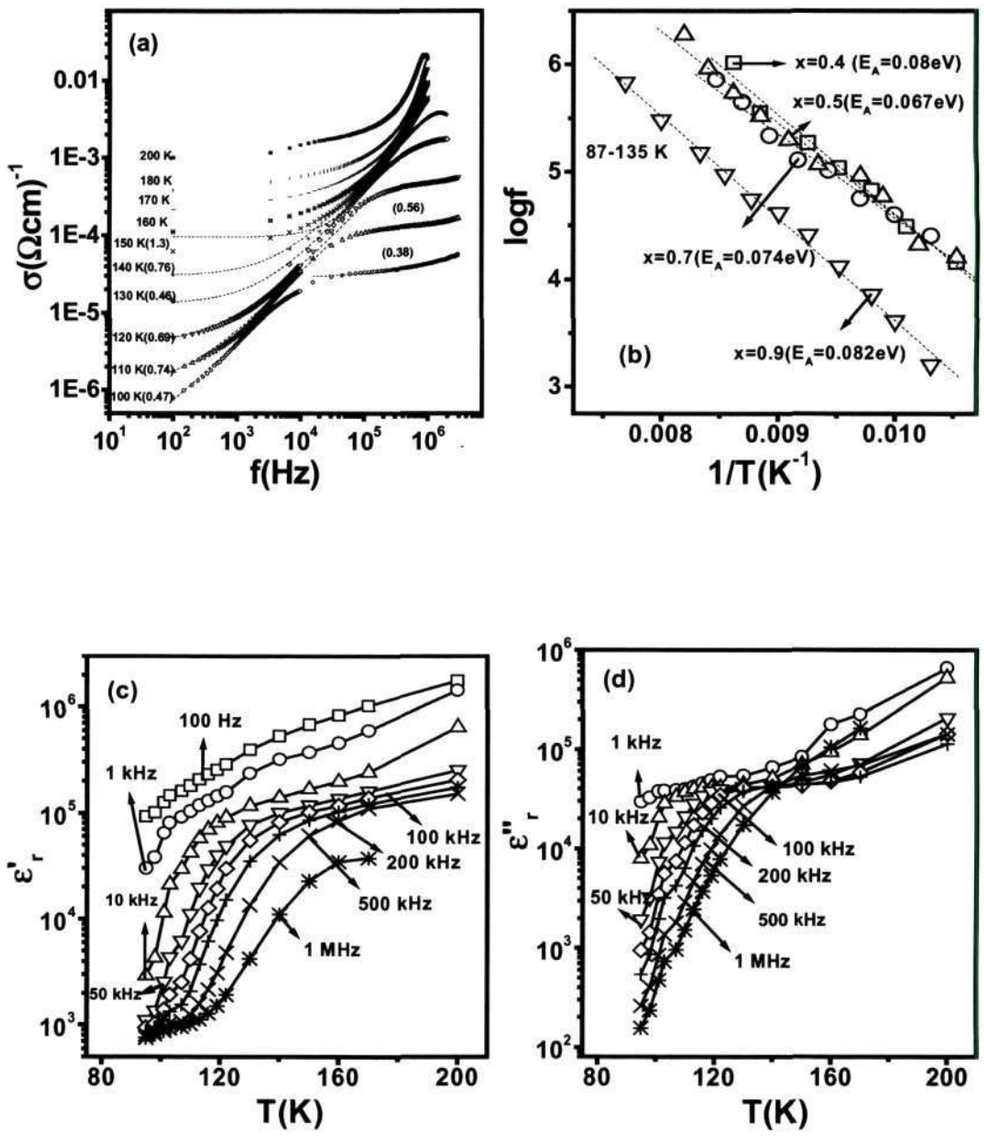


***Fig. 4.7.12 (a)*** *Frequency variation of ac conductivity of* $(La_{0.3}Y_{0.7})_{0.7}Ca_{0.3}MnO_3$ *in the temperature range 80-200 K;* ***(b)*** *Arrhenius plot of frequency corresponding to maximum in tan*$\delta$ *of* $(La_{0.3}Y_{0.7})_{0.7}Ca_{0.3}MnO_3$*;* ***(c)*** *temperature variation of real part of dielectric constant in* $(La_{0.3}Y_{0.7})_{0.7}Ca_{0.3}MnO_3$ *;* ***(d)*** *temperature variation of imaginary part of dielectric constant in* $(La_{0.3}Y_{0.7})_{0.7}Ca_{0.3}MnO_3$.

the $(La_{1-x}Ln_x)_{0.7}Ca_{0.3}MnO_3$ compositions is similar to that found in copper titanate perovskite dielectrics [37].

The imaginary part of the dielectric constant also shows very high dielectric values. The transition temperature in the imaginary part of the dielectric data appears as peaks, which shift to higher temperatures with frequency (Fig.4.7.12d). The unusually high dielectric constant of $(La_{1-x}Ln_x)_{0.7}Ca_{0.3}MnO_3$ for $x > x_c$ can be understood by assuming the presence of conducting domains surrounded by insulating layers with an activated behavior of the intra-domain (non-percolative) conductivity. Such a finite conductivity could be one of the reasons for the high dielectric constant beyond 120 K. The dielectric constant at any given frequency decreases with the decrease in conductivity for $x > x_c$ as expected [38]. Similar to the copper titanates, the $(La_{1-x}Ln_x)_{0.7}Ca_{0.3}MnO_3$ ($x > x_c$) compositions exhibit peaks in the dissipation factor which shifts to higher frequencies with increasing temperature. An Arrhenius plot of frequency with temperature gives a activation energy of 68 meV close to the values in perovskite oxide dielectrics (Fig. 4.7.12b).

***4.7.7 Conclusions:*** The present study of the electronic and magnetic properties of three series of rare earth manganates of the type $(La_{1-x}Ln_x)_{0.7}Ca_{0.3}MnO_3$ where Ln = Nd, Gd and Y, has shown they become ferromagnetic when $x \leq x_c$ accompanied by an insulator-metal transition. These manganates become AFM insulators when $x > x_c$, but show a small increase in magnetic moment at low temperatures ($T < T_M$). $T_c$ and $T_M$ values are both sensitive to cation size disorder. The values of $x_c$ are 0.6, 0.3 and 0.2 respectively for Nd, Gd and Y, correspond to a unique value of average size of the A-site cation, $< r_A >$, of 1.18 Å ($< r_A^c >$). It

must be recalled that this value of $< r_A >$ also marks the critical value below which the ground state is charge ordered. Phase separation is marked around $x_c$ or $< r_A^c >$ in all the series of compositions, although ferromagnetic clusters are likely to be present at low temperatures even when $1.0 > x > x_c$. The origin of phase separation in these series of manganates is likely to be triggered by size disorder arising from the substitution of the smaller rare earth cations in place of La. The results obtained in the present study are consistent with the accepted theoretical models for electronic phase separation in rare earth manganates and other oxide materials [26, 35, 39].

## 4.8 References


1. A. Arulraj, R. Mahesh, G. N. Subbanna, R. Mahendiran, A. K. Raychaudhuri, C. N. R. Rao, *J. Solid. State. Chem.*, 87, 127, 1996
2. W. H. McCarroll, K.V. Ramanujachary, M. Greenblatt, F. Cosandey, *J. Solid. State. Chem.*, 136, 322, 1998
3. C. N. R. Rao, A. R. Raju, V. Ponnambalam, S. Parashar and N. Kumar, *Phys. Rev.*, B 61, 594, 2000.
4. R. C. Budhani, N. K. Pandey, P. Padhan, S. Srivastava and R. P. S. M. Lobo, *Phys. Rev.*, B 65,014429, 2002.
5. S. Srivastava, N. K. Pandey, P. Padhan and R. C. Budhani, *Phys. Rev.*, B 62, 13868, 2001.
6. V. Podzorov, B. G. Kim, V. Kiryukhin, M. E. Gershenson, and S. W. Cheong, *Phys. Rev.*, B 64, 140406, 2001.
7. J. Dho, W. S. Kim, and N. H. Hur, *Phys. Rev. Lett.*, 87, 187201, 2001.
8. A. Guha, N. Khare, A. K. Raychaudhury and C. N. R. Rao, *Phys. Rev.*, B 62, R11941, 2000.
9. A. Machida, Y. Moritomo, K. Ohoyama, T. Katsfuji and A. Nakamura, *Phys. Rev.*, B 65, 64435, 2002.
10. P. Murugavel, C. Narayana, A. K. Sood, S. Parashar, A. R. Raju and C. N. R. Rao, *Europhys. Lett.*, 52, 461, 2000.
11. P. G. Radaelli, R. M. Ibberson, D. N. Argyriou, H. Casalta, K. H. Andersen, S. W. Cheong and J. F. Mitchell, *Phys. Rev.*, B 63, 62419, 2000.
12. L. M Rodriguez-Martinez and J. P. Attfield, *Phys. Rev.*, B 54, R15622, 1996.

13. C. N. R. Rao, A. Arulraj, A. K. Cheetham and B. Raveau, *J. Phys.: Condens. Matter*, 12, R 83, 2000.

14. K. V. Sarathy, P. V. Vanitha, R. Seshadri, A. K. Cheetham and C. N. R. Rao, *Chem. Mater.*, 13, 787, 2001.

15. P. N. Santosh, A. Arulraj, P. V. Vanitha, R. S. Singh, K. Sooryanarayana and C. N. R.Rao, *J. Phys.: Condens. Matter*, 11, L27, 1999.

16. A. Maignan, C. Martin, F. Damay, and B. Raveau, *Chem. Mater.*, 10, 950, 1998.

17. A. Maignan, C. Martin, F. Damay, B. Raveau and J. Hejtmanek, *Phys. Rev.*, B 58, 2758, 1998.

18. J. Hejtmanek, Z. Jirak, M. Marysko, C. Martin, A. Maignan, M. Hervieu, and B. Raveau, *Phys. Rev.*, B 60, 14057, 1999.

19. W. H. Meiklejohn and C. P. Bean, *Phys. Rev.*, 102, 1413, 1956.

20. D. V. Dimitrov, S. Zhang, J. Q. Xiao, G. C. Hadjipanayis and C. Prados, *Phys. Rev.*, B 58, 12090, 1998.

21. Z. Li and S. Zhang, *Phys. Rev.*, B 61, R14897, 2000.

22. L. A. Bendersky, R. Chen, I. D. Fawcett, M. Greenblatt, *J. Solid. State. Chem.*, 157, 309, 2001.

23. I. D. Fawcett, J. E. Sunstrom IV, M. Croft, K. V. Ramanujachary and M. Greenblatt, *Chem. Mater.*, 10, 1998, 3643.

24. C. N. R. Rao, P. Ganguly, K. K. Singh and R. A. Mohan Ram, *J. Solid. State. Chem.*, 72,14, 1988.

25. A. Moreo, S. Yunoki, E. Dagotto, *Science*, 283, 2034, 1999.

26. C. N. R. Rao, P. V. Vanitha and A. K. Cheetham, *Chem. Eur. J.*, 4, 9, 2003.

27. C. Martin, A. Maignan, M. Hervieu and B. Raveau, *Phys. Rev.*, B 60 12191, 1999.

28. H. Terashita and J. J. Neumeier, *Phys. Rev.*, B 63, 174436, 2001.

29. A. M. Balagurov, Y. Yu. Pomjakushin, D. V. Sheptyakov, V. L. Aksenov, P. Fischer, L. Keller, O. Yu. Gorbenko, A. R. Kaul and N. A. Babushkina, *Phys. Rev.*, B 64, 024420, 2001.

30. J. M De Teresa, M. R. Ibarra, J. Garci'a, J. Blasco, C. Ritter, P. A. Algarabel, C. Marquina and A. del Moral, *Phys. Rev. Lett.*, 76, 3392, 1996.

31. P. V. Vanitha and C. N. R. Rao, *J. Phys.: Condens Matter*, 13, 11707, 2001.

32. M. Uehara, S. Mori, C. H. Chen and S.-W. Cheong, *Nature*, 399, 560, 1999.

33. I. G. Deac, S. V. Diaz, B. G. Kim, S.-W. Cheong, and P. Schiffer, *Phys. Rev.*, B 65, 174426, 2002.

34. P. V. Vanitha, P. N. Santosh, R. S. Singh, C. N. R. Rao and J. P. Attfield, *Phys. Rev.*, B 59, 13539, 1999.

35. C. N. R. Rao and P. V. Vanitha, *Curr. Opp. Solid State Mater. Sci.*, 6, 97, 2002.

36. K. Vijaya Sarathy, S. Parashar, A. R. Raju and C. N. R. Rao, *Solid State Sci.*, 4, 353, 2002.

37. C. C. Homes, T. Vogt, S. M. Shapiro, S. Wakimoto and A. R. Ramirez, *Science*, 293, 673, 2001.

38. L. He, J. B. Neaton, M. H. Cohen, D. Vanderbilt and C.C. Homes, *Cond-mat/0110166*, 2002.

39. E. Dagotto, T. Hotta and A. Moreo, *Phys. Rep.*, 344, 1, 2001.

# 5. OTHER WORK CARRIED OUT BY THE CANDIDATE

## 5.1 Bonding of monazite to $Al_2O_3$ and $TiO_2$ ceramics

***5.1.1 Introduction***: Recent work of Morgan et al [1, 2] has shown monazite, $LaPO_4$ to be a suitable weak bonding material in preparing composites with $Al_2O_3$. These composites show high toughness with an interface sufficiently weak for debonding to occur when cracks are deflected into monazite and away from the $Al_2O_3$ phase. $LaPO_4$ in the $Al_2O_3$ composites is quite stable and no reaction occurs between the two phases upto 1600 $^0$C, provided the La : P ratio in the monazite is close to one [3]. Furthermore, composites of $LaPO_4$ with some other ceramics are machinable [4]. Interface properties of $LaPO_4$ with $Al_2O_3$ and yttrium aluminium garnet (YAG) fibers have also yielded useful information on the mechanical properties of the interfaces [5, 6].

A systematic investigation has been carried out on the particulate composites of $Al_2O_3$ and $TiO_2$ with a variety of monazites, $LnPO_4$ (Ln = La, Pr, Nd or Gd) by means of scanning electron microscopy in order to check the chemical compatibility of these $LnPO_4$ with alumina and titania. The studies reveal all the monazites to be compatible with the oxide ceramics and have favorable mechanical properties in terms of damage tolerance and increase in fracture toughness.

***5.1.2 Experimental:*** All the monazites $LnPO_4$ were synthesized by mixing phosphoric acid with a rare earth oxide or acetate. The composites were prepared by mixing the monazite powder (~600nm in size) with the powder of ceramic oxide

(~300nm in size) in agate mortar with addition of 2% PVA binder and pelletizing them by applying a uniaxial pressure of approximately 2.5 tonnes. Mixtures of $Al_2O_3$ and monazite (3, 5, 7 and 15 molar percent) were pelletized and heated to 1200 $^0$C and 1350 $^0$C for 15hrs and 1600 $^0$C for 2hrs, the last being found to be the ideal temperature for sintering. In the case of the $TiO_2$ composites mixtures of $TiO_2$ containing 1, 3 and 5 molar percent of monazite were pelletized and heated to 1000 $^0$C and 1200 $^0$C for 12hrs and 1300 $^0$C for 4hrs. The concentration of the monazite was restricted to 5 molar percent in the case of $TiO_2$, due to segregation at high temperatures. The microstructure evolution and composition were monitored by scanning electron microscopy (Leica S440I) and energy dispersive X-ray analysis (Links). Mechanical testing for determining hardness and fracture toughness (by measuring the ratio $a/c^{3/2}$ wherein, a is half the diagonal length of the contact impression and c is the crack length) was carried out by Vickers indentation method (Vickers Armstrongs).

### *5.1.3 Results and Discussion*

***5.1.3a Microstructure of $Al_2O_3$ and $TiO_2$ composites with monazite:*** In Fig. 5.1.1a we show the SEM image of the surface microstructure of $Al_2O_3$ with 7 molar percent of $LaPO_4$. The bright regions around the $Al_2O_3$ grains corresponds to $LaPO_4$ which is more clearly seen in the backscattered image due to high elemental contrast, characteristic of backscattered images. The images show that monazite is deformed under the tensile and compressive stresses exerted by $Al_2O_3$ grains.

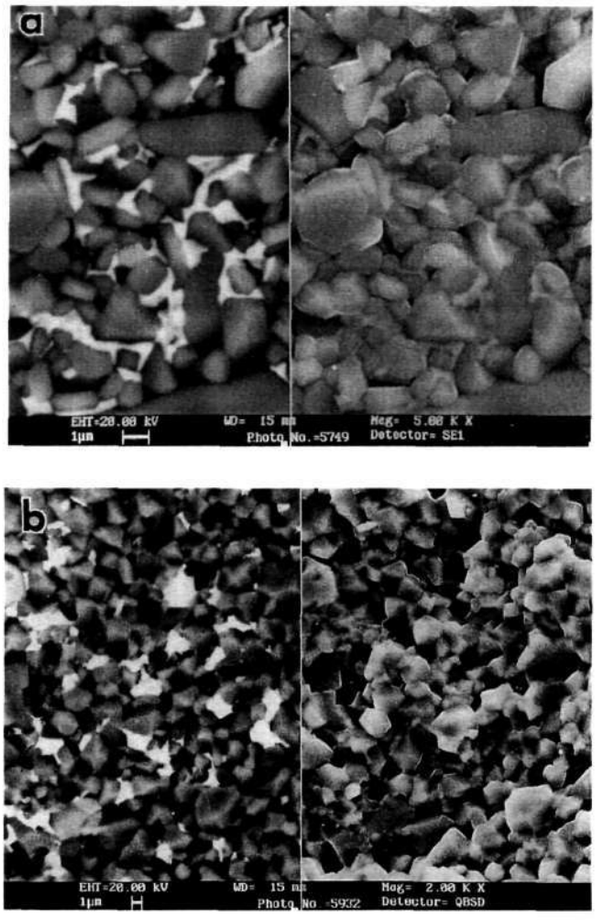


***Fig. 5.1.1**. Scanning electron micrographs showing **(a)** the surface morphology of $Al_2O_3$ composites with 7 mol% $LaPO_4$ and **(b)** fractured surface of $Al_2O_3$ with 3 mol% $NdPO_4$ sintered at 1600°C for 2 h. The left half side images are backscattered electron images and the right half side images are secondary electron images.*

The EDAX results show these regions to be slightly rich in phosphorous (P/La~1.2). Since the monazite composition is on the P-rich side, it seems to have melted when these composites were heated to temperature in excess of 1300 $^0$C. This appears to be quite different from that reported in literature wherein a $AlPO_4$ phase surrounding the

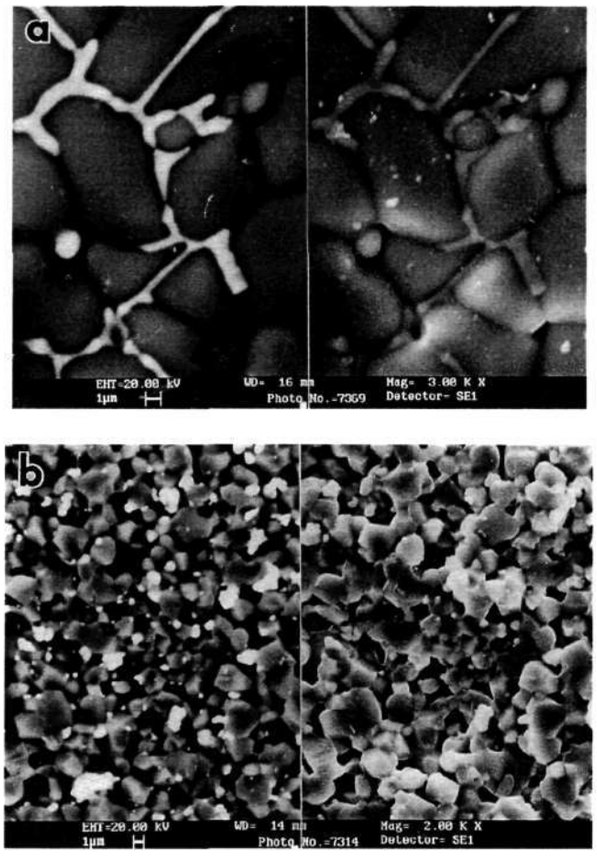


***Fig.5.1.2**. Scanning electron micrographs showing **(a)** surface morphology and **(b)** fractured surfaces of $TiO_2$ composite with 3 mol% $NdPO_4$ sintered at 1300°C for 4 h. The left half side images are backscattered electron images and the right half side images are secondary electron images.*

$Al_2O_3$ grains were found in the composites containing phosphorous rich rhabdophane [3]. According to the phase diagram available on $Ln_2O_3$-$P_2O_5$ [7], compositions rich in phosphorous undergo (when P:Ln is between 1 and 3) a incongruent melting at approximately 1300-1350 $^0$C leading to the formation of $LnPO_4$+liquid ($P_2O_5$).

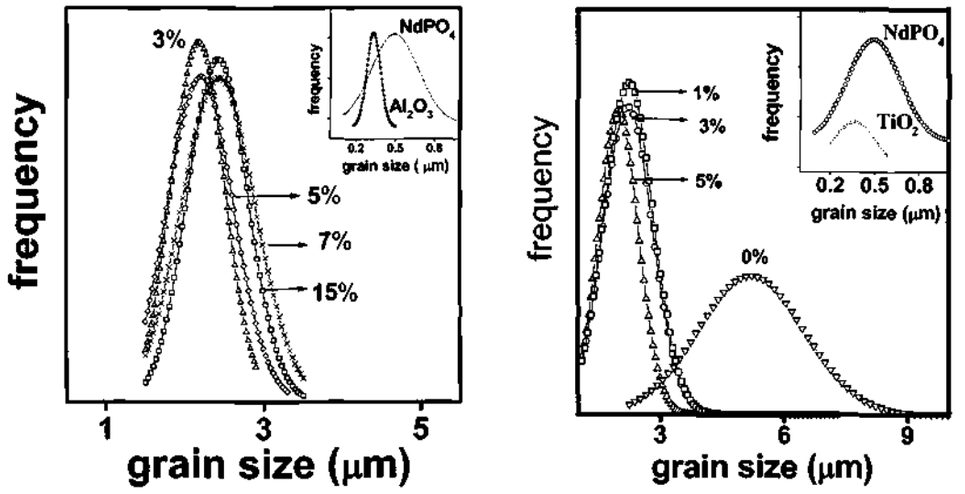


*Fig. 5.1.3. The grain size distribution of the composites of (a) $Al_2O_3$ and (b) $TiO_2$ with different concentrations of $NdPO_4$. The insets show the initial particle size distribution for the starting materials.*

In the present study the compositions of these P-rich lanthanum phosphates was $5Ln_2O_3.6P_2O_5$, which melts into $LnPO_4$+liquid at higher temperatures (around 1300 $^0$C). This incongruent melting and deformation seem to be responsible for the kind of morphology seen in $Al_2O_3$-$LnPO_4$ composites. The flow of $LnPO_4$ promotes the binding of the randomly oriented $Al_2O_3$ grains. Fig. 5.1.1b shows the fractured surface of 3 molar percent $NdPO_4$ in $Al_2O_3$.

A study of the variation in concentration of the monazite in the $NdPO_4$-$Al_2O_3$ composites showed that 3 mole percent was sufficient to provide bonding. In Fig. 5.1.2a we show the surface morphology of a $TiO_2$-$NdPO_4$ (3%) composite heated to 1300 $^0$C for 4hrs. The fractured surface of the same is shown in Fig. 5.1.2b. The SEM images of fractured surfaces of $Al_2O_3$ composites with Pr, Nd and Gd monazites gave a

similar result, in that, all of them show bonding with the monazite material present around the alumina grains due to peritectic melting.

***5.1.3b Grain size:*** In addition to providing bonding, monazite materials have a beneficial effect in terms of inhibiting the uneven grain growth and obtaining uniformity in grain size of ceramic materials. Fig.5.1.3a shows that the addition of $NdPO_4$ to $Al_2O_3$ ceramic results in uniform grain growth of $Al_2O_3$ ceramics with a narrow distribution of grain sizes around 2 microns. $TiO_2$, unlike $Al_2O_3$ exhibits higher rate of grain growth at 1300 $^0$C as can be seen from Fig. 5.1.3b. Addition of even 1 molar percent of monazite ($NdPO_4$) limits the grain growth of $TiO_2$ substantially.

***5.1.3c Vickers hardness and fracture toughness:*** Fig. 5.1.4 shows the results of the Vickers hardness tests carried out on $Al_2O_3$-$NdPO_4$ and $TiO_2$-$NdPO_4$ composites heated to 1600 $^0$C (2hrs) and 1300 $^0$C (4hrs) respectively. The hardness decreases with the increasing monazite concentration in both the $Al_2O_3$ and $TiO_2$ composites. The decrease in the hardness value can be attributed to the greater deformability of the composites with the increase in the concentration of the monazite in the oxide matrix. In the case of $Al_2O_3$-$LnPO_4$ composites, the hardness increases slightly when Ln is changed from La to Gd. Measurement of the fracture toughness of the $TiO_2$-$NdPO_4$ composites (sintered to 1300 $^0$C for 4hrs) showed that upon increasing the concentration of monazite, the toughness increases slightly as shown in Fig. 5.1.4b.

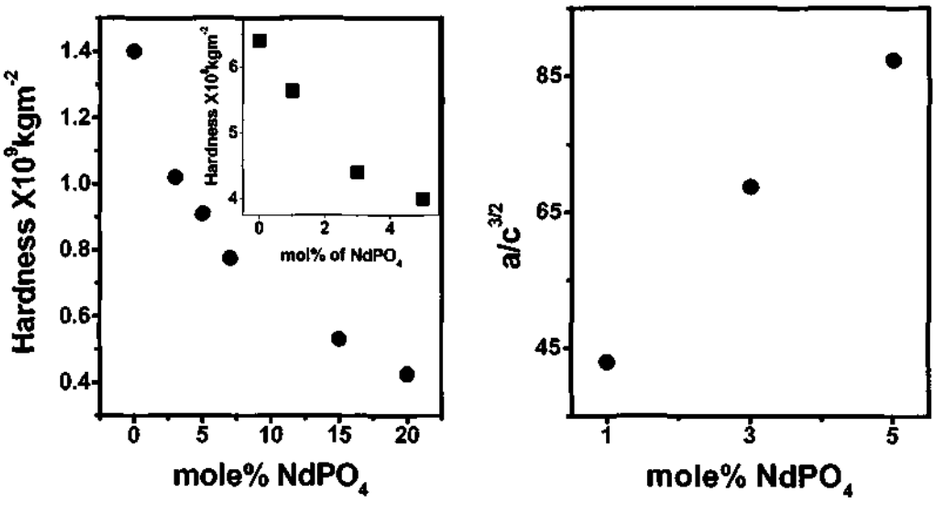


*Fig. 5.1.4 (a) Variation of Vickers hardness with $NdPO_4$ concentration for $Al_2O_3$ composite. Inset shows the hardness variation for $TiO_2$ composite with $NdPO_4$. (b) Variation of the ratio $a/c^{3/2}$ with the concentration of $NdPO_4$ for $TiO_2$ composite.*

It is noteworthy that, the toughness could not be measured in the case of pure $TiO_2$ because of chipping of the grains at the point of indentation. The incorporation of monazite certainly imparts damage tolerance properties to oxide ceramics as was seen for the machinable specimens [4].

***5.1.4 Conclusions:*** Rare earth phosphates, $LnPO_4$ (Ln = La, Pr, Nd and Gd) are quite compatible with oxide ceramics even when the ratio of P : Ln is slightly greater than 1. Although there is an incongruent melting of these systems (when rich in P) into monazite and liquid, there appears to be no reaction at the interface between alumina and monazite. Vickers hardness decreases with the increasing monazite content in both $Al_2O_3$ and $TiO_2$ composites. The increased fracture toughness and resistance to mechanical stress in these composites is due to (1) weak bonding between the monazite

phase and alumina and (2) deformation of $LnPO_4$ like smearing of material under the local stresses. Furthermore, bonding with the monazite limits the grain growth of the oxide ceramics, as seen in the case of $TiO_2$ ceramics.

### 5.1.5 References

1. P. E. D. Morgan, D. B. Marshall and R. M. Housley, *Mater. Sci. Eng.*, A, 195, 215, 1995.

2. P. E. D. Morgan and D. B. Marshall, *J. Am. Ceram. Soc.*, 78, 1553, 1995.

3. D. B. Marshall, P. E. D. Morgan, R. M. Housley and J. T. Cheung, *J. Am. Ceram. Soc.*, 81, 951, 1998.

4. J. B. Davis, D. B. Marshall, R. M. Housley and P. E. D. Morgan, *J. Am. Ceram. Soc.*, 81, 2169, 1998.

5. D. H. Kuo and W. M. Kriven, *Mater. Sci. Eng.*, A, 210, 123, 1995.

6. D. H. Kuo and W. M. Kriven, *J. Am. Ceram. Soc.*, 80, 2987, 1997.

7. D. Agrawal and F. A. Hummel, *J. Electrochem. Soc.: Solid-State Science and Technology*, 127, 1550, 1980.

## 5.2 Peptide-induced formation of silica from tetraethylorthosilicate at near - neutral pH

***5.2.1 Introduction:*** Geological synthesis of silica-related materials occurs at extremes of pH, temperature and pressure. Even laboratory synthesis of silica is generally carried out at high/low pH values. Biological silica, on the other hand, is formed around neutral pH and under less severe temperatures and pressures. Biogenic silica bodies in higher plants (phytolyths) contain protein residues, which are suspected to play a role in silica precipitation. Bio-mineralization of silica is different from that of ionic compounds such as calcite which are crystalline and exhibit hierarchical architectures. Silica bio-mineralization generally leads to amorphous products indicating that templating does not dictate crystallinity. Hilderbrand et al. [1] have isolated and characterized clones encoding proteins that interact with silicon and transport it. They have also demonstrated silicon uptake activity of the cDNA encoding silicon transporter from the diatom *Cylindrotheca fusiformis*. Cha et al. [2] have isolated the protein, silicatein, from the marine sponge *Tethya aurantia*, which has three similar subunits of which silicatein α (70% mass of the protein) catalyzes the formation of silica from tetraethylorthosilicate (TEOS). Site-directed mutagenesis of the silicatein α filament has shown the importance of serine and histidine residues in the active site for the catalytic hydrolysis and polymerization of siloxane [3]. Synthetic block co-polypeptides containing cysteine, lysine, serine, glutamine and alanine [4] have also been shown to mimic the properties of silicatein at near neutral pH. Kroger et al. [5,6] have reported the discovery of low molecular weight proteins called silaffins

from *Cylindrotheca fusiformis* containing polyamines linked to lysine groups which are responsible for catalyzing silica mineralization. Adding silaffins to solutions of silicic acid produced silica nanospheres of different shapes and sizes. Based on the above studies, it would appear that lysine-containing peptides and proteins may be especially effective in hydrolyzing TEOS and subsequently forming silica.

We considered it important to systematically investigate the interaction of TEOS with lysine and serine and their oligomers as well as polypeptides to quantitatively examine their effectiveness in hydrolyzing the ester at near neutral pH followed by the formation of silica. In particular, it was of interest to know whether the hydrolysis of TEOS was significantly faster in the case of oligomers and polypeptides compared to the parent amino acids since they would probably provide greater hydrogen bonding sites with $(SiOH)_X$ type species [7]. We have also examined the interaction of TEOS with polycysteine for purpose of comparison. In order to explore whether the presence of lysine and serine in synthetic polypeptides also favoured the formation of silica at neutral pH, we have investigated the interaction of TEOS with a few peptides with and without these amino acids, since there is reason to believe that the occasional presence of specific amino acids may suffice to yield amorphous silica [8]. The present study establishes the formation of silica by the hydrolysis of TEOS by lysine and serine containing peptides at near-neutral pH.

***5.2.2 Experiment:*** All the amino acids were obtained from Sigma Aldrich and were used without further purification. Oligomers and polypeptides of lysine, serine and cysteine were obtained from Bachem. The hydrolysis of TEOS (Fluka) by the

amino acids was carried out in a 1.5 ml tube with a closed lid placed in a thermostat maintained at 303 K at ambient pressure. The samples were kept in a shaker rotating at a constant speed throughout the experiment. In a typical experiment 0.267 ml TEOS was added to 10 μl of 5 mM solution of lysine. The pH was maintained by adding 20 μl of Tris buffer at pH 6.9. The total volume was made up to 1ml by adding double distilled water. The effective concentration of the amino acid was therefore 0.068 mM and that of TEOS was 1.2 mM. The silica precipitate was extracted by centrifugation (at 13000 rpm), washed twice with double distilled water and finally with isopropanol (silica samples that settled down at the bottom were only collected for estimation). The samples were then vacuum dried for 20 min to remove the organic solvent and water. The silica thus obtained was amorphous as evidenced by x-ray diffraction. The amount of silica was estimated by fusing it with sodium bicarbonate in a platinum crucible at 900 $^0$C, and the resultant sodium silicate was dissolved in double distilled water and diluted to a known quantity (100 ml). The quantity of silica in the solution was then estimated by the ammonium molybdate method [9] by measuring the absorbance at 810 nm against double distilled water. A similar procedure was employed for serine as well as other amino acids such as Arg, Glu, Asp, Gln, Gly, Met and Ala. A blank experiment was carried out by taking TEOS in the neutral buffer medium in the absence of amino acids. The effect of concentration of the amino acids at neutral pH on the hydrolysis of TEOS was examined by the same procedure. The effect of pH on the hydrolysis of TEOS was examined by the same procedure. The effect of pH on the hydrolysis of TEOS was studied by fixing the concentration of amino acid and varying the pH of the medium by adding Tris buffers corresponding to pH

6 and 5. In order to study the kinetics of hydrolysis of TEOS, known aliquots were taken out at different time intervals from the sample tubes maintained at 303 K in a shaker. The amount of silica was estimated as a function of time in these experiments.

In the case of oligomers and polypeptides of lysine and serine (mol wt: 5000-15000), 5 mM solutions were prepared by dissolving them in double distilled water. The concentrations of the polypeptides were calculated based on their average molecular weights. These solutions were taken with TEOS and diluted as described earlier in the case of the amino acids. Since, polycysteine was partially insoluble, the solution was homogenized by using a vortex before setting up the reaction. The experimental procedure for studying the interaction of TEOS with oligomer and polypeptides was similar to that with amino acids.

We have studied the hydrolysis of TEOS by the following synthetic peptides obtained from Center for Biochemical Technology, New Delhi: 1, R-L-S-K-R-V-S-A-M-Q-N-S-G-V-N-D, 2, Y-G-G-F-S-K-K-K-F-M-R-F and 3, S-G-G-L-H-G-V-G. Solutions of 5 mM concentration were prepared by dissolving these polypeptides in double distilled water and the hydrolysis of TEOS carried out by the procedure described earlier.

### *5.2.3 Results and Discussion*

***5.2.3a Effect of amino acids:*** Interaction of TEOS with lysine and serine at neutral pH gives rise to amorphous silica, although the rates are very small.

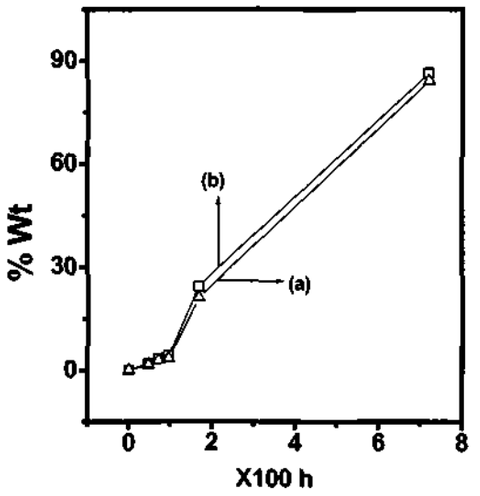


***Fig.5.2.1*** *Rate of formation of silica from TEOS in an aqueous solution containing 0.068 mM of the amino acid :* ***(a)*** *lysine and* ***(b)*** *serine at pH 6.9.*

In Fig. 5.2.1, the plots of the weight percent of silica formed against time at a fixed amino acid concentration of 0.068 mM are shown. ÅThe rates of formation of silica are comparable for lysine and serine. When TEOS was added to a solution of cysteine, the aqueous layer containing cysteine gradually merged with the TEOS layer to give a homogenous solution which then formed a transparent gel after 24 h. We could not therefore study the rates in the case of cysteine. Arg, Glu, Asp, Gln, Gly, Met and Ala did not initiate the hydrolysis of TEOS under similar conditions even upto 120 h. It must be noted that, in the absence of any amino acid, the hydrolysis of TEOS was initiated after 192 h from the start of the experiment. While the Zwitterionic nature of the amino acids may provide acid-base sites for catalyzing the hydrolysis of TEOS, the specific ability of lysine and serine to hydrolyze TEOS to produce silica may be linked to the presence of the $NH^{+}_{3}$ and

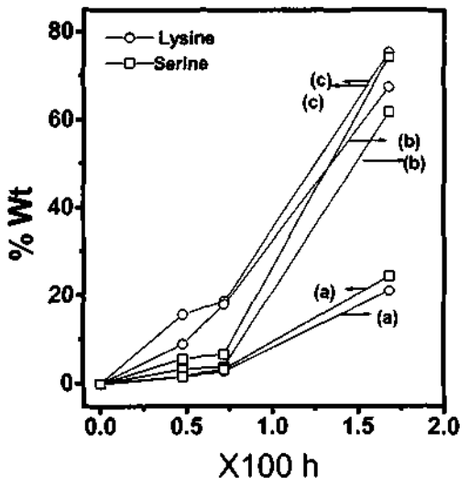


***Fig.5.2.2*** *Rate of formation of silica from TEOS in an aqueous solution at different concentrations of lysine and serine* ***(a)*** *0.068 mM,* ***(b)*** *0.136 mM and* ***(c)*** *0.272 mM.*

OH functional groups attached to the amino acid on the alpha side chain. Hydrogen bonding of the amine and hydroxyl hydrogens with the $(SiOH)_X$ moiety may be responsible for their reactivity [7].

***5.2.3b Effect of concentration:*** In order to quantitatively compare the effectiveness of lysine and serine in hydrolyzing TEOS to produce silica, we carried out experiments at different concentrations of the two amino acids. In Fig.5.2.2, we have plotted the weight percent of silica formed at neutral pH at different concentrations of lysine and serine.

Lysine is somewhat more effective than serine, particularly in the initial period of hydrolysis and polymerization. The difference becomes smaller at longer periods

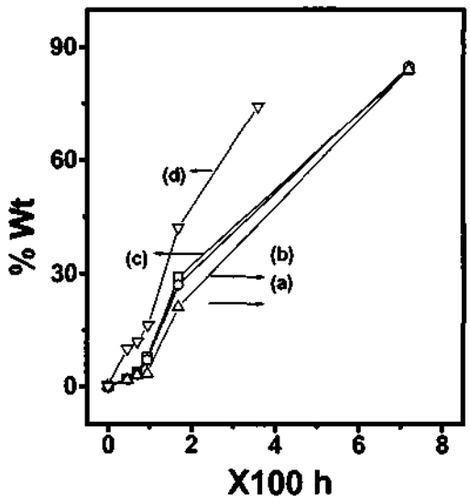


*Fig.5.2.3 Rate of formation of silica from TEOS in 0.068mM solution of **(a)** lysine **(b)** $(lysine)_2$, **(c)** $(lysine)_3$ and **(d)** $(lysine)_4$.*

(~180 h). Accordingly, an increase in the concentration of lysine from 0.068 mM to 0.136 mM has a significant effect on the hydrolysis of TEOS. Such an effect of amino acid concentration establishes that the amino acid is directly involved in the process of formation of silica from TEOS. The mechanism of hydrolysis of TEOS by lysine itself is likely to involve the attack by the $NH_3^+$ end of the alpha side chain on the ester oxygen and follows the known behavior of lysine in such reactions.

***5.2.3c Effect of pH:*** The rate of hydrolysis of TEOS by serine and lysine is affected markedly by the pH of the solution. Thus, the rate is markedly greater at a pH of 5, and comparable at pH values of 6 and 6.9. The faster rate of hydrolysis at pH 5 is mainly due to the medium rather than the amino acid. At pH 6, hydrolysis could be competitive or co-operative between the $H^+$ ions from the buffer and the amino acid, resulting in a rate higher than that at pH 6.9, which is purely due to the amino acid.

The hydrolysis of TEOS by amino acids is slow in comparison to silicatein [2] where the enzymatic sites may favor the orientation of the hydrolyzed TEOS for polymerization. In order for species such as $(SiOH)_x$ or the small oligomeric silicate units present in solution as a result of catalytic hydrolysis to polymerize and form $SiO_2$, they need to be assembled or anchored on to an appropriate host. Since the hydrolyzed product of TEOS would tend to form hydrogen bonds with the peptides, we would expect the magnitude of hydrogen bonding to increase with the number of hydrogen bonding sites in the peptide. There is reason to believe from the literature that small chain peptides would aid the hydrolysis of silicic acid from solution. A molecular orbital modeling of the diatom *frustule* [9] has shown that sheets of hydroxyl containing polypeptides would induce the growth of silica at the interface when reacted with silicic acid. It has been suggested that the formation of amorphous silica require only an occasional, non-regular occurrence of amino acid pairs such as Ser-Ser interspersed within a polypeptide.

***5.2.3d Effect of Oligomers:*** We have, therefore studied the interaction of TEOS with di, tri and tetra peptides of lysine. We show the results on the formation of silica effected by the various oligomers in Fig. 5.2.3. The rate of formation of silica is rather high with tetralysine, and is most effective even over extended periods. In Fig. 5.2.4 we compare the formation of silica by polylysine, polyserine and polycysteine after a fixed period of time, keeping the concentration of the polypeptides at 0.068 mM. Polylysine

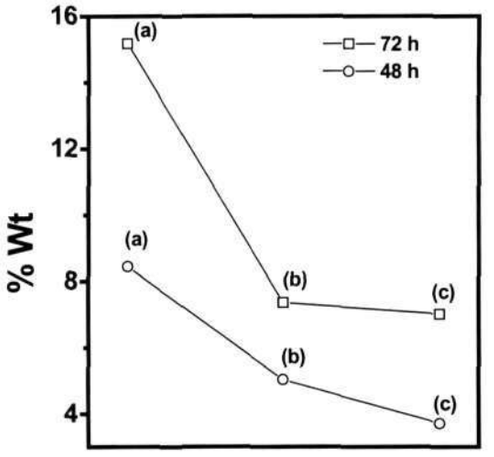


***Fig.5.2.4*** *Silica formed at different time intervals by reaction of TEOS with* ***(a)*** *polylysine,* ***(b)*** *polyserine and* ***(c)*** *polycysteine ( ~ 0.068 concentration).*

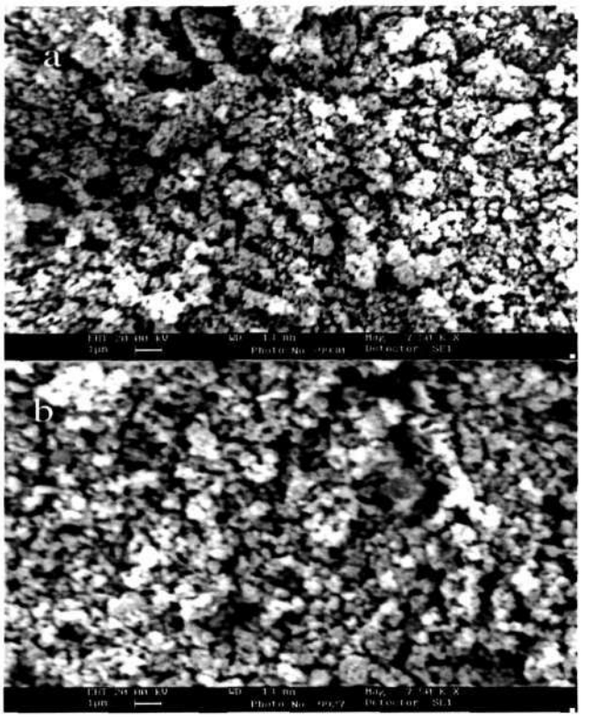


***Fig.5.2.5*** *SEM images of silica obtained by the hydrolysis of TEOS by* ***(a)*** *polylysine and* ***(b)*** *peptide-1.*

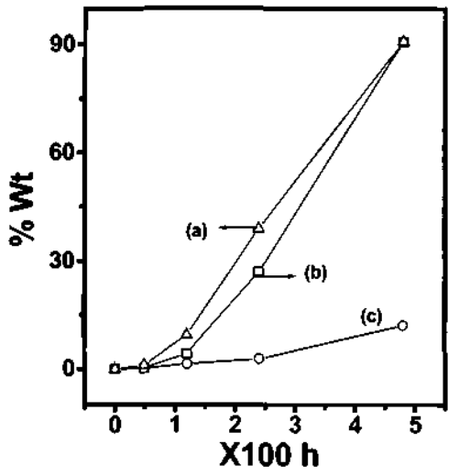


*Fig. 5.2.6 Rate of formation of silica from TEOS in 0.068 mM solution of (a) peptide-1, (b) peptide-2 and (c) peptide-3.*

is most effective, the rates of hydrolysis being considerably higher than those of polyserine and polycysteine. In Fig. 5.2.5a we show a SEM image of silica obtained with polylysine after a period of 96 h. The average particle size of silica obtained by the interaction of TEOS with polylysine is 100 nm.

***5.2.3e Polypeptides:*** Having established that the peptides of lysine and serine are able to hydrolyze TEOS at neutral pH to produce silica, we have examined the interaction of TEOS with synthetic polypeptides containing lysine and serine. In Fig. 5.2.6 we have plotted the weight percent of silica obtained as a product by interaction with 0.068 mM of peptide. 1, R-L-S-K-R-V-S-A-M-Q-N-S-G-V-N-D and 2, Y-G-G-F-S-K-K-K-F-M-R-F containing lysine and serine, hydrolyzed TEOS and produced silica, but they are not as effective as polylysine (see Fig. 5.2.4). It is significant that peptide-3 (S-G-G-L-H-G-V-G) which has no lysine in it exhibits rates very much lower than the peptides 1 and 2. In Fig. 5.2.5b, we show a SEM

image of silica obtained with synthetic peptide 1 after a period of 96 h. The average particle size of the silica is around 200 nm.

***5.2.4 Conclusions:*** The present study establishes that TEOS undergoes hydrolysis at near neutral pH in the presence of lysine and serine to form amorphous silica. The rate of formation of silica from TEOS is enhanced in the case of tetra and polylysine, the latter being more effective than polyserine or polycysteine. Interestingly, synthetic peptides containing a few fragments of lysine and serine also hydrolyze TEOS and produce silica.

### 5.2.5 References

1. M. Hildebrand, B. E. Volcani, W. Gassmann and J. I. Schroeder, *Nature*, 385, 688, 1997.
2. J. N. Cha, K. Shimizu, Y. Zhou, S. C. Chrishtiansen, B. F. Chemelka, G. D. Stucky and D. E. Morse, *Proc. Natl. Acad. Sci., USA*, 96, 361, 1999.
3. Y. Zhou, K. Shimizu, J. N. Cha, G. D. Stucky and D. E. Morse, *Angew. Chem.Int. Edn Engl.*, 38, 780, 1999.
4. J. N. Cha, G. D. Stucky, D. E. Morse and T. J. Deming, *Nature*, 403, 289, 2000.
5. N. Kroger, R. Deutzmann and M. Sumper, *Science*, 286, 1129, 1999.
6. N. Kroger, R. Deutzmann, C. Bergsdorf and M. Sumper, *Proc. Natl. Acad. Sci., USA*, 26, 14133, 2000.
7. R. K. Iler in *Biochemistry of Silicon and Related Problems* Eds. G. Bendz & I. Lindqvist Plenum, 53, 1977.
8. K. D. Lobel, J. K. West and L. L. Hench, *J. Mater. Sci. Lett.*, 15, 648, 1996.
9. *Vogel's textbook of quantitative chemical analysis* Eds. G. H. Jeffery, J. Bassett, J. Mendham and R. C. Denney, Longman, Fifth edn.

## 5.3 Silica fibres obtained with long-chain carboxylic acid templates

***5.3.1 Introduction:*** Synthesis of inorganic assemblies akin to biomineralised structures has emerged to become an attractive area of investigation. Hierarchical structures that incorporate inorganic/organic materials to form mesoscopic structures have been designed and synthesized in recent years. Thus, by employing cationic surfactants it is possible to prepare mesoscopic structures involving bilayer or vesicle templating [1]. Silica hollow tubules, 200-300 μm in length, have been prepared by the hydrolysis of tetraethyl-orthosilicate (TEOS) in a mixture of ethanol, ammonia, water and DL–tartaric acid [2]. These workers have also obtained wormlike structures of silica by substituting DL-tartaric acid with citric acid [3]. Hexagonal phase mesoporous silica fibres have been prepared employing a general method involving the growth of the fibres from an oil-water interface [4]. S. Baral and P. Schoen have recently obtained hollow silica fibres by coating hollow phospholipid tubules with a stable sol of 40% silica, of a particle diameter of 10-15 nm, maintained at pH 9 [5]. Bacterial templating of silica and silica-surfactant mesophases have also been reported recently, the resulting brittle fibre being composed of amorphous silica with organic material and inorganic salts [6]. These fibres are distinctly different from the silica fibres obtained by spinning a viscous sol of TEOS and freezing of aqueous polysilicic acid [7,8].

Since fibres of silica and related self-assembled composite products can be obtained by a suitable choice of organic templates; we have investigated the formation of silica fibres in the presence of long-chain aliphatic carboxylic acids.

***5.3.2 Experimental:*** Experiments with the different long-chain carboxylic acids were carried out by the following procedure. Citric acid (0.04mmol) was added to 200 mmol of isopropanol and stirred till the acid dissolved completely. To this solution, 0.6 mmol of a long-chain acid was added and the stirring continued for 10 minutes. 1 mmol of TEOS was then added slowly and the solution kept stirred for 15minutes. Water (1 mol) was added to this solution, and stirred for 30-45 minutes. The initial pH of the solution was generally ~ 3.5 in these experiments. The final pH of ~7.5 was attained by dropwise addition of 5M NaOH. The product was stirred for 30 minutes and allowed to age for 12 hours in air. The fibrous material obtained in this manner was washed with water and dried at 60-80 $^0$C.

The fiber-carboxylic acid composites were characterized with a SEIFERT XRD 3000TT x-ray diffractometer. LEICA S440i scanning electron microscope (SEM) was employed to study the morphology of these fiber composites. FTIR measurements were carried out using BRUKER IFS 66v/S to analyze the different functional groups present in these composites. Thermal gravimetric analysis (TGA) was carried out by employing a METTLER TOLEDO TGA850.

### *5.3.3 Results and discussion*

***5.3.3a X-ray analysis:*** Figure 5.3.1 shows the X-ray diffraction patterns of as-grown silica fibre-composites obtained with octanoic, decanoic and lauric acids. The patterns indicate a lamellar structure of the silica fibres and the peaks could be indexed accordingly as shown in the figure 5.3.1.

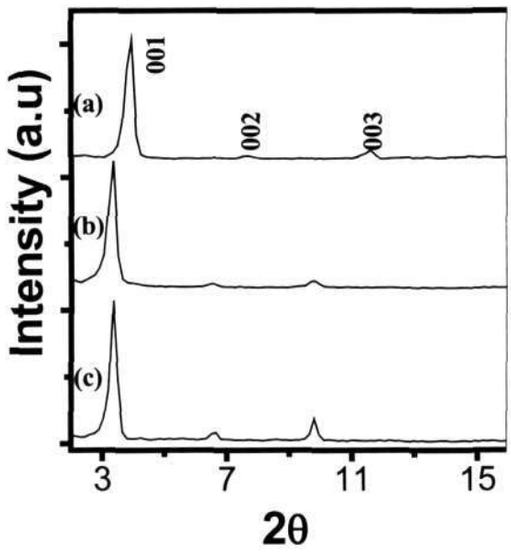


***Fig. 5.3.1*** *X-ray diffraction patterns of the as-synthesized silica fibre-composites with* ***(a)*** *octanoic acid,* ***(b)*** *decanoic acid and* ***(c)*** *lauric acid.*

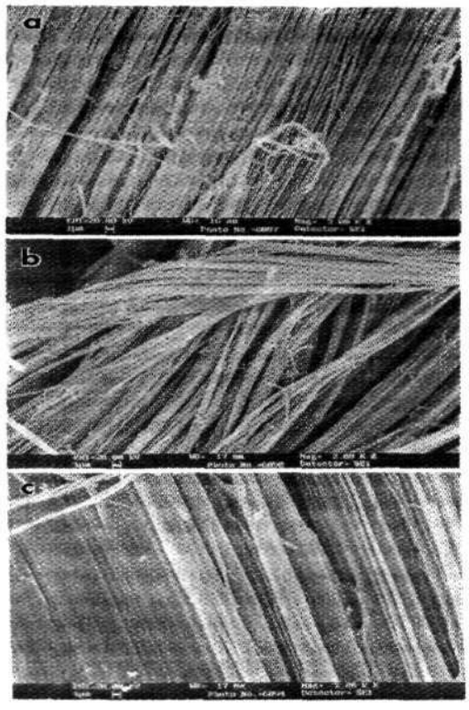


***Fig. 5.3.2*** *SEM images of the as-prepared silica fibre-composites with* ***(a)*** *octanoic acid,* ***(b)*** *decanoic acid and* ***(c)*** *lauric acid.*

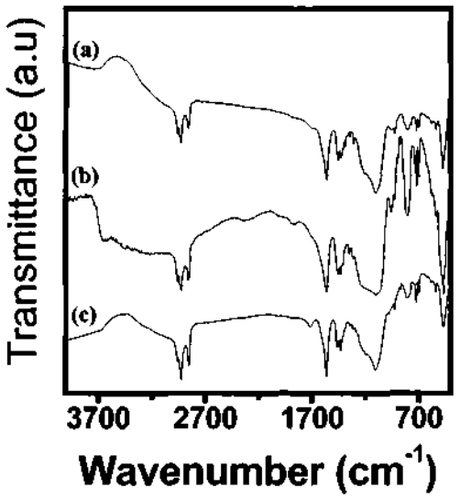


***Figure 5.3.3*** *FTIR spectra of the silica fibre-composties with **(a)** octanoic acid, **(b)** decanoic acid and **(c)** lauric acid.*

***5.3.3b SEM micrographs and IR analysis:*** Figure 5.3.2 shows the SEM images of the as-prepared silica fibre-composites. The images show the beautiful fibre structure and establish the diameter of these fibres to be in 50-100 nm range. Infrared spectra (figure 5.3.3) of the fibre-composite show the characteristic bands associated with stretching of the alkyl groups (2960-2850cm$^{-1}$), $COO^-$ (1610-1550 cm$^{-1}$) and the alkyl group bending modes in the 1450 cm$^{-1}$ region. The O-H stretching and O-H out-of-plane bending of the carboxylic acid group are absent giving credence to the presence of the carboxylate anion. In addition, there is a strong band at 1100- 1000 cm$^{-1}$ corresponding to the Si-O-Si grouping.

***5.3.3c TGA analysis:*** The TGA curves of the fibre-composites (figure 5.3.4) show loss of water below 200 $^0$C and of the long chain carboxylic acid above 300 $^0$C. Based on the TGA results, the compositions are found to be (a) $SiO_2.0.25H_2O.0.25C_8H_{16}O_2$, (b) $SiO_2.0.25H_2O.0.26C_{10}H_{20}O_2$ and (c)

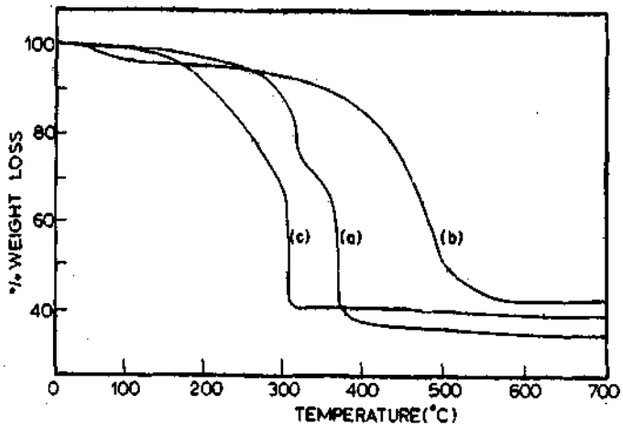


*Fig. 5.3.4 TGA curves of the silica fibre-composites with **(a)** octanoic acid, **(b)** decanoic acid and **(c)** lauric acid.*

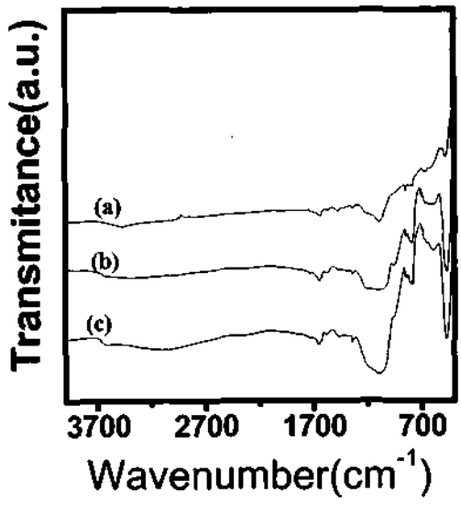


*Fig. 5.3.5 FTIR spectra of the silica fiber-composites with **(a)** octanoic acid, **(b)** decanoic acid and **(c)** lauric acid, heated to 400 $^0$C in air for 2 hours.*

$SiO_2.0.39H_2O.0.25C_{12}H_{24}O_2$ for the fibre composites consisting of octanoic, decanoic and lauric acids respectively. We see the silica to carboxylic acid ratio is generally 4:1, where as silica to water ratio is 3:1. The constancy of silica to carboxylic acid ratio is interesting and suggests a common

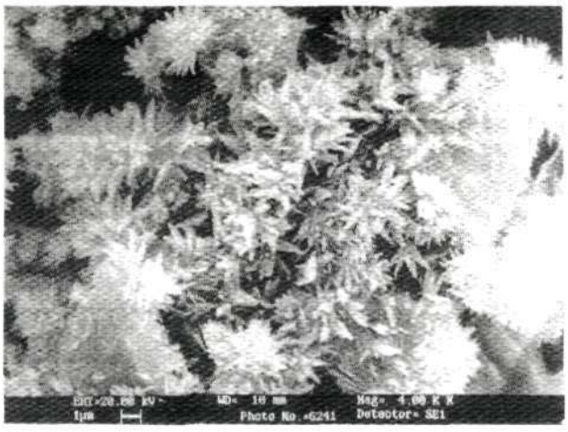

*Fig. 5.3.6 SEM image of the silica-octanoic acid fiber-composite after heating in air at 400 $^0$C for 2 hours.*

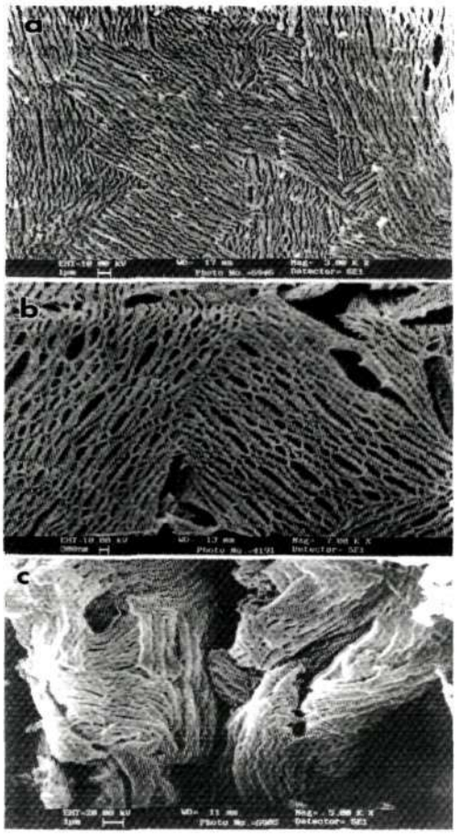


*Fig. 5.3.7 SEM images of the silica fiber-composites with **(a)** octanoic acid, **(b)** decanoic acid and **(c)** lauric acid heated to 300 $^0$C in vacuum for 4 hours.*

mechanism of formation of all the fibre composites. It is to be noted that addition of NaOH neutralizes the carboxylate head group and align the acid molecules to form fibre bundles. It seems that the hydrolysis of silica around the carboxylate head group and the formation of fibrous like structure occur simultaneously, with the gelation of the solution starting around a pH of 6.5.

***5.3.3d Effect of heating:*** Heating the carboxylic acid-silica fibre-composites in air at 400 $^0$C for 2 hours removes the carboxylic acid. Infrared spectra of these products indicate the presence of bands associated with only silica as expected (figure 5.3.5). In figure 5.3.6 we show SEM image of the octanoic acid-silica fiber composite structure obtained after heating to 400 $^0$C for 2 hours in air. The image shows flowery particles. The long fibre like structures are entirely absent. Clearly the fibrous structure of the silica composites have mostly collapsed. XRD patterns show silica obtained in this manner to be amorphous. Instead of heating the composite fibers in air at 400 $^0$C, if they are heated at 300 $^0$C in vacuum for 4 hours, the morphology changes from a fibrous one to a net shape (mesh) structure (figure 5.3.7). Under these conditions there was no loss of carboxylic acids. The change from the fibrous to mesh-like structure arises due to the loss of water molecules.

***5.3.4 Conclusions:*** Fibres of silica have been obtained by using long-chain carboxylic acids as templates. The presence of the acid is necessary for the formation of fibrous structure.

### *5.3.5 References*

1. G. A. Ozin and S. Oliver, *Adv. Mater.*, 7, 943, 1995.
2. H. Nakamura and Y. Matsui, *J. Am. Chem. Soc.*, 117, 2651, 1995.
3. H. Nakamura and Y. Matsui, *Adv. Mater.*, 7, 871, 1995.
4. Q. Huo, D. Zhou, J. Feng, K. Weston, S. K. Buratto, G. D. Stucky, S. Schacht, and F. Schuth, *Adv. Mater.*, 9, 974, 1997.
5. S. Baral and P. Schoen, *Chem. Mater.*, 5, 145, 1993.
6. S. A. Davis, S. L. Burkett, N. H. Mendelson and S. Mann, *Nature,* 385, 420, 1997.
7. K. Matsuzaki D. Arai N. Taneda T. Mukaiyama and M. Ikemura, *J. Non-Cryst. Solids,* 112, 437, 1989.
8. W. Mahler and M. F. Bechtold, *Nature,* 285, 27, 1980.

620.112 97
P03